Novel Metal Oxide Nanocomposites for Oxygen Storage, Sulfur Dioxide Adsorption and Hydrogen Sulfide Absorption

by

Jason T. Sweeney

B. S. Chemical Engineering
Rensselaer Polytechnic Institute, 1994

Submitted to the Department of Chemical Engineering
in Partial Fulfillment of the Requirements for the Degree of

Doctor of Philosophy in Chemical Engineering

at the

MASSACHUSETTS INSTITUTE OF TECHNOLOGY

February 2003

© Massachusetts Institute of Technology 2002. All rights reserved.

Author: _____
Department of Chemical Engineering
September 20, 2002

Certified by: _____
Prof. Jackie Y. Ying
Professor of Chemical Engineering
Thesis Supervisor

Accepted by: _____
Prof. Daniel Blankschtein
Professor of Chemical Engineering
Chairman, Departmental Committee on Graduate Studies

ARCHIVES
MASSACHUSETTS INSTITUTE OF TECHNOLOGY
JAN 0 8 2003
LIBRARIES

Novel Metal Oxide Nanocomposites for Oxygen Storage, Sulfur Dioxide Adsorption and Hydrogen Sulfide Absorption

by

Jason T. Sweeney

B.S. Chemical Engineering
Rensselaer Polytechnic Institute, 1994

Submitted to the Department of Chemical Engineering
on September 20, 2002 in Partial Fulfillment of the Requirements
for the Degree of Doctor of Philosophy in Chemical Engineering

ABSTRACT

Increasingly stringent regulations on automotive emissions have resulted in the need for improved pollution control technology. To reduce mobile emissions, researchers have investigated alternatives such as lean-burn engines and fuel cells. This work is focused on the synthesis, characterization and testing of novel metal oxide nanocomposites to facilitate the utilization of these technologies.

In lean-burn engines, the use of adsorbents to remove NO_x faces two major challenges: (1) excess hydrocarbon and CO emissions during fuel-rich pulses for adsorbent regeneration, and (2) reduced NO_x adsorption efficiencies due to competitive adsorption of SO_2 in the gas stream. To provide for the low-temperature oxidation of hydrocarbons and CO under a reducing atmosphere, CeO_2, a well-known oxygen storage material, was modified through secondary metal oxide doping to improve thermal stability and oxygen accessibility. 20 at% substitution of Pr, Sc and Zr in CeO_2 successfully promoted microstructural stability, with $Ce_{0.8}Zr_{0.2}O_{2-\delta}$ retaining grain size of 30 nm even after calcination at 1000°C. At high doping levels, Zr improved grain size stability further, but ZrO_2 phase segregation was noted in $Ce_{1-x}Zr_xO_{2-\delta}$ with $x > 0.2$. TPR experiments under 2.5% H_2 in He showed that $Ce_{0.8}Pr_{0.2}O_{2-\delta}$ provided superior low-temperature reduction and overall reducibility amongst $Ce_{0.8}M_{0.2}O_{2-\delta}$ materials. Moreover, $Ce_{1-x}Pr_xO_{2-\delta}$ showed increased reducibility with increasing x, achieving a maximum weight loss of 4.8% at $x = 1.0$. CO oxidation studies over $Ce_{0.8}M_{0.2}O_{2-\delta}$ identified Sc and Zr doping with the lowest CO light-off temperatures (247°C and 264°C, respectively). For $Ce_{1-x}Pr_xO_{2-\delta}$ and $Ce_{1-x}Zr_xO_{2-\delta}$, low levels of doping resulted in the highest CO oxidation activity; light-off was successfully achieved at 264°C and 252°C for $x = 0.4$ and 0.1, respectively.

Metal oxide-based materials were developed to selectively adsorb SO_2 during fuel-lean conditions and desorb SO_2 during fuel-rich conditions, thereby preventing the SO_2 poisoning of the NO_x adsorbent. Of various simple and mixed metal oxides, the Cr_2O_3-CuO system was found to provide SO_2 adsorption under oxidizing conditions at

400°C, and SO_2 evolution under reducing conditions below 350°C. The $CuCr_2O_4$ phase present at the optimal Cr_2O_3-CuO composition gave rise to improved low-temperature CO activity, which facilitated SO_2 desorption. With increased CuO content, both adsorption capacity and regenerability were increased. Through the introduction of dopants, phase-pure $CuCr_{2-y}Co_yO_4$ was obtained to allow for SO_2 desorption below 300°C, which corresponded well with increased CO_2 evolution. By introducing excess CuO onto $CuCr_{1.9}Co_{0.1}O_4$ via various synthesis routes, improved SO_2 sorption characteristics were attained. In pulse adsorption/desorption studies, the CuO/ $CuCr_{1.9}Co_{0.1}O_4$ materials and $CuO/CuCr_2O_4$ also demonstrated excellent capacity and superior regenerability relative to the conventional CuO/Al_2O_3 adsorbent.

For on-board H_2 production for fuel cells, the removal of H_2S is paramount to avoiding poisoning of the H_2 separation membrane and the fuel cell. Conventional coarse-grained ZnO is not viable for H_2S removal in fuel cell powered vehicles due to weight and efficiency concerns. To address these challenges, nanocrystalline ZnO was synthesized with a grain size of < 10 nm and a surface area > 150 m^2/g upon calcination at 200°C. However, significant grain growth to 21 nm and 45 nm was experienced at 300°C and 500°C, respectively, with a concomitant decrease in surface area to 81 m^2/g and 15 m^2/g. Since H_2S absorption is a diffusion-controlled process, the nanocrystalline materials showed absorption capacity of 10 times and 1.5 times higher than conventional ZnO at 300°C and 500°C, respectively. To prevent sintering above 200°C and structural degradation during regeneration, TiO_2, V_2O_5 and ZrO_2 coatings were introduced onto the ZnO nanoparticles through liquid-phase adsorption and condensation. The resulting nanocomposites showed improved stability at 500°C, with TiO_2-coated ZnO retaining an ultrafine grain size of 9 nm and an ultrahigh surface area of 88 m^2/g. The TiO_2-coated ZnO nanocomposite achieved H_2S absorption capacity of > 90% at both 300°C and 500°C. Regenerability of TiO_2- and ZrO_2-coated ZnO at 500°C was also superior to nanocrystalline and conventional ZnO materials.

Thesis Supervisor: Jackie Y. Ying
Title: Professor of Chemical Engineering

Acknowledgements

First and foremost, I am grateful to Prof. Jackie Ying for her financial and technical support. She provided encouragement and guidance throughout my research, which were essential to me realizing the accomplishments presented here. I would like to thank the members of my thesis committee: Prof. Jefferson Tester, Prof. T. Alan Hatton and Prof. William Green for their advice. I would like to thank Professor Bernhardt Wuensch for helping me develop a fundamental understanding of crystal structure.

As a member of the Nanostructured Materials Research Laboratory (NMRL), I had the opportunity to work with very talented people. The guidance and expertise of senior NMRL members, Dr. Larry Panchula, Dr. Andrey Zarur, Dr. Michael Wong, Dr. Christian Mehnert, Dr. Edward Ahn, Dr. Mark Fokema, Dr. Chen-chi Wang, Dr. Lei Zhang, Dr. John Lettow and Duane Myers helped me immensely in starting my research. In particular, Dr. Michael Wong, Dr. Mark Fokema and Dr. Edward Ahn have helped me define and direct my research. Pemakorn Pitukmanorom and Mark Stoykovich were instrumental in my completing pulsed CO oxidation analysis and synthesis, respectively, for the CeO_2-based nanocomposites. I am indebted to Dr. Larry Panchula, Dr. Neeraj Sangar, Yee San Su and Steven Weiss for their help on various technical projects. I would like to thank Dr. Justin McCue, the other member of my class, for his support and helpful discussion throughout the thesis process. All the other members of the NMRL have contributed in one way or another to the development of this research, and for this, I thank them profoundly. They are Dr. Javier García-Martínez, Dr. Dejian Huang, Dr. Jinsuo Xu, Dr. Su Seoung Lee, Suniti Moudgil, Yu-Ming Lin, Todd Zion, Thomas Lancaster, Wolfgang Rupp, Jianyi Cui and Noreen Zaman.

I would like to acknowledge Michael Frongillo for his assistance in obtaining electron micrographs for my thesis, and Dr. Elizabeth Shaw who was helpful in collecting X-ray photoelectron spectroscopy data. I would also like to acknowledge Linda Mousseau for taking care of the administrative tasks of the group, and for her support and friendship. Financial support from Packard Foundation and Ford Motor Company is appreciated.

Finally, I would like to acknowledge my family. Without the love and support of my wife Erin, and my children Ian and Aidan, I would not have been able to accomplish the work presented here. I would also like to thank my grandmother Elsie McAvoy, my mother and stepfather Margaret and Jim Baker, my father Thomas Sweeney, and my father- and mother-in law Fredric and Caroline Wilson for their support.

Contents

1 Background and Research Motivation **16**
1.1 Improved Low-Temperature Oxidation for Catalytic Converters 16
1.1.1. Current Technology 17
1.1.2. Research Direction 17
1.2 Adsorbents for Lean-Burn Engines 18
1.2.1. Current Technology 19
1.2.2. Research Direction 19
1.3 H_2S Removal Technology for Automotive Fuel Cells 20
1.3.1. Current Technology 21
1.3.2. Research Direction 22
1.4 Research Motivation and Approach 22
1.5 References 25

2 Rare Earth Oxide Nanocomposites for Oxygen Storage Applications **27**
2.1 Introduction 27
2.2 Experimental 28
2.2.1. Materials Synthesis 28
2.2.2. Structural Characterization 28
2.2.3. Temperature-Programmed Reduction and Catalytic CO Oxidation Studies 29
2.3 Results and Discussion 30
2.3.1. Structural Characteristics and Stability of $Ce_{1-x}M_xO_{2-\delta}$ Nanocomposites 30
2.3.1.1. $Ce_{0.8}M_{0.2}O_{2-\delta}$ with Non-Lanthanide Dopants 30
2.3.1.2. $Ce_{0.8}M_{0.2}O_{2-\delta}$ with Lanthanide Dopants 32
2.3.1.3. $Ce_{1-x}M_xO_{2-\delta}$ with Zr, Pr, Tb and Sm Dopants 34
2.3.2. Temperature-Programmed Reduction of $Ce_xM_{1-x}O_{2-\delta}$ 41
2.3.2.1. Reducibility of $Ce_{0.8}M_{0.2}O_{2-\delta}$ with Non-Lanthanide Dopants 41
2.3.2.2. Reducibility of $Ce_{0.8}M_{0.2}O_{2-\delta}$ with Lanthanide Dopants 42
2.3.2.3. Reducibility of $Ce_{1-x}M_xO_{2-\delta}$ with Zr, Pr and Tb Dopants 43
2.3.3. Catalytic CO Oxidation Studies 46
2.3.3.1. CO Conversion over $Ce_{0.8}M_{0.2}O_{2-\delta}$ 46
2.3.3.2. CO Conversion over $Ce_{1-x}Zr_xO_{2-\delta}$ and $Ce_{1-x}Pr_xO_{2-\delta}$ 48
2.4 Summary 49
2.5 References 51

3 Metal Oxide Nanocomposites for Low-Temperature SO_2 Adsorption **52**
3.1 Introduction 52
3.2 Experimental 53
3.2.1. Materials Synthesis 53
3.2.2. Materials Characterization 53
3.2.3. SO_2 Adsorption and Regeneration 53
3.3 Results and Discussion 56
3.3.1. SO_2 Sorption Characteristics of Mixed Oxides 56
3.3.1.1. Synthesis and Characteristics of CuO-based Mixed Oxides 56
3.3.1.2. Synthesis and Characteristics of Cr_2O_3-CuO Mixed Oxides 58

3.3.2. Doping of $CuCr_2O_4$ for Improved SO_2 Sorption Characteristics 65
3.3.2.1. Synthesis and Sorption Characteristics of $Cu_{0.95}M_{0.05}Cr_2O_4$ 65
3.3.2.2. Synthesis and Sorption Characteristics of $CuCr_{1.9}M_{0.1}O_4$ 67
3.3.2.3. Synthesis and Sorption Characteristics of $CuCr_{2-y}Co_yO_4$ 71
3.3.3. Adsorption Performance of $CuO/CuCr_{1.9}Co_{0.1}O_4$ Materials 75
3.3.3.1. Synthesis and Characteristics of $CuO/CuCr_{1.9}Co_{0.1}O_4$ 75
3.3.3.2. Dynamic SO_2 Adsorption/Desorption Studies 80
3.4 Summary 83
3.5 References 85

4 Synthesis and Stabilization of Zinc Oxide Nanocrystals for H_2S Absorption 86
4.1 Introduction 86
4.2 Experimental 87
4.2.1. Materials Synthesis 87
4.2.2. Materials Characterization 88
4.2.3. Absorption and Kinetic Analyses 88
4.3 Results and Discussion 89
4.3.1. Synthesis of Nanocrystalline ZnO 89
4.3.1.1. Effect of Base 90
4.3.1.2. Effect of $Zn(NO_3)_2 \cdot 6H_2O$ Precursor Concentration 92
4.3.1.3. Effect of Calcination Temperature 93
4.3.2. Stabilization of ZnO Nanocrystals through Secondary Oxide Coating 97
4.3.2.1. Effect of Coating Composition 98
4.3.2.2. Surface Characterization of the Coated ZnO Nanoparticles 101
4.3.2.3. Effect of ZnO Pretreatment on Secondary Oxide Loading 103
4.3.3. H_2S Absorption Studies 106
4.3.3.1. H_2S Absorption over Nanocrystalline ZnO 107
4.3.3.2. H_2S Absorption over TiO_2- and ZrO_2-coated ZnO Nanocrystals 110
4.3.4. Regeneration of Pure and Coated ZnO Nanocrystals 112
4.3.4.1. Evolution of SO_2 from Pure and Coated ZnO Nanocrystals 112
4.3.4.2. Regeneration of Nanocrystalline and Conventional ZnO 113
4.3.4.3. Regeneration of TiO_2- and ZrO_2-coated ZnO Nanocrystals 117
4.3.5. H_2S Absorption Kinetics 120
4.3.5.1. Effect of Grain Size and Absorption Temperature on ZnO Conversion 121
4.3.5.2. Effect of Absorption Temperature on Coated ZnO Conversion 124
4.3.5.3. Surface Absorption Kinetics of Pure and Coated ZnO Nanocrystals 126
4.4 Summary 131
4.5 References 133

5 Recommendations for Future Work 134

6 Conclusions 135

List of Figures

2.1 Schematic of reactor setup. 30

2.2 Effect of calcination temperature on the XRD grain size of (a) CeO_2, (b) $Ce_{0.8}Ca_{0.2}O_{2-\delta}$, (c) $Ce_{0.8}Y_{0.2}O_{2-\delta}$, (d) $Ce_{0.8}Sc_{0.2}O_{2-\delta}$ and (e) $Ce_{0.8}Zr_{0.2}O_{2-\delta}$. 32

2.3 Effect of calcination temperature on the XRD grain size of (a) CeO_2, (b) $Ce_{0.8}Sm_{0.2}O_{2-\delta}$, (c) $Ce_{0.8}Tb_{0.2}O_{2-\delta}$ and (d) $Ce_{0.8}Pr_{0.2}O_{2-\delta}$. 34

2.4 XRD patterns of 1000°C-calcined $Ce_{1-x}Zr_xO_{2-\delta}$ with x = (a) 0.0, (b) 0.1, (c) 0.2, (d) 0.3 and (e) 0.4. Tetragonal ZrO_2 <101> reflection (*) was noted for $x > 0.2$. 36

2.5 Effect of dopant concentration on the a_{200} lattice parameter of 600°C-calcined $Ce_{1-x}M_xO_{2-\delta}$ doped with (a) Sm, (b) Pr, (c) Tb and (d) Zr. 37

2.6 Effect of dopant concentration on the XRD grain size of $Ce_{1-x}Sm_xO_{2-\delta}$ calcined at (a) 600°C, (b) 800°C and 1000°C. 38

2.7 Effect of dopant concentration on the XRD grain size of $Ce_{1-x}Tb_xO_{2-\delta}$ calcined at (a) 600°C, (b) 800°C and (c) 1000°C. 38

2.8 Effect of dopant concentration on the XRD grain size of $Ce_{1-x}Pr_xO_{2-\delta}$ calcined at (a) 600°C, (b) 800°C and (c) 1000°C. 39

2.9 Effect of dopant concentration on the XRD grain size of $Ce_{1-x}Zr_xO_{2-\delta}$ calcined at (a) 600°C, (b) 800°C and (c) 1000°C. 39

2.10 HRTEM micrograph of 1000°C-calcined $Ce_{0.6}Zr_{0.4}O_{2-\delta}$ showing (a) and (b) segregated amorphous ZrO_2, and (c) and (d) thin coatings of ZrO_2 around $Ce_{1-x}Zr_xO_{2-\delta}$ crystallites. 40

2.11 TPR analysis of (a) CeO_2 and $Ce_{0.8}M_{0.2}O_{2-\delta}$ doped with (b) Y, (c) Sc, (d) Zr and (e) Ca. The 800°C-calcined materials were first pretreated *in situ* at 800°C in O_2, followed by TPR at 150-800°C under 2.5% H_2 in He. 42

2.12 TPR analysis of (a) CeO_2 and $Ce_{0.8}M_{0.2}O_{2-\delta}$ doped with (b) Sm, (c) Tb and (d) Pr. The 800°C-calcined materials were first pretreated *in situ* at 800°C in O_2, followed by TPR at 150-800°C under 2.5% H_2 in He. 43

2.13 TPR analysis of $Ce_{1-x}Zr_xO_{2-\delta}$ with x = (a) 0.0, (b) 0.1, (c) 0.2, (d) 0.3 and (e) 0.4. The 800°C-calcined materials were first pretreated *in situ* at 800°C in O_2, followed by TPR at 150-800°C under 2.5% H_2 in He. 44

2.14 TPR analysis of $Ce_{1-x}Tb_xO_{2-\delta}$ with x = (a) 0.0, (b) 0.2, (c) 0.4, (d) 0.6, (e) 0.8 and (f) 1.0. The 800°C-calcined materials were first pretreated *in situ* at 800°C in O_2, followed by TPR at 150-800°C under 2.5% H_2 in He. 45

2.15 TPR analysis of $Ce_{1-x}Pr_xO_{2-\delta}$ with x = (a) 0.0, (b) 0.2, (c) 0.4, (d) 0.6, (e) 0.8 and (f) 1.0. The 800°C-calcined materials were first pretreated *in situ* at 800°C in O_2, followed by TPR at 150-800°C under 2.5% H_2 in He. 45

2.16 CO conversion over 600°C-calcined (■) $Ce_{0.8}Sc_{0.2}O_{2-\delta}$, (Δ) $Ce_{0.8}Zr_{0.2}O_{2-\delta}$, (♦) CeO_2, (○) $Ce_{0.8}Ca_{0.2}O_{2-\delta}$ and (*) $Ce_{0.2}Y_{0.8}O_{2-\delta}$. The reaction was conducted with 1% CO and 0.75% O_2 in He at 120,000 hr^{-1}. 47

2.17 CO conversion over 600°C-calcined (*) $Ce_{0.8}Pr_{0.2}O_{2-\delta}$, (■) CeO_2, (Δ) $Ce_{0.8}Tb_{0.2}O_{2-\delta}$ and (○) $Ce_{0.2}Sm_{0.8}O_{2-\delta}$. The reaction was conducted with 1% CO and 0.75% O_2 in He at 120,000 hr^{-1}. 47

2.18 CO conversion over 600°C-calcined (■) $Ce_{0.9}Zr_{0.1}O_{2-\delta}$, (○) $Ce_{0.8}Zr_{0.2}O_{2-\delta}$, (*) CeO_2, (♦) $Ce_{0.7}Zr_{0.3}O_{2-\delta}$ and (Δ) $Ce_{0.6}Zr_{0.4}O_{2-\delta}$. The reaction was conducted with 1% CO and 0.75% O_2 in He at 120,000 hr^{-1}. 48

2.19 CO conversion over 600°C-calcined (■) $Ce_{0.6}Pr_{0.4}O_{2-\delta}$, (♦) $Ce_{0.8}Pr_{0.2}O_{2-\delta}$, (○) $Ce_{0.4}Pr_{0.6}O_{2-\delta}$, (Δ) CeO_2, (+) $Ce_{0.2}Pr_{0.8}O_{2-\delta}$ and (×) $PrO_{2-\delta}$. The reaction was conducted with 1% CO and 0.75% O_2 in He at 120,000 hr^{-1}. 49

3.1 SO_2 adsorption reactor setup. 54

3.2 Schematic of pulsing reactor setup. 56

3.3 TPD of SO_2 over mixed oxides of CuO and (a) MnO_2, (b) Co_2O_3, (c) NiO, (d) CuO, (e) Fe_2O_3, (f) In_2O_3 and (g) Cr_2O_3. Following SO_2 adsorption at 400°C, SO_2 desorption was conducted by introducing 1% O_2 in He at 200°C, and then 2000 ppm CO in He at GHSV ~ 120,000 hr^{-1} and 200-700°C (ramp = 1°C/min). 58

3.4 Phase diagram of Cr_2O_3 and CuO_x. 59

3.5 XRD patterns of 800°C-calcined Cr_2O_3-CuO mixed oxides with (a) 100%, (b) 75%, (c) 66%, (d) 56%, (e) 33% and (f) 0% CuO. Phases present include (*) CuO, (+) $CuCr_2O_4$, (o) $CuCrO_2$ and (#) Cr_2O_3. 60

3.6 Weight gain associated with SO_2 adsorption over 500°C-calcined Cr_2O_3-CuO with (a) 100%, (b) 75%, (c) 66%, (d) 56%, (e) 33% and (f) 0% CuO. The TGA analysis was performed with a feedstream of 130 ppm SO_2 and 1% O_2 in He at a flow rate of 400 sccm and 400°C. 63

3.7 TPD of SO_2 over 500°C-calcined Cr_2O_3-CuO with (a) 100%, (b) 75%, (c) 66%, (d) 56%, (e) 33% and (f) 0% CuO. Following SO_2 adsorption at 400°C, SO_2 desorption was conducted by introducing 1% O_2 in He at 200°C, and then 2000 ppm CO in He at GHSV ~ 240,000 hr^{-1} and 200-600°C (ramp = 1°C/min). 64

3.8 CO_2 evolution corresponding to the SO_2 TPD over 500°C-calcined Cr_2O_3-CuO with (a) 100%, (b) 75%, (c) 66%, (d) 56%, (e) 33% and (f) 0% CuO. Following SO_2 adsorption at 400°C, SO_2 desorption was conducted by introducing 1% O_2 in He at 200°C, and then 2000 ppm CO in He at GHSV ~ 240,000 hr^{-1} and 200-600°C (ramp = 1°C/min). 64

3.9 TPD of SO_2 over 500°C-calcined $Cu_{0.95}M_{0.05}Cr_2O_4$ with M = (a) Fe, (b) Co, (c) Ni and (d) Cu. Following SO_2 adsorption at 400°C, SO_2 desorption was conducted by introducing 1% O_2 in He at 200°C, and then 2000 ppm CO in He at GHSV ~ 240,000 hr^{-1} and 200-500°C (ramp = 1°C/min). 67

3.10 TPD of SO_2 over 500°C-calcined $CuCr_{1.9}M_{0.1}O_4$ with M = (a) Al, (b) Cr, (c) Fe, (d) Co and (e) Ni. Following SO_2 adsorption at 400°C, SO_2 desorption was conducted by introducing 1% O_2 in He at 200°C, and then 2000 ppm CO in He at GHSV ~ 240,000 hr^{-1} and 200-500°C (ramp = 1°C/min). 70

3.11 CO_2 evolution corresponding to the SO_2 TPD over 500°C-calcined $CuCr_{1.9}M_{0.1}O_4$ with M = (a) Al, (b) Cr, (c) Fe, (d) Co and (e) Ni. Following SO_2 adsorption at 400°C, SO_2 desorption was conducted by introducing 1% O_2 in He at 200°C, and then 2000 ppm CO in He at GHSV ~ 240,000 hr^{-1} and 200-500°C (ramp = 1°C/min). 71

3.12 XRD patterns of 1000°C-calcined $CuCr_{2-y}Co_yO_4$ with y = (a) 0.20, (b) 0.15, (c) 0.10, (d) 0.05 and (e) 0.00. Besides the $CuCr_2O_4$ phase, peaks associated with the secondary $CuCrO_2$ phase were noted (#) in the Co-doped samples. 72

3.13 TPD of SO_2 over 500°C-calcined $CuCr_{2-y}Co_yO_4$ with y = (a) 0.20, (b) 0.15, (c) 0.10, (d) 0.05 and (e) 0.00. Following SO_2 adsorption at 400°C, SO_2 desorption was conducted by introducing 1% O_2 in He at 200°C, and then 2000 ppm CO in He at GHSV ~ 240,000 hr^{-1} and 200-500°C (ramp = 1°C/min). 74

3.14 CO_2 evolution corresponding to the SO_2 TPD over 500°C-calcined $CuCr_{2-y}Co_yO_4$ with y = (a) 0.20, (b) 0.15, (c) 0.10, (d) 0.05 and (e) 0.00. Following SO_2 adsorption at 400°C, SO_2 desorption was conducted by introducing 1% O_2 in He at 200°C, and then 2000 ppm CO in He at GHSV ~ 240,000 hr^{-1} and 200-600°C (ramp = 1°C/min). 75

3.15 XRD patterns of 800°C-calcined (a) $CuCr_{1.9}Co_{0.1}O_4$, $CuO/CuCr_{1.9}Co_{0.1}O_4$ prepared by (b) CP, (c) PP, (d) RP and (e) IP methods, and (f) $CuO/CuCr_2O_4$. Besides the $CuCr_2O_4$ phase (♦), peaks associated with the secondary CuO phase were noted (*). 77

3.16 TPD of SO_2 over 500°C-calcined (a) $CuCr_{1.9}Co_{0.1}O_4$, $CuO/CuCr_{1.9}Co_{0.1}O_4$ prepared by (b) CP, (c) PP, (d) RP and (e) IP methods, and (f) $CuO/CuCr_2O_4$. Following SO_2 adsorption at 400°C, SO_2 desorption was conducted by introducing 1% O_2 in He at 200°C, and then 2000 ppm CO in He at GHSV ~ 240,000 hr^{-1} and 200-500°C (ramp = 1°C/min). 79

3.17 CO_2 evolution corresponding to the SO_2 TPD over 500°C-calcined (a) $CuCr_{1.9}Co_{0.1}O_4$, $CuO/CuCr_{1.9}Co_{0.1}O_4$ prepared by (b) CP, (c) PP, (d) RP and (e) IP methods, and (f) $CuO/CuCr_2O_4$. Following SO_2 adsorption at 400°C, SO_2 desorption was conducted by introducing 1% O_2 in He at 200°C, and then 2000 ppm CO in He at GHSV ~ 240,000 hr^{-1} and 200-600°C (ramp = 1°C/min). 80

3.18 SO_2 evolution during alternating pulses of 0.5% O_2 in He (10 min) and 1% CO in He (10 min) over 500°C-calcined (a) CuO/Al_2O_3, (b) $CuCr_{1.9}Co_{0.1}O_4$, $CuO/CuCr_{1.9}Co_{0.1}O_4$ prepared by (c) CP, (d) PP, (e) RP and (f) IP methods, and (g) $CuO/CuCr_2O_4$. A constant feed of 300 ppm SO_2 (---) was introduced at GHSV ~ 120,000 hr^{-1} and 400°C. Prior to each pulse, a 1-min He purge was fed. 82

4.1	Schematic of reactor setup.	89
4.2	BET surface area of ZnO synthesized using (a) $(NH_4)_2CO_3$ and (b) TEAH as the base.	90
4.3	TEM micrographs of (a) $ZnCO_3$ precipitate, (b) 300°C-calcined ZnO nanoparticles by $(NH_4)_2CO_3$ synthesis, (c) ZnOH precipitate, and (d) 300°C-calcined ZnO nanoparticles by TEAH synthesis.	92
4.4	Effect of $Zn(NO_3)_2 \cdot 6H_2O$ concentration in the $(NH_4)_2CO_3$ synthesis on the (a) BET surface area and (b) XRD grain size of 300°C-calcined ZnO.	93
4.5	(a) Weight loss and (b) heat flow associated with the thermal decomposition of the $ZnCO_3$ precipitate in air (ramp = 10°C/min).	94
4.6	XRD patterns of (a) uncalcined $ZnCO_3$ precipitate, and $ZnCO_3$ calcined at 200°C in air for (b) 1 hour, (c) 4 hours and (d) 6 hours.	95
4.7	PA-FTIR spectra of (a) uncalcined $ZnCO_3$ precipitate, and $ZnCO_3$ calcined at 200°C in air for (b) 1 hour, (c) 4 hours and (d) 6 hours.	96
4.8	BET surface area of (a) TiO_2-, (b) ZrO_2- and (c) V_2O_5-coated ZnO nanoparticles, and (d) uncoated ZnO nanoparticles calcined to 500-900°C.	99
4.9	XRD grain size of (a) TiO_2-, (b) ZrO_2- and (c) V_2O_5-coated ZnO nanoparticles, and (d) uncoated ZnO nanoparticles calcined to 500-900°C.	99
4.10	XRD patterns of (a) TiO_2-, (b) ZrO_2- and (c) V_2O_5-coated ZnO nanoparticles, and (d) uncoated ZnO nanoparticles calcined to 700°C. Peaks corresponding to secondary phases are denoted: (o) ZrO_2 and (*) $Zn_3(VO_4)_2$.	100
4.11	TEM micrographs of (a,e) nanocrystalline ZnO, (b,f) TiO_2-, (c,g) ZrO_2- and (d,h) V_2O_5-coated ZnO nanoparticles calcined to 500°C (a-d) and 700°C (e-h).	101
4.12	XPS spectra of (a) conventional TiO_2, TiO_2-coated ZnO nanoparticles calcined at (b) 500°C, (c) 700°C and (d) 900°C, and (e) conventional $ZnTiO_3$.	102
4.13	HR-TEM micrographs of (a) TiO_2- and (b) ZrO_2-coated ZnO nanoparticles calcined to 700°C, and (c) V_2O_5-coated ZnO nanoparticles calcined to 500°C.	103
4.14	(a) TiO_2 and (b) ZrO_2 loadings on ZnO nanoparticles that were pretreated at 25°C in a flowing He gas stream containing different water contents.	104
4.15	BET surface areas of (o) TiO_2- and (x) ZrO_2-coated ZnO nanoparticles calcined to 500°C (---) and 700°C (—).	105
4.16	XRD grain sizes of (o) TiO_2- and (x) ZrO_2-coated ZnO nanoparticles calcined to 500°C (---) and 700°C (—).	106

4.17 H_2S absorption analysis for (a) conventional ZnO (130 nm), (b) nanocrystalline ZnO calcined to 500°C (43 nm), (c) nanocrystalline ZnO calcined to 400°C (28 nm) and (d) nanocrystalline ZnO calcined to 300°C (13 nm), with 1000 ppm H_2S in He with GHSV = 30,000 hr^{-1} at 300°C. 107

4.18 H_2S absorption analysis for (a) conventional ZnO (130 nm) and (b) nanocrystalline ZnO calcined to 500°C (43 nm), with 1000 ppm H_2S in He and GHSV = 30,000 hr^{-1} at 500°C. 108

4.19 Effect of grain radius on ZnO breakthrough conversion at (a) 300°C, (b) 400°C and (c) 500°C, with 1000 ppm H_2S in He at 30,000 hr^{-1}. 109

4.20 H_2S absorption analysis for (a) nanocrystalline ZnO calcined at 300°C, TiO_2-coated ZnO nanocrystals calcined at (b) 500°C and (c) 700°C, and ZrO_2-coated ZnO nanocrystals calcined at (d) 500°C and (e) 700°C, with 1000 ppm H_2S in He at 30,000 hr^{-1} and 300°C. 111

4.21 H_2S absorption analysis for (a) nanocrystalline ZnO calcined at 500°C, TiO_2-coated ZnO nanocrystals calcined at (b) 500°C and (c) 700°C, and ZrO_2-coated ZnO nanocrystals calcined at (d) 500°C and (e) 700°C, with 1000 ppm H_2S in He at ~30,000 hr^{-1} and 500°C. 112

4.22 Temperature-programmed desorption of presulfided (a) conventional ZnO, (b) 500°C-calcined nanocrystalline ZnO, (c) TiO_2-coated ZnO nanocrystals and (d) ZrO_2-coated ZnO nanocrystals in air at 30,000 hr^{-1}. 113

4.23 H_2S absorption analysis for 500°C-calcined nanocrystalline ZnO with 1000 ppm H_2S in He at 30,000 hr^{-1} and 500°C: (a) first cycle, (b) second cycle and (c) third cycle. The sample was regenerated in air at 650°C for 4 hours at 30,000 hr^{-1} after each absorption cycle. 114

4.24 H_2S absorption analysis for conventional ZnO with 1000 ppm H_2S in He at 30,000 hr^{-1} and 500°C: (a) first cycle, (b) second cycle and (c) third cycle. The sample was regenerated in air at 650°C for 4 hours at 30,000 hr^{-1} after each absorption cycle. 115

4.25 TEM micrographs of (a) 500°C-calcined nanocrystalline ZnO and (b) conventional ZnO, and (c) nanocrystalline and (d) conventional ZnO following the third regeneration in air at 650°C for 4 hours at 30,000 hr^{-1}. 116

4.26 H_2S absorption analysis for 700°C-calcined TiO_2-coated ZnO with 1000 ppm H_2S in He at 30,000 hr^{-1} and 500°C: (a) first cycle (——), (b) second cycle (----) and (c) third cycle (– – –). The sample was regenerated in air at 650°C for 4 hours at 30,000 hr^{-1} after each absorption cycle. 117

4.27 H_2S absorption analysis for 700°C-calcined ZrO_2-coated ZnO with 1000 ppm H_2S in He at 30,000 hr^{-1} and 500°C: (a) first cycle (——), (b) second cycle (----) and (c) third cycle (– – –). The sample was regenerated in air at 650°C for 4 hours at 30,000 hr^{-1} after each absorption cycle. 118

4.28 XRD patterns of (a) 700°C-calcined and (b) thrice-regenerated TiO_2-coated ZnO, and (a) 700°C-calcined and (b) thrice-regenerated ZrO_2-coated ZnO. Peaks associated with ZnO (unmarked), $ZnTiO_3$ (*) and ZrO_2 (o) were observed. 119

4.29 TEM micrographs of 700°C-calcined (a) TiO_2- and (b) ZrO_2-coated ZnO, and (c) TiO_2- and (d) ZrO_2-coated ZnO following the third regeneration cycle in air at 650°C for 4 hours at 30,000 hr^{-1}. 120

4.30 TGA analysis of H_2S absorption for nanocrystalline ZnO calcined to (a) 300°C, (b) 400°C and (c) 500°C, and (d) conventional ZnO, with 500 sccm of 0.4% H_2S in He at 300°C. 122

4.31 TGA analysis of H_2S absorption for conventional ZnO with 500 sccm of 0.4% H_2S in He at (a) 300°C, (b) 400°C and (c) 500°C. 123

4.32 TGA analysis of H_2S absorption for 500°C-calcined nanocrystalline ZnO with 500 sccm of 0.4% H_2S in He at (a) 300°C, (b) 400°C and (c) 500°C. 123

4.33 TGA analysis of H_2S absorption for (a) TiO_2- and (b) ZrO_2-coated ZnO, and (c) 300°C-calcined and (d) 500°C-calcined nanocrystalline ZnO, with 500 sccm of 0.4% H_2S in He at 300°C. 124

4.34 TGA analysis of H_2S absorption for (a) TiO_2- and (b) ZrO_2-coated ZnO, and (c) 500°C-calcined nanocrystalline ZnO, with 500 sccm of 0.4% H_2S in He at 300°C. 125

4.35 TGA analysis of H_2S absorption for (a) TiO_2- and (b) ZrO_2-coated ZnO, and 500°C-calcined nanocrystalline ZnO, with 500 sccm of 0.4% H_2S in He at 300°C. 126

4.36 Effect of gas-phase H_2S concentration on the intrinsic reaction rate of 500°C-calcined nanocrystalline ZnO at (a) 300°C, (b) 400°C and (c) 500°C. 127

4.37 Effect of gas-phase H_2S concentration on the intrinsic reaction rate of conventional ZnO at (a) 300°C, (b) 400°C and (c) 500°C. 128

4.38 Arrhenius plot for (▲) conventional ZnO and (■) 500°C-calcined nanocrystalline ZnO. 128

4.39 Effect of gas-phase H_2S concentration on the intrinsic reaction rate of 700°C-calcined TiO_2-coated ZnO at (a) 300°C, (b) 400°C and (c) 500°C. 129

4.40 Effect of gas-phase H_2S concentration on the intrinsic reaction rate of 700°C-calcined ZrO_2-coated ZnO at (a) 300°C, (b) 400°C and (c) 500°C. 130

4.41 Arrhenius plot for 700°C-calcined (a) ZrO_2- and (b) TiO_2-coated ZnO. 130

List of Tables

2.1 BET surface area, grain size, ionic radius and lattice parameter of 600°C-calcined $Ce_{0.8}M_{0.2}O_{2-\delta}$ with non-lanthanide dopants. 31

2.2 BET surface area, grain size, ionic radius and lattice parameter of 600°C-calcined $Ce_{0.8}M_{0.2}O_{2-\delta}$ with lanthanide dopants. 33

2.3 BET surface areas (m^2/g) of $Ce_{1-x}M_xO_{2-\delta}$ calcined at 600°C and 800°C. 35

3.1 Characteristics of 500°C-calcined 50 wt% MO_x-50 wt% CuO mixed oxides. SO_2 adsorption was established for each material when breakthrough was attained in a feed of 130 ppm SO_2 and 1% O_2 in He at GHSV ~ 120,000 hr^{-1} and 400°C. Desorption was achieved by introducing 1% O_2 in He at 200°C, and then 2000 ppm CO in He at GHSV ~ 120,000 hr^{-1} and 200-700°C (ramp = 1°C/min). 57

3.2 BET surface area and XRD grain size of 500°C-calcined Cr_2O_3-CuO mixed oxides. 60

3.3 SO_2 adsorption/desorption over 500°C-calcined Cr_2O_3-CuO mixed oxides. A feed of 130 ppm SO_2 and 1% O_2 in He at GHSV ~ 240,000 hr^{-1} and 400°C was used for a two-hour adsorption. Desorption was conducted by introducing 1% O_2 in He at 200°C, and then 2000 ppm CO in He at GHSV ~ 240,000 hr^{-1} and 200-600°C (ramp = 1°C/min). 61

3.4 Effect of dopant composition on the surface area and grain size of 500°C-calcined $Cu_{0.95}M_{0.05}Cr_2O_4$. Lattice parameters of $Cu_{0.95}M_{0.05}Cr_2O_4$ were determined following calcination to 1000°C. 66

3.5 SO_2 adsorption/desorption over 500°C-calcined $Cu_{0.95}M_{0.05}Cr_2O_4$. A feed of 130 ppm SO_2 and 1% O_2 in He at GHSV ~ 240,000 hr^{-1} and 400°C was used for a two-hour adsorption. Desorption was conducted by introducing 1% O_2 in He at 200°C, and then 2000 ppm CO in He at GHSV ~ 240,000 hr^{-1} and 200-500°C (ramp = 1°C/min). 66

3.6 Effect of dopant composition on the surface area and grain size of 500°C-calcined $CuCr_{1.9}M_{0.1}O_4$. Lattice parameters of $CuCr_{1.9}M_{0.1}O_4$ were determined following calcination to 1000°C. 68

3.7 SO_2 adsorption/desorption over 500°C-calcined $CuCr_{1.9}M_{0.1}O_4$. A feed of 130 ppm SO_2 and 1% O_2 in He at GHSV ~ 240,000 hr^{-1} and 400°C was used for a two-hour adsorption. Desorption was conducted by introducing 1% O_2 in He at 200°C, and then 2000 ppm CO in He at GHSV ~ 240,000 hr^{-1} and 200-500°C (ramp = 1°C/min). 69

3.8 Effect of dopant concentration on surface area and grain size of 500°C-calcined $CuCr_{2-y}Co_yO_4$. Lattice parameters of $CuCr_{2-y}Co_yO_4$ were determined following calcination to 1000°C. 72

3.9	SO_2 adsorption/desorption over 500°C-calcined $CuCr_{1-y}Co_yO_4$. A feed of 130 ppm SO_2 and 1% O_2 in He at GHSV ~ 240,000 hr^{-1} and 400°C was used for a two-hour adsorption. Desorption was conducted by introducing 1% O_2 in He at 200°C, and then 2000 ppm CO in He at GHSV ~ 240,000 hr^{-1} and 200-500°C (ramp = 1°C/min).	73
3.10	Surface area and grain size of 500°C-calcined $CuCr_{1.9}Co_{0.1}O_4$, $CuO/CuCr_{1.9}Co_{0.1}O_4$ (synthesized by 4 different methods) and $CuO/CuCr_2O_4$. Lattice parameters of the $CuCr_2O_4$ phase were determined following calcination at 1000°C.	76
3.11	SO_2 adsorption/desorption over 500°C-calcined materials. A feed of 130 ppm SO_2 and 1% O_2 in He at GHSV ~ 240,000 hr^{-1} and 400°C was used for a two-hour adsorption. Desorption was conducted by introducing 1% O_2 in He at 200°C, and then 2000 ppm CO in He at GHSV ~ 240,000 hr^{-1} and 200-500°C (ramp = 1°C/min).	78
3.12	SO_2 adsorption/desorption averaged over 5-pulses during alternating cycles of 0.5% O_2 in He (10 min) and 1% CO in He (10 min) over 500°C-calcined materials. A constant feed of 300 ppm SO_2 was introduced at GHSV of 120,000 hr^{-1} and 400°C. Prior to each pulse, a 1-min He purge was fed.	83
4.1	Physical characteristics of 300°C-calcined ZnO prepared by carbonate and hydroxide synthesis routes.	91
4.2	Effect of calcination atmosphere on the characteristics of 200°C-calcined ZnO.	96
4.3	Weight ratios of Zn to secondary metals analyzed by ICP and XPS for nominally 9 wt% TiO_2-, ZrO_2- and V_2O_5-coated ZnO nanoparticles calcined to 500°C.	102

List of Symbols

a	unit cell dimension
A_s	BET surface area
c	unit cell dimension
E_a	Arrhenius activation energy
k	reaction rate constant
k_o	preexponential factor
R	ideal gas constant (kcal/mol/K)
r_i	reaction rate
r_o	theoretical grain radius
r_u	unreacted radius
Vo_e	extrinsic oxygen vacancy
Vo_i	intrinsic oxygen vacancy
X	conversion at breakthrough
x	A-site dopant concentration
y	B-site dopant concentration
δ	oxygen vacancy concentration
ρ	metal oxide density

1 – Background and Research Motivation

Air pollution has been recognized in the U.S. as an environmental issue since the 1950's, and legislation has been adopted since 1970 on emissions control. A large portion of the emissions are attributed to mobile combustion sources. Combustion processes generate hazardous gases that have adverse effects on human health and plant life, and contribute to smog formation, acid rain and global climate change [1]. Automobiles are responsible for 63%, 34% and 38% of carbon monoxide, hydrocarbon and nitrogen oxides emissions, respectively. Even with improved catalytic converter technology and fuel efficiency, increases in vehicle number and use led to little decline in automotive emissions since 1980 [2]. Thus, further legislation is forthcoming with the eventual goal of zero emission.

With more stringent regulations on mobile source emissions, improved environmental control has become a major research priority worldwide. CO, hydrocarbon and NO_x emissions will be limited to 1.7 g/mile, 0.125 g/mile, and 0.2 g/mile, respectively, by 2004 [1]. To meet these regulations, efforts are devoted towards (1) the improvement of catalytic converter activity, (2) the development of lean-burn combustion technology, and (3) the use of alternative power sources such as fuel cells to provide efficient, environmentally sound operation. Utilizing current combustion technology in conjunction with improved catalytic converter properties shows the most promise for meeting the short-term emissions regulations.

1.1 Improved Low-Temperature Oxidation for Catalytic Converters

Automotive emissions are currently controlled through catalytic converters that employ a three-way catalyst to oxidize hydrocarbons and CO, while reducing NO_x. The key components in this catalyst include noble metals to improve catalytic activity, CeO_2 as an oxygen buffer, γ-Al_2O_3 as a high surface area support, and additives such as La_2O_3 or BaO that promote catalytic activity and thermal stability of the system [3]. There has been a great deal of recent interest on enhancing the oxygen storage capacity of catalytic converters through the use of CeO_2-containing mixed oxides, which would provide increased oxygen availability and potentially reduce the catalyst activation temperature. These characteristics would have a significant impact on the catalytic converter

performance, reducing the overall emissions of CO and hydrocarbons especially during the cold-start period.

1.1.1 Current Technology

CeO_2 possesses a number of properties that help improve the catalytic converter performance. The presence of CeO_2 provides for the stable and ultrahigh dispersion of noble metals [4-7]. CeO_2 nanocrystals can also stabilize the high surface area γ-Al_2O_3 support, inhibiting its transformation to the inactive α phase [4]. From a catalytic standpoint, CeO_2 can function in conjunction with noble metals to promote the water-gas shift reaction [8, 9]. It is critical towards maintaining the gas stream oxidation environment to near-stoichiometry by storing oxygen during oxidizing conditions and releasing the oxygen during reducing conditions [5, 7, 10]. CeO_2 may possess +3 and/or +4 oxidation states at elevated temperatures, changing to $CeO_{2-\delta}$ in a reducing atmosphere and then reoxidizing to CeO_2 in an oxidizing atmosphere [11]. Ceria takes on the reduced forms of $CeO_{1.96}$ and $CeO_{1.83}$ at 600°C in air and hydrogen, respectively, with an attractive reduction capacity of $\Delta\delta = 0.13$ [12].

The oxidation/reduction properties of CeO_2 have proven to be quite effective at modifying the high-temperature exhaust stream redox potential. However, the peak temperature for oxygen desorption from ceria in a stream with 10% H_2 is 482°C [12], which is too high to control emissions at 100–300°C during the cold-start and engine warm-up cycle [3]. The addition of palladium or platinum to ceria can promote a low-temperature activity at 225°C [13]. However, the surface available oxygen species that are involved in this system represent only a small portion of the total available oxygen species. Conventional CeO_2 in the catalytic converter system also suffers from low surface area and stability, resulting in performance degradation over time.

1.1.2 Research Direction

To improve the thermal stability and oxygen storage capacity of CeO_2, current research on catalytic converter systems has focused on the use of dopants. ZrO_2 has been introduced within the CeO_2 lattice to enhance high-temperature stability [12, 14-20]. ZrO_2 typically has a monoclinic structure, but it adopts the fluorite-based cubic structure

of CeO_2 when introduced as a dopant, and does not form a separate phase at a Zr concentration of < 25 at% [19]. The surface area of CeO_2 can be increased from 62 m^2/g to 70 m^2/g at 600°C with the introduction of 10 at% ZrO_2, with a minor increase in oxygen storage capacity ($\Delta\delta$) from 0.13 to 0.14 [12]. Through controlled synthesis, recent research has obtained surface areas as high as 120 m^2/g for 20 at% Zr-doped CeO_2 calcined to 550°C [20].

To provide for greater oxygen storage capacity, altervalent dopants have been examined. Trivalent and divalent cations that can introduce extrinsic vacancies to provide improved oxygen diffusion are of particular interest. Specifically, Ca^{2+} doping has shown the highest oxygen availability, possibly because the oxygen vacancy size correlates well with the size of the lattice oxygen [12]. Unfortunately, this dopant reduces the thermal stability of CeO_2. Another concept that has been examined for increasing oxygen storage capacity involves the use of a secondary metal oxide, such as Pr_6O_{11} and Tb_4O_7. These lanthanide oxides are also stable in +3 and +4 valence states, but favor the former to a greater extent than CeO_2 [21]. This may provide for the formation of extrinsic vacancies that are active for oxidation, since the presence of CeO_2 enhances the ability of both Pr and Tb for adopting the +4 oxidation state. CeO_2-Pr_6O_{11} and CeO_2-Tb_4O_7 have shown promise for higher oxygen storage capacities than pure CeO_2 [22, 23]. However, thermal stability and phase segregation remain as challenging issues with these mixed oxides by conventional synthesis.

1.2 Adsorbents for Lean-Burn Engines

A lean-burn engine operates at a high air-to-fuel ratio (~ 20), which reduces NO_x generation by 87% and eliminates CO emissions [2]. However, the conventional catalytic converter is not effective at NO_x reduction under the highly oxidizing conditions. Recent research has focused on NO_x storage in the form of surface nitrate, utilizing the short fuel-rich cycles to remove and reduce the NO_x to N_2 [24-27]. BaO, SrO and CaO possess the desired NO_x adsorption properties, forming thermally stable surface nitrates $\leq$ 450°C while decomposing surface nitrites $\leq$ 250°C. However, SO_2 adsorbs competitively on these materials, forming sulfates that are stable to temperatures in excess of 1000°C [26, 28, 29]. Therefore, it is necessary to remove SO_2 upstream of

the NO_x storage material during oxidizing conditions when highly stable sulfate species will likely form.

1.2.1 Current Technology

The predominant method for SO_2 removal from flue gas involves the use of lime ($Ca(OH)_2$) or limestone ($CaCO_3$) in the form of a slurry or hydrated solids. Upon absorption in the aqueous phase, SO_2 reacts with water to form sulfite and hydrogen ion. Both $Ca(OH)_2$ and $CaCO_3$ dissociate in water and react with sulfite and hydrogen ions to produce calcium sulfate, calcium sulfite, water and carbon dioxide. Addition of other basic cations, such as Mg^{+2} and Na^{+}, can aid in the SO_2 removal and lead to a higher degree of desulfurization. The reacted solids are treated and disposed of as non-hazardous waste [30].

Inherent problems in SO_2 removal with $Ca(OH)_2$ or $CaCO_3$ are associated with recovery efficiency and flue gas temperature. Although SO_2 reacts readily with Ca^{+2} ion in solution, the equilibrium constraints imposed on absorption and reaction within the liquid phase limit the removal efficiency to ~ 95% [30]. Liquid removal systems also require the temperature reduction of the flue gas, which must then be reheated prior to release. Thus, liquid absorption processes are not suitable for treating mobile emissions, and with a conversion of only 9%, solid calcium adsorbents are not a viable candidate for automotive applications.

1.2.2 Research Direction

Several materials have been studied for SO_2 adsorption with limited success. Among these, supported copper oxide and activated carbon have shown the most promise. The high regenerability and SO_2 capacity of these adsorbents make them attractive.

CuO/Al_2O_3 can remove 90% of the SO_2 present in a flue gas stream. Thermodynamics of this reaction favor 100% conversion below 450°C [30]. The first step in SO_2 removal by CuO is the catalytic oxidation of SO_2 to SO_3. The surface adsorbed SO_3 then reacts directly with the CuO surface to produce $CuSO_4$. The sorbent can be regenerated directly at ≥ 700°C, but this can lead to loss of adsorption activity and mechanical strength [31]. Regeneration using various reducing agents such as H_2, CH_4 or

CO can be achieved at 400°C. The rate of regeneration with H_2 is 4 times faster than that with CH_4 under the same conditions. The formation of Cu species during the regeneration process activates H_2, thereby catalyzing the reduction and increasing the reaction rate. Although regeneration with CH_4 is slower, 90% regenerability can be obtained compared to a maximum of 80% attained with H_2 (due to the undesired formation of CuS as a side-reaction in H_2 reduction [32]). Following regeneration, Cu is oxidized *in situ* by the feedstream.

Activated carbon can be used to treat flue gas emissions, removing up to 95% of SO_2 and 80% of NO_x. SO_2 reacts over activated carbon to form H_2SO_4 in the presence of water and oxygen at 80-120°C [33]. The reaction begins with oxygen chemisorption onto carbon to form an activated C(O) intermediate, which can react with gas-phase SO_2 to form SO_3. SO_3 can be converted to sulfuric acid in the presence of adsorbed water. Surface adsorbed water condenses and dissolves the sulfuric acid, continuously regenerating active sites on the carbon surface. The reaction of SO_2 with the surface C(O) intermediate continues until the condensed water within the pores is saturated with sulfuric acid. The adsorbent can then be regenerated by thermally decomposing the sulfuric acid above 360°C or by aqueous washes.

Although both CuO/Al_2O_3 and activated carbon operate with $\geq$ 90% removal efficiency and are regenerable, the regeneration temperature of CuO/Al_2O_3 (~ 440°C in CO) and the adsorption temperature for activated carbon (80-120°C) make these solid sorbents unattractive for the lean-burn application. It would be ideal to achieve an efficient SO_2 adsorbent that functions and regenerates reproducibly at $\leq$ 400°C.

1.3 H_2S Removal Technology for Automotive Fuel Cells

Due to a lack of H_2 storage technology and distribution infrastructure, fuel cell development for mobile sources has been focused on providing H_2 at the necessary rate while minimizing the expense and frequency of refueling. Gasoline, methanol or methane are attractive fuels for H_2 production since both storage technology and high energy-to-volume ratios allow for long travel distances. The current distribution infrastructure also allows for ease of refueling for gasoline and methane. However, on-

board cracking and reforming processes are necessary to convert the hydrocarbon-based fuels to hydrogen.

Hydrocarbon fuels often contain sulfur (e.g. H_2S) as a byproduct, which can lead to poisoning of the reforming catalyst or the fuel cell. For most catalytic applications, sulfur poisoning would not only reduce conversion by as much as an order of magnitude [34], but also decrease selectivity and catalyst life. Although current technology exists for treating gas-phase H_2S, absorbent efficiency on the order of 100% is necessary in mobile applications to minimize the weight requirements.

1.3.1 Current Technology

Traditionally, liquid-phase amine systems have been used to remove H_2S from low-temperature gas streams. For high-temperature applications, however, liquid systems are not practical because the cooled gas stream would have to be reheated prior to introduction to the reaction system, leading to higher cooling and heating costs. Thus, solid absorbents have been developed in place of liquid-phase systems. The most widely used solid absorbent for the removal of H_2S at low concentrations is ZnO. Thermodynamics for H_2S sorption by ZnO are quite favorable with an equilibrium H_2S concentration of 4.2 ppm at 540°C [35]. H_2S concentrations lower than the equilibrium value (< 0.1 ppm) have been achieved by ZnO, making its use attractive.

The mechanism for H_2S reaction with ZnO has been studied extensively [35-40]. H_2S first diffuses to the absorbent surface where it reacts to form ZnS and H_2O. Once reacted, the sulfide ion can diffuse through the ZnO lattice at a temperature above 350°C, allowing more oxygen to diffuse to the solid surface. As the reaction progresses, the lattice structure begins to change from the hexagonal ZnO to cubic ZnS, creating a dense ZnS outer shell around the ZnO particle. This limits the lattice diffusion, changing the rate-limiting step from surface reaction to bulk diffusion, and resulting in incomplete conversion of the ZnO absorbent [41, 42]. ZnO also suffers from problems in regeneration and in zinc loss above 700°C [36]. Temperatures above 600°C are necessary for ZnO regeneration so as to prevent the formation of surface sulfates in converting ZnS to ZnO. However, substantial sintering of ZnO would occur above 350°C, resulting in a significant reduction in surface area [38]. This low thermal stability

reduces the conversion or absorption capacity of ZnO in regeneration cycles, making this material less attractive for repeated use.

1.3.2 Research Direction

Recent research has focused on the use of ZnO-based mixed oxides that act as composite systems with increased stability [35, 43, 44]. In some instances, these materials can promote the regeneration process by either lowering the regeneration temperature required or by providing greater stability for high-temperature regeneration. A great deal of research interests has been directed at porous ZnO stabilized with Fe_2O_3 or TiO_2 to form $ZnFe_2O_4$ or $ZnTiO_3$, respectively [35, 44].

Highly porous $ZnFe_2O_4$ would react with H_2S to form a mixture of ZnS and FeS. The H_2S concentration in the effluent can be reduced to less than 1 ppm with both dense and porous $ZnFe_2O_4$ particles. A sorbent conversion at breakthrough (where H_2S concentration > 1 ppm) of > 95% can be achieved at 600°C with $ZnFe_2O_4$. Once breakthrough is reached, the sorbent can be regenerated in air at 600°C by reoxidizing the iron and zinc sulfides. However, after four regeneration cycles, the porous $ZnFe_2O_4$ has a substantially reduced conversion of 60% due to sintering, zinc evaporation and incomplete regeneration [35].

$ZnTiO_3$ can retain a surface area of ~ 20 m^2/g at 750°C, compared to < 7 m^2/g for pure ZnO [44]. The increased stability allows $ZnTiO_3$ to be used at temperatures as high as 600°C, achieving a conversion of ~ 100%. $ZnTiO_3$ can be regenerated by reoxidizing the ZnS at 700°C. However, its conversion is substantially decreased after multiple regenerations. Both zinc titanate and zinc ferrite show improved performance for high-temperature applications, however, maximizing the active ZnO content while minimizing grain growth are necessary to attain high efficiency for mobile applications.

1.4 Research Motivation and Approach

The motivation of this research is to develop novel metal oxide nanocomposites for automotive emissions control through advanced oxygen storage, SO_2 adsorption and H_2S absorption technologies. During the past decade, significant research efforts have been devoted to nanostructure processing as a means to achieve materials with ultrafine microstructures for structural, catalytic, electronic and optical applications [45-49].

Nanocrystalline materials possess an ultrahigh surface-to-volume ratio, which translates to greater surface reactivity and reduced diffusion depth. These properties as well as the potential for improved grain size stability make metal oxide nanocomposites attractive for automotive emissions remediation.

For oxygen storage, it is important to focus on compositional selection and microstructural control to provide improved oxygen accessibility at low temperatures as well as high thermal stability. Through nanocrystalline processing, we can tailor chemically homogeneous CeO_2-based nanocomposites for enhanced oxygen storage capacity, redox kinetics and thermal stability. By improving upon the oxygen storage capacity, the loading of CeO_2-based oxygen buffer materials can be minimized. Having a material with superior oxygen storage capacity will also facilitate the redox reactions under the oxidizing and reducing atmospheres of the automotive exhaust stream. This may also reduce the amount of active noble metals required for the catalytic reactions. Thus, we can achieve a more effective and economical material system for catalytic converter applications.

For SO_2 adsorption, it would be critical to attain high adsorbent capacity and regenerability at temperatures $\leq$ 400°C. CuO-based nanocomposites are examined as adsorbents that may allow for sulfate decomposition below 400°C for low-temperature regenerability. Nanostructure processing is employed to attain high adsorption capacity via microstructural control. Thus, by compositional manipulation and nanostructure tailoring, novel SO_2 storage materials can be designed and developed.

For H_2S absorption, ultrafine grain size and microstructure are crucial towards obtaining high absorbent capacity through multiple regeneration cycles. This research focuses on the development of ZnO-based absorbents to take advantage of the favorable equilibrium, fast kinetics and oxygen-nitrogen counter-diffusion of ZnO. Non-agglomerated nanocrystalline ZnO is synthesized to minimize the lattice diffusion distance, while facilitating H_2S interaction with the ZnO grains. To overcome the low sintering temperature of ZnO, a two-step synthesis approach is employed, involving precipitation of ZnO nanocrystals, followed by the deposition of small amounts of a secondary metal oxide on the ZnO surface to prevent contact between adjacent ZnO

grains. By suppressing grain growth and carefully selecting the secondary metal oxide, an effective and reusable H_2S absorbent can be developed.

1.5 References

[1] Turco, R. P., *Earth Under Siege: From Air Pollution to Global Climate Change*, Oxford University Press, New York, **1997**.

[2] Cooper, C. D., Alley, F. C., *Air Polution Control: A Design Approach*, 2nd ed., Waveland Press, Inc., Prospect Heights, **1994**.

[3] Delmon, B., Yates, J. T., *Stud. Surf. Sci. Catal.* **1998**, *115*, 1.

[4] Ozawa, M., Kimura, M., *J. Mater. Sci. Lett.* **1990**, *9*, 291.

[5] Su, E. C., Rothschild, W. G., *J. Catal.* **1986**, *99*, 506.

[6] Tschöpe, A., Liu, W., Flytzani-Stephanopoulos, M., Ying, J. Y., *J. Catal.* **1995**, *157*, 42.

[7] Yao, H. C., Yao, Y. F. Y., *J. Catal.* **1984**, *86*, 254.

[8] Schlatter, J. C., Mitchell, P. J., *Ind. Eng. Chem. Prod. Res. Dev.* **1980**, *19*, 288.

[9] Kim, G., *Ind. Eng. Chem. Prod. Res. Dev.* **1982**, *21*, 267.

[10] Shyu, J. Z., Weber, W. H., Gandhi, H. S., *J. Phys. Chem.* **1988**, *92*, 4964.

[11] Kofstad, P., *Nonstoichiometry, Diffusion, and Electrical Conductivity in Binary Metal Oxides*, John Wiley & Sons, Inc., New York, **1972**.

[12] Zhang, Y., Andersson, S., Muhammed, M., *Appl. Catal. B: Environ.* **1995**, *6*, 325.

[13] Logan, A. D., Shelef, M., *J. Mater. Res.* **1994**, *9*, 468.

[14] Balducci, G., Kaspar, J., Fornasiero, P., Graziani, M., Islam, M. S., *J. Phys. Chem. B* **1998**, *102*, 557.

[15] Masui, T., Ozaki, T., Machida, K., Adachi, G., *J. Alloy Compd.* **2000**, *303*, 49.

[16] Masui, T., Nakano, K., Ozaki, T., Adachi, G., Kang, Z., Eyring, L., *Chem. Mater.* **2001**, *13*, 1834.

[17] Madier, Y., Descorme, C., Le Govic, A. M., Duprez, D., *J. Phys. Chem. B* **1999**, *103*, 10999.

[18] Rossignol, S., Micheaud-Especel, C., Duprez, D., *Stud. Surf. Sci. Catal.* **2000**, *130*, 3327.

[19] Ozawa, M., Kimura, M., Isogai, A., *J. Alloy Compd.* **1993**, *193*, 73.

[20] Gonzalez-Velasco, J. R., Gutierrez-Ortiz, M. A., Marc, J. L., Botas, J. A., Gonzalez-Marcos, M. P., Blanchard, G., *Appl. Catal. B: Environ.* **1999**, *22*, 167.

[21] Kang, Z. C., Eyring, L., in *Key Engineering Materials, Vol. 155-156* (Ed.: Boulesteix, C.), Trans Tech Publications Ltd., Switzerland, **1998**, pp. 301.

[22] Blanco, G., Calvino, J. J., Cauqui, M. A., Corchado, P., Lopez-Cartes, C., Colliex, C., Perez-Omil, J. A., Stephan, O., *Chem. Mater.* **1999**, *11*, 3610.

[23] Shigapov, A. N., Jen, H.-W., Graham, G. W., Chun, W., McCabe, R. W., *Stud. Surf. Sci. Catal.* **2000**, *130*, 1373.

[24] Machida, M., in *Catalysis, Vol. 15* (Ed.: Spivey, J. J.), Royal Society of Chemistry, Cambridge, **2000**, pp. 73.

[25] Mahzoul, H., Brilhac, J. F., Gilot, P., *Appl. Catal. B: Environ.* **1999**, *20*, 47.

[26] Feeley, J., Deeba, M., Farrauto, R. J., *Stud. Surf. Sci. Catal.* **1998**, *116*, 529.

[27] Bogner, W., Kramer, M., Krutzsch, B., Pischinger, S., Voigtlander, D., Wenninger, G., Wirbeleit, F., Brogan, M. S., Brisley, R. J., Webster, D. E., *Appl. Catal. B: Environ.* **1995**, *7*, 153.

[28] Adams, K. M., Cavataio, J. V., Hammerle, R. H., *Appl. Catal. B: Environ.* **1996**, *10*, 157.

[29] Engstrom, P., Amberntsson, A., Skoglundh, M., Fridell, E., Smedler, G., *Appl. Catal. B: Environ.* **1999**, *22*, L241.
[30] Kohl, A. L., Riensenfeld, F., *Gas Purification*, Gulf Publishing Co., Houston, **1979**.
[31] Kiel, J. H. A., Prins, W., Vanswaaij, W. P. M., *Appl. Catal. B: Environ.* **1992**, *1*, 13.
[32] Macken, C., Hodnett, B. K., *Ind. Eng. Chem. Res.* **1998**, *37*, 2611.
[33] Lizzio, A. A., DeBarr, J. A., *Fuel* **1996**, *75*, 1515.
[34] Irandoust, S., Edvardsson, J., *J. Am. Oil Chem. Soc.* **1993**, *70*, 1149.
[35] Tamhankar, S. S., Bagajewicz, M., Gavalas, G. R., Sharma, P. K., Flytzani-Stephanopoulos, M., *Ind. Eng. Chem. Prod. Res. Dev.* **1986**, *25*, 429.
[36] Westmoreland, P. R., Gibson, J. B., Harrison, D. P., *Environ. Sci. Technol.* **1977**, *11*, 488.
[37] Westmoreland, P. R., Harrison, D. P., *Environ. Sci. Technol.* **1976**, *10*, 659.
[38] Ranade, P. V., Harrison, D. P., *Chem. Eng. Sci.* **1981**, *36*, 1079.
[39] Rajeswara, R. T., Kumar, R., *Chem. Eng. Sci.* **1982**, *37*, 987.
[40] Gibson, J. B., Harrison, D. P., *Ind. Eng. Chem. Prod. Res. Dev.* **1980**, *19*, 231.
[41] Richardson, J. T., *Catalyst Handbook*, Wolfe Scientific Books, London, **1970**.
[42] Twigg, V., *Catalyst Handbook*, 2nd ed., Wolfe Publishing Ltd., Frome, **1989**.
[43] Sasaoka, E., Sada, N., Manabe, A., Uddin, M. A., Sakata, Y., *Ind. Eng. Chem. Res.* **1999**, *38*, 958.
[44] Lew, S., Jothimurugesan, K., Flytzani-Stephanopoulos, M., *Ind. Eng. Chem. Res.* **1989**, *28*, 535.
[45] Dag, O., Kuperman, A., Ozin, G. A., *Adv. Mater.* **1995**, *7*, 72.
[46] Ying, J. Y., *AIChE J.* **2000**, *46*, 1902.
[47] Ying, J. Y., Sun, T., *J. Electroceram.* **1997**, *1*, 219.
[48] Siegel, R. W., *Ann. Rev. Mater. Sci.* **1991**, *21*, 559.
[49] Gleiter, H., *Prog. Mater. Sci.* **1989**, *33*, 223.

2 - Rare Earth Oxide Nanocomposites for Oxygen Storage Applications

2.1 Introduction

Realizing new catalytic converter or lean-burn engine technology would require improved oxygen storage materials with substantial oxygen accessibility at low temperatures. Thus far, ceria has been employed in treating exhaust streams due to its attractive oxidation/reduction properties. However, the peak temperature for oxygen desorption from ceria in a stream containing 10% hydrogen is 482°C [1]. This would not satisfy the demand of emissions control during the cold-start and engine warm-up cycle (100-300°C) [2] or downstream of a NO_x storage system (400°C) [3]. The addition of palladium or platinum to ceria can promote redox activity at 225°C [4], however, the surface available oxygen species that are involved in this system represent only a small portion of the total available oxygen. Ceria in conventional catalytic converter systems also suffers from low surface area and stability, resulting in performance degradation over time. In order to meet the automotive emissions standards, researchers have attempted to correlate the overall oxygen storage capacity and microstructure stability with the low-temperature catalytic activity of ceria. Improved structural stability and chemical/electronic characteristics of ceria would not only impact the environment by providing better control of automotive pollutants, but also reduce the cost associated with minimizing the quantity of noble metals needed for the emissions remediation.

Recent research has focused on the doping of secondary metal oxides to improve the thermal stability and oxygen accessibility of ceria [1, 4-6]. By introducing metal oxides (e.g. ZrO_2) that adopt a similar crystal structure as CeO_2, or metal dopants with a similar ionic radius as Ce^{+4}, it is possible to improve upon ceria's thermal and reduction stability [1, 7-13]. The creation of intrinsic vacancies (Vo_i) within CeO_2 upon exposure to a reducing gas (R) can then be accomplished more readily, providing improved oxygen accessibility:

$$CeO_2 + xR = CeO_2 + xRO + xVo_i \qquad (2.1)$$

When the dopant ion possesses a lower valence state, extrinsic vacancies (Vo_e) will be formed to further improve the oxygen diffusion:

$$CeO_2 + xM^{+3} = Ce_{1-x}M_xO_2 + xCe^{+4} + x/2Vo_e \qquad (2.2)$$

The ideal material would have extrinsic vacancies to promote oxygen diffusion, as well as stability for both intrinsic vacancies formation and thermal treatment.

Our research has focused on studying the effect of dopants on ceria's thermal stability, oxygen accessibility, oxygen storage capacity and catalytic oxidation activity. For low-temperature applications such as downstream of a NO_x storage system, thermal stability is not as critical an issue. However, for better emissions control in catalytic converters, the ability to operate at temperatures in excess of 1000°C would be important. Thus, our materials development efforts will focus on enhancing low-temperature oxygen accessibility as well as high-temperature thermal stability.

2.2 Experimental

2.2.1 Materials Synthesis

Doped CeO_2 materials were synthesized by chemical co-precipitation using either ammonium hydroxide (NH_4OH) or tetra(n-butyl) ammonium hydroxide (TBAH, Alfa Aesar, 55 wt% in water). Zirconyl chloride (Alfa Aesar) was used to introduce Zr into CeO_2. For all other dopants, metal nitrate salts (Alfa Aesar) were used as precursors to prevent surface contamination by residual chlorides. A typical precipitation involved the dropwise addition of 0.2 M mixed nitrate solution to a 2:3 NH_4OH-water solution under vigorous stirring to achieve a final pH of 10. The precipitate was allowed to age for 18 hours before recovery by centrifuging at 3000 rpm for > 10 min and decanting the supernatant. After three isopropanol washes to remove unused precursor, the recovered precipitate was dried at 25°C. It was then ground to break up loose agglomerates and calcined at 600-1200°C (ramp: 2°C/min).

2.2.2 Structural Characterization

The surface area of the powders was determined from nitrogen adsorption analysis by the five-point BET (Brunauer-Emmett-Teller) method using a Micromeritics ASAP 2000 gas adsorption analyzer. Phase identification was performed by powder X-ray diffraction (XRD) using a Siemens D5000 θ-θ diffractometer (45 kV, 40 mA, Cu-K_α). Grain size was obtained from the peak broadening analysis of the <111> reflection of CeO_2 ($2\theta = 28.55°$) using Scherrer's method after correcting for instrumental line broadening. The lattice parameter was calculated from the <200> peak position of CeO_2

and correcting for instrumental error using the <111> peak of a silver reference. High-resolution transmission electron microscopy (HRTEM) was performed using a JEOL 2010 microscope (200 kV).

2.2.3 Temperature-Programmed Reduction and Catalytic CO Oxidation Studies

Reducibility of materials as a function of temperature was examined with a Perkin Elmer System 7HT Thermal Gravimetric Analyzer (TGA). Samples were first pretreated to 800°C in oxygen for 30 min prior to cooling to 150°C to ensure complete oxidation and to eliminate surface contaminants. After a He purge at 150°C to remove weakly absorbed oxygen, a stream of 2.5% H_2 in He was introduced and the temperature was ramped to 800°C at a rate of 5°C/min.

A vertical tubular flow reactor was used to perform catalytic CO oxidation studies over various doped CeO_2 materials (Figure 2.1). The sample was supported on a bed of quartz wool in a ¼"-O.D. quartz reactor tube. An Omega K-type thermocouple protected by a quartz sheath was used in conjunction with a vertically mounted Lindberg tube furnace and an Omega temperature controller to maintain the reaction temperature (100-500°C) within 2°C. Sierra and MKS mass flow controllers were used to control the feedstream composition and maintain the flow rate at a constant space velocity of ~ 120,000 hr^{-1}. The effluent stream was analyzed by a Hewlett Packard 6890 gas chromatograph operating with a thermal conductivity detector to quantify CO and CO_2. Prior to analysis, each material was pressed at 175 lb/in^2, crushed and sieved to 60 mesh to ensure consistent interparticle diffusion and minimal pressure drop. The catalyst weight was varied from 50 mg to 120 mg to maintain a constant bed height of 4 mm.

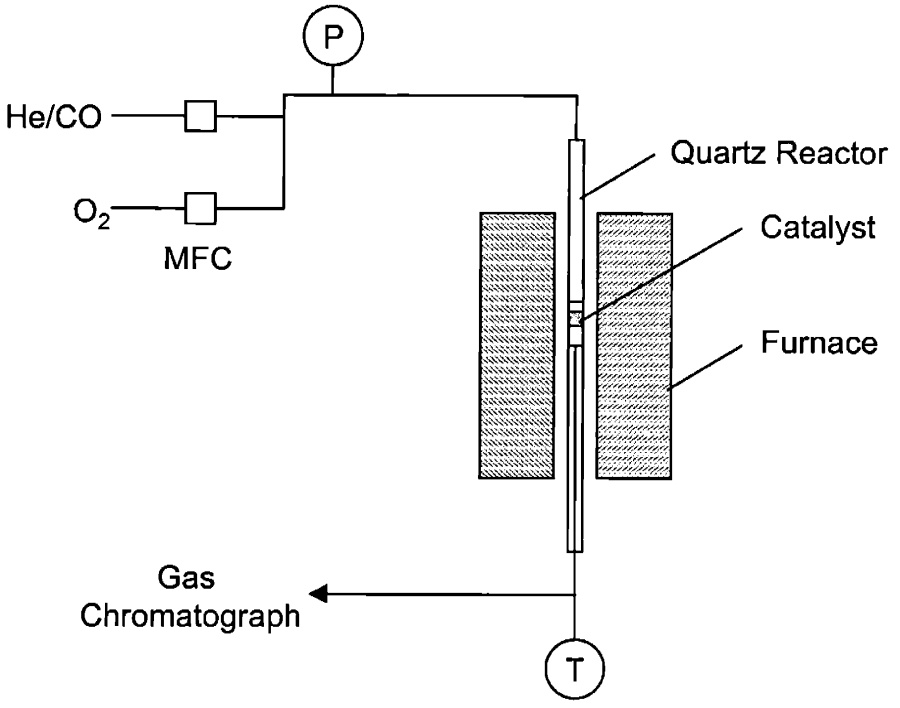

Figure 2.1 Schematic of reactor setup.

2.3 Results and Discussion

2.3.1 Structural Characteristics and Stability of $Ce_{1-x}M_xO_{2-\delta}$ Nanocomposites

Various $Ce_{1-x}M_xO_{2-\delta}$ materials containing transition metal, base metal and lanthanide dopants were synthesized by chemical co-precipitation. For $Ce_{0.8}M_{0.2}O_{2-\delta}$ with non-lanthanide dopants, a pure CeO_2 phase was maintained after calcination to 1200°C only by those doped with Ca, Y, Sc and Zr. Thus, these four non-lanthanide dopants were examined in detail. Pr and Tb were selected as lanthanide dopants because they shared similar oxide crystal structure as CeO_2 and possessed variable oxidation states. Sm was also chosen as a lanthanide dopant for its +2 and +3 oxidation states as well as its ability to introduce intrinsic vacancies. Each $Ce_{1-x}M_xO_{2-\delta}$ system was compared with CeO_2 and $Ce_{1-x}Zr_xO_{2-\delta}$.

2.3.1.1 $Ce_{0.8}M_{0.2}O_{2-\delta}$ with Non-Lanthanide Dopants

$Ce_{0.8}M_{0.2}O_{2-\delta}$ with Ca, Sc, Y and Zr dopants were analyzed for <111> grain size, surface area and lattice shift (Table 2.1). The materials doped with Ca, Sc and Zr maintained ultrafine grain sizes after calcination at 600°C (7.1 nm, 6.1 nm and 5.4 nm,

respectively). Y-doped ceria showed a similar grain size (10.5 nm) as pure CeO_2 (9.8 nm). Surface areas for the doped ceria systems were found to be significantly lower than that of pure CeO_2 (99 m^2/g). The relative a_{200} peak positions of the various $Ce_{0.8}M_{0.2}O_{2-\delta}$ materials were consistent with the differences in the dopant's ionic radius ($Ca^{+2} > Ce^{+4} \sim Y^{+3} > Zr^{+4} > Sc^{+3}$ [14]).

Table 2.1 BET surface area, grain size, ionic radius [14] and lattice parameter of 600°C-calcined $Ce_{0.8}M_{0.2}O_{2-\delta}$ with non-lanthanide dopants.

M Dopant	Surface Area (m^2/g)	Grain Size (nm)	Ionic Radius (Å)	a_{200} (Å)
Ca	34	7.1	0.99	5.421
Sc	59	6.1	0.73	5.376
Y	68	10.5	0.89	5.407
Zr	78	5.4	0.79	5.379
Ce	99	9.8	0.92	5.409

Figure 2.2 shows that $Ce_{0.8}Sc_{0.2}O_{2-\delta}$ and $Ce_{0.8}Zr_{0.2}O_{2-\delta}$ both maintained a smaller grain size of < 11 nm compared to CeO_2 (20 nm) upon calcination at 800°C. $Ce_{0.8}Zr_{0.2}O_{2-\delta}$ demonstrated particularly high thermal stability at 1000°C, with a grain size of 30 nm compared to 99 nm for pure CeO_2. $Ce_{0.8}Sc_{0.2}O_{2-\delta}$ underwent more grain growth than $Ce_{0.8}Zr_{0.2}O_{2-\delta}$ with heat treatment to 1000°C, showing a grain size of 42 nm. $Ce_{0.8}Y_{0.2}O_{2-\delta}$ also exhibited a grain size of < 50 nm at 1000°C, although it possessed a larger grain size than CeO_2 at 800°C.

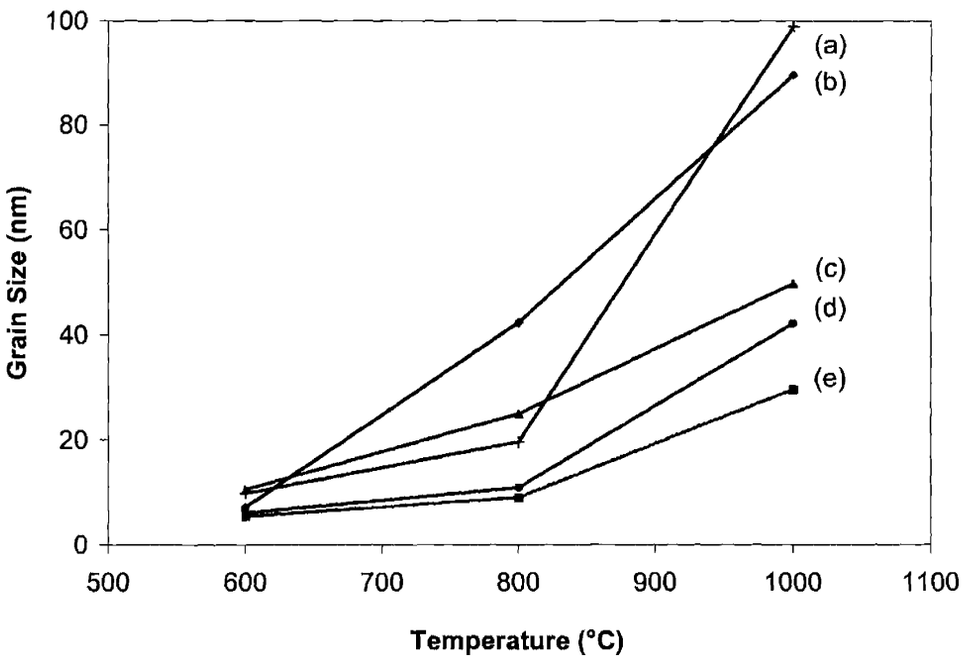

Figure 2.2 Effect of calcination temperature on the XRD grain size of (a) CeO_2, (b) $Ce_{0.8}Ca_{0.2}O_{2-\delta}$, (c) $Ce_{0.8}Y_{0.2}O_{2-\delta}$, (d) $Ce_{0.8}Sc_{0.2}O_{2-\delta}$ and (e) $Ce_{0.8}Zr_{0.2}O_{2-\delta}$.

2.3.1.2 $Ce_{0.8}M_{0.2}O_{2-\delta}$ with Lanthanide Dopants

The XRD grain sizes of $Ce_{0.8}M_{0.2}O_{2-\delta}$ doped with Sm and Tb calcined to 600 °C were ~ 10 nm (Table 2.2). Pure and Pr-doped CeO_2 both achieved grain sizes of < 10 nm with high surface areas of 99 and 95 m^2/g, respectively. In contrast, the surface areas of $Ce_{0.8}Sm_{0.2}O_{2-\delta}$ and $Ce_{0.8}Tb_{0.2}O_{2-\delta}$ were significantly lower (75 and 78 m^2/g, respectively). The a_{200} lattice parameters for $Ce_{0.8}Sm_{0.2}O_{2-\delta}$ and $Ce_{0.8}Tb_{0.2}O_{2-\delta}$ followed the expected trend of lattice expansion and contraction, respectively, relative to CeO_2. For $Ce_{0.8}Pr_{0.2}O_{2-\delta}$, Pr was expected to have a mixed valence of +3 and +4 (since the most stable praseodymium oxide was Pr_6O_{11} [15, 16]). Given that Pr^{+3} and Pr^{+4} have ionic radii of 1.013 Å and 0.90 Å [14], respectively, it was not surprising that $Ce_{0.8}Pr_{0.2}O_{2-\delta}$ showed a greater a_{200} than CeO_2.

Table 2.2 BET surface area, grain size, ionic radius [14] and lattice parameter of 600°C-calcined $Ce_{0.8}M_{0.2}O_{2-\delta}$ with lanthanide dopants.

M Dopant	Surface Area (m^2/g)	Grain Size (nm)	Ionic Radius (Å)	a_{200} (Å)
Sm	75	11.7	0.96	5.432
Tb	78	10.1	0.84	5.395
Pr	95	9.6	0.90, 1.013	5.423
Ce	99	9.8	0.92	5.409

$Ce_{0.8}M_{0.2}O_{2-\delta}$ doped with Sm and Tb calcined to 800°C showed significant peak shift (with a_{200} = 5.431 Å and 5.385 Å) consistent with lattice expansion and contraction, respectively. When calcined to 800°C, $Ce_{0.8}Pr_{0.2}O_{2-\delta}$ showed only a slight peak shift (with a_{200} = 5.416 Å) compared to that in the 600°C-calcined $Ce_{0.8}Pr_{0.2}O_{2-\delta}$. This could be explained by a change in the Pr mixed oxidation states with calcination [15]. The $Ce_{0.8}M_{0.2}O_{2-\delta}$ materials with Sm, Tb and Pr dopants showed phase purity through calcination to 1200°C.

Figure 2.3 shows that $Ce_{0.8}Pr_{0.2}O_{2-\delta}$ had a fine grain size of < 15 nm while pure CeO_2 grew to 20 nm upon calcination to 800°C. Although it maintained an improved thermal stability relative to CeO_2 after calcination at 1000°C, $Ce_{0.8}Pr_{0.2}O_{2-\delta}$'s 39-nm grain size was larger than that obtained with $Ce_{0.8}Zr_{0.2}O_{2-\delta}$ (30 nm). $Ce_{0.8}Sm_{0.2}O_{2-\delta}$ and $Ce_{0.8}Tb_{0.2}O_{2-\delta}$ had similar grain sizes as CeO_2 through 800°C, but demonstrated superior thermal stability to CeO_2 upon calcination to 1000°C.

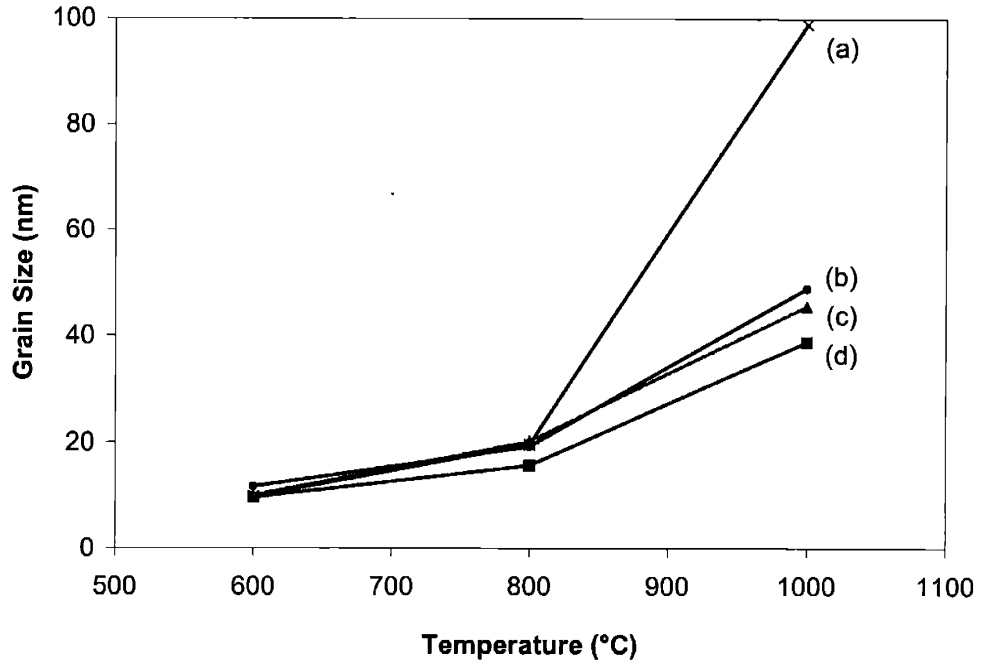

Figure 2.3 Effect of calcination temperature on the XRD grain size of (a) CeO_2, (b) $Ce_{0.8}Sm_{0.2}O_{2-\delta}$, (c) $Ce_{0.8}Tb_{0.2}O_{2-\delta}$ and (d) $Ce_{0.8}Pr_{0.2}O_{2-\delta}$.

2.3.1.3 $Ce_{1-x}M_xO_{2-\delta}$ with Zr, Pr, Tb and Sm Dopants

For $Ce_{1-x}Pr_xO_{2-\delta}$, $Ce_{1-x}Sm_xO_{2-\delta}$ and $Ce_{1-x}Zr_xO_{2-\delta}$ calcined to 800°C, x = 0.1 gave rise to the highest surface area (60, 52 and 50 m^2/g, respectively) (Table 2.3). $Ce_{1-x}Tb_xO_{2-\delta}$ achieved the highest surface area of 37 m^2/g at x = 0.2, which was only slightly higher than the 35 m^2/g obtained by pure CeO_2 at 800°C. Although its surface areas were not particularly high, the $Ce_{1-x}Tb_xO_{2-\delta}$ series maintained phase purity throughout all dopant levels in calcination to 1200°C. For $Ce_{1-x}Pr_xO_{2-\delta}$, single-phase materials were attained in calcination to 1200°C, with the exception of $Ce_{0.2}Pr_{0.8}O_{2-\delta}$, which showed phase segregation at 1000°C. $Ce_{1-x}Sm_xO_{2-\delta}$ experienced phase segregation for $x > 0.4$, showing peaks corresponding to a Sm_2O_3 secondary phase when calcined to 1000°C.

Table 2.3 BET surface areas (m^2/g) of $Ce_{1-x}M_xO_{2-\delta}$ calcined at 600°C and 800°C.

	$Ce_xPr_{1-x}O_{2-\delta}$		$Ce_xTb_{1-x}O_{2-\delta}$		$Ce_xSm_{1-x}O_{2-\delta}$		$Ce_xZr_{1-x}O_{2-\delta}$	
x	600°C	800°C	600°C	800°C	600°C	800°C	600°C	800°C
0.0	99	35	99	35	99	35	99	35
0.1	92	60	71	23	84	52	93	50
0.2	95	52	78	37	75	39	82	49
0.3	91	52	77	27	80	27	85	44
0.4	99	44	68	11	67	13	76	43
0.6	75	17	50	2	-	-	-	-
0.8	61	27	38	2	-	-	-	-
1.0	58	21	33	11	-	-	-	-

Phase purity of 1000°C-calcined $Ce_{1-x}Zr_xO_{2-\delta}$ was examined by XRD (Figure 2.4). The <111> reflection of $Ce_{1-x}Zr_xO_{2-\delta}$ materials with $x \leq 0.2$ was symmetric with no sign of a separate ZrO_2 phase. However, for $x = 0.3$ and 0.4, peak asymmetry was noted in the <111> reflection due to the presence of a second peak at $2\theta = 29.8°$ associated with the <101> reflection of tetragonal ZrO_2. Grain size analysis of these two materials indicated a ZrO_2 grain size of < 5 nm. Phase segregation for high Zr dopant levels was not unexpected since the literature has reported a Zr solubility of $x \leq 0.25$ in the CeO_2 lattice [13].

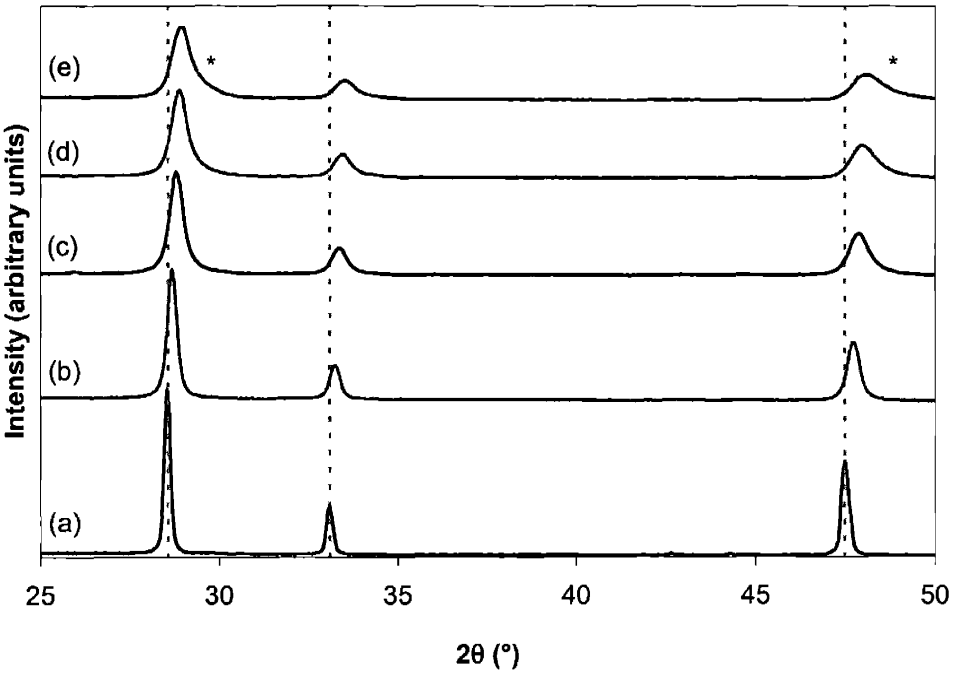

Figure 2.4 XRD patterns of 1000°C-calcined $Ce_{1-x}Zr_xO_{2-\delta}$ with x = (a) 0.0, (b) 0.1, (c) 0.2, (d) 0.3 and (e) 0.4. Tetragonal ZrO_2 <101> reflection (*) was noted for $x > 0.2$.

With the cubic Fm3m structure of CeO_2, lattice substitution should show a linear correlation with dopant concentration. This was the case for 600°C-calcined $Ce_{1-x}Sm_xO_{2-\delta}$ and $Ce_{1-x}Zr_xO_{2-\delta}$ with $x \leq 0.4$ ($R^2 > 0.98$), and $Ce_{1-x}Tb_xO_{2-\delta}$ with $0.0 \leq x \leq 1.0$ ($R^2 > 0.97$) (Figure 2.5). $Ce_{1-x}Pr_xO_{2-\delta}$, however, deviated from linearity especially for $x = 0.6$ and 0.8. Praseodymium oxides may adopt Pr_6O_{11} and PrO_2 forms in the flourite structure. Therefore, it was not unexpected to see some variation in the lattice parameters due to changes in the oxidation state.

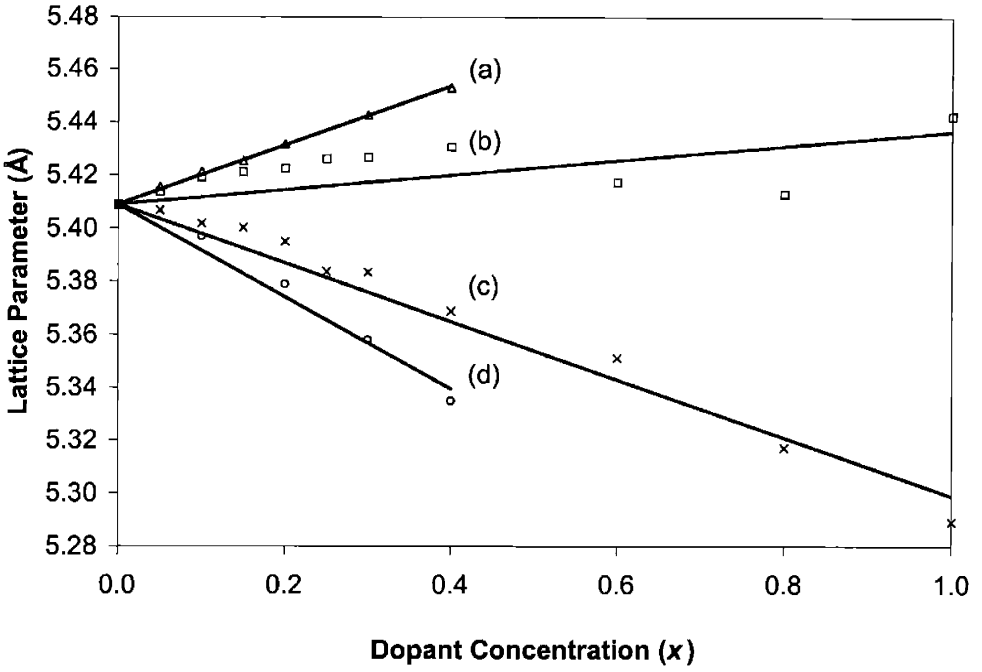

Figure 2.5 Effect of dopant concentration on the a_{200} lattice parameter of 600°C-calcined $Ce_{1-x}M_xO_{2-\delta}$ doped with (a) Sm, (b) Pr, (c) Tb and (d) Zr.

For $Ce_{1-x}M_xO_{2-\delta}$ doped with Sm, Tb, Pr and Zr, significant grain growth suppression was achieved at 1000°C compared to pure CeO_2 (Figures 2.6 through 2.9). In particular, $Ce_{1-x}Zr_xO_{2-\delta}$ demonstrated excellent stability against grain growth with increasing x after calcination at 600°C, 800°C and 1000°C. $Ce_{1-x}Zr_xO_{2-\delta}$ with $x > 0.2$ retained grain sizes of < 10 nm and < 20 nm even after calcination to 800°C and 1000°C, respectively. For $Ce_{1-x}Sm_xO_{2-\delta}$, $Ce_{1-x}Tb_xO_{2-\delta}$ and $Ce_{1-x}Pr_xO_{2-\delta}$, the finest grain sizes obtained at 1000°C were 47 nm at $x = 0.1$, 25 nm at $x = 1.0$ and 35 nm at $x = 0.4$, respectively.

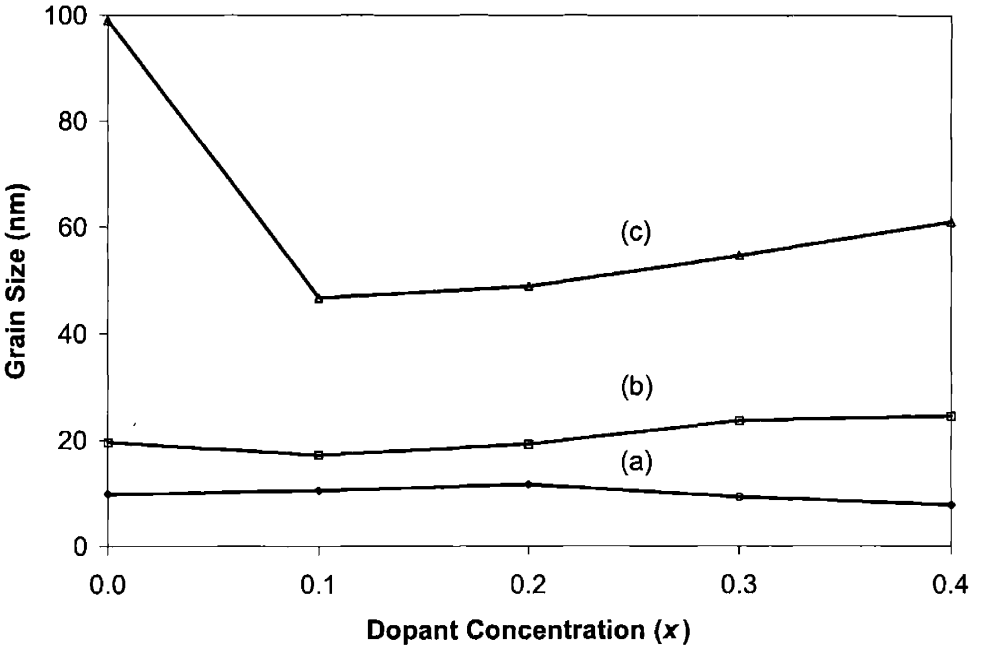

Figure 2.6 Effect of dopant concentration on the XRD grain size of $Ce_{1-x}Sm_xO_{2-\delta}$ calcined at (a) 600°C, (b) 800°C and 1000°C.

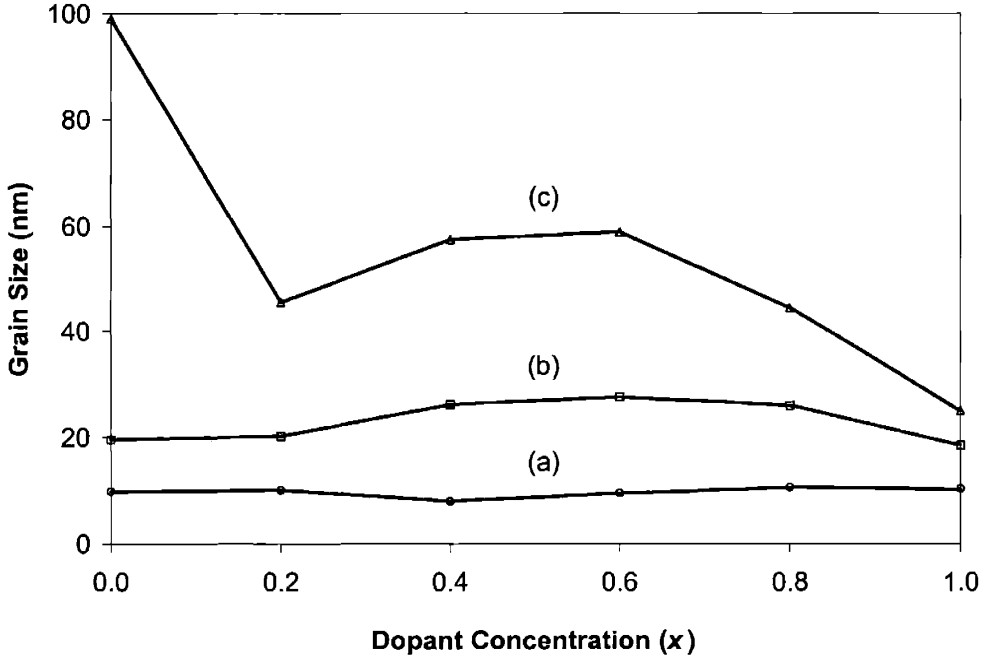

Figure 2.7 Effect of dopant concentration on the XRD grain size of $Ce_{1-x}Tb_xO_{2-\delta}$ calcined at (a) 600°C, (b) 800°C and (c) 1000°C.

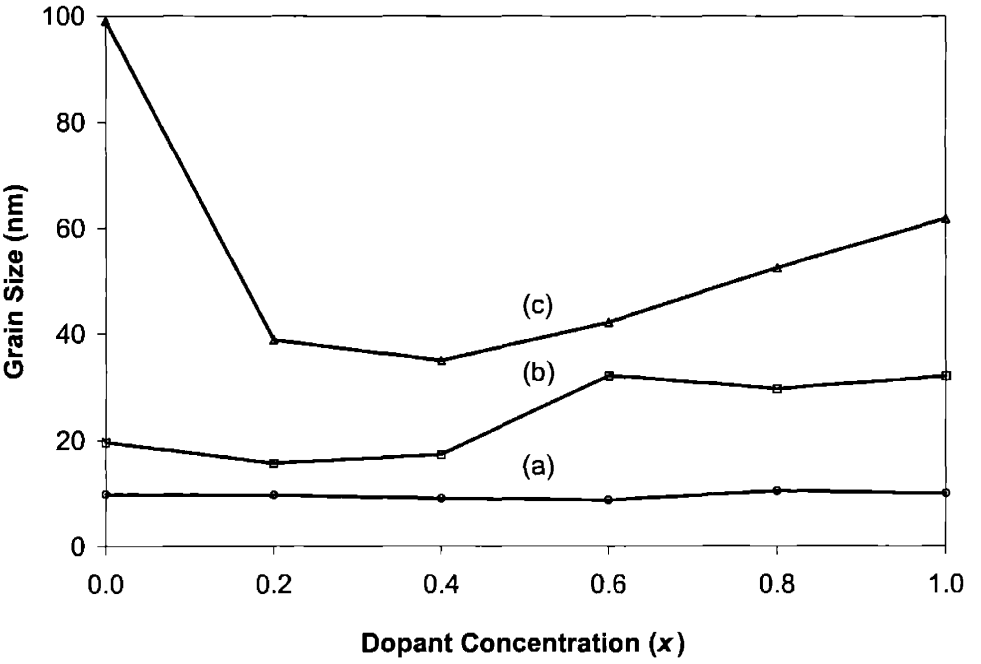

Figure 2.8 Effect of dopant concentration on the XRD grain size of $Ce_{1-x}Pr_xO_{2-\delta}$ calcined at (a) 600°C, (b) 800°C and (c) 1000°C.

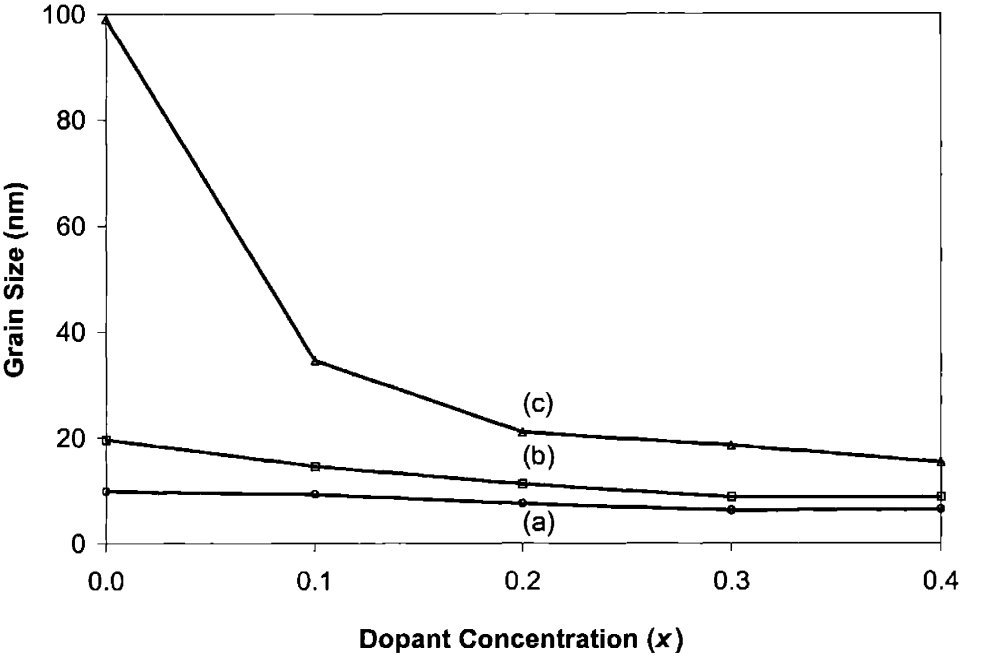

Figure 2.9 Effect of dopant concentration on the XRD grain size of $Ce_{1-x}Zr_xO_{2-\delta}$ calcined at (a) 600°C, (b) 800°C and (c) 1000°C.

The excellent thermal stability of $Ce_{0.6}Zr_{0.4}O_{2-\delta}$ could be attributed to the secondary ZrO_2 phase formation (see Figure 2.4(e)). HRTEM micrograph (Figure 2.10) illustrates 1000°C-calcined $Ce_{0.6}Zr_{0.4}O_{2-\delta}$ as agglomerated grains of < 20 nm with fine regions and coatings of ZrO_2, which might have served towards inhibiting grain growth by preventing contacts between adjacent $Ce_{1-x}Zr_xO_{2-\delta}$ crystallites.

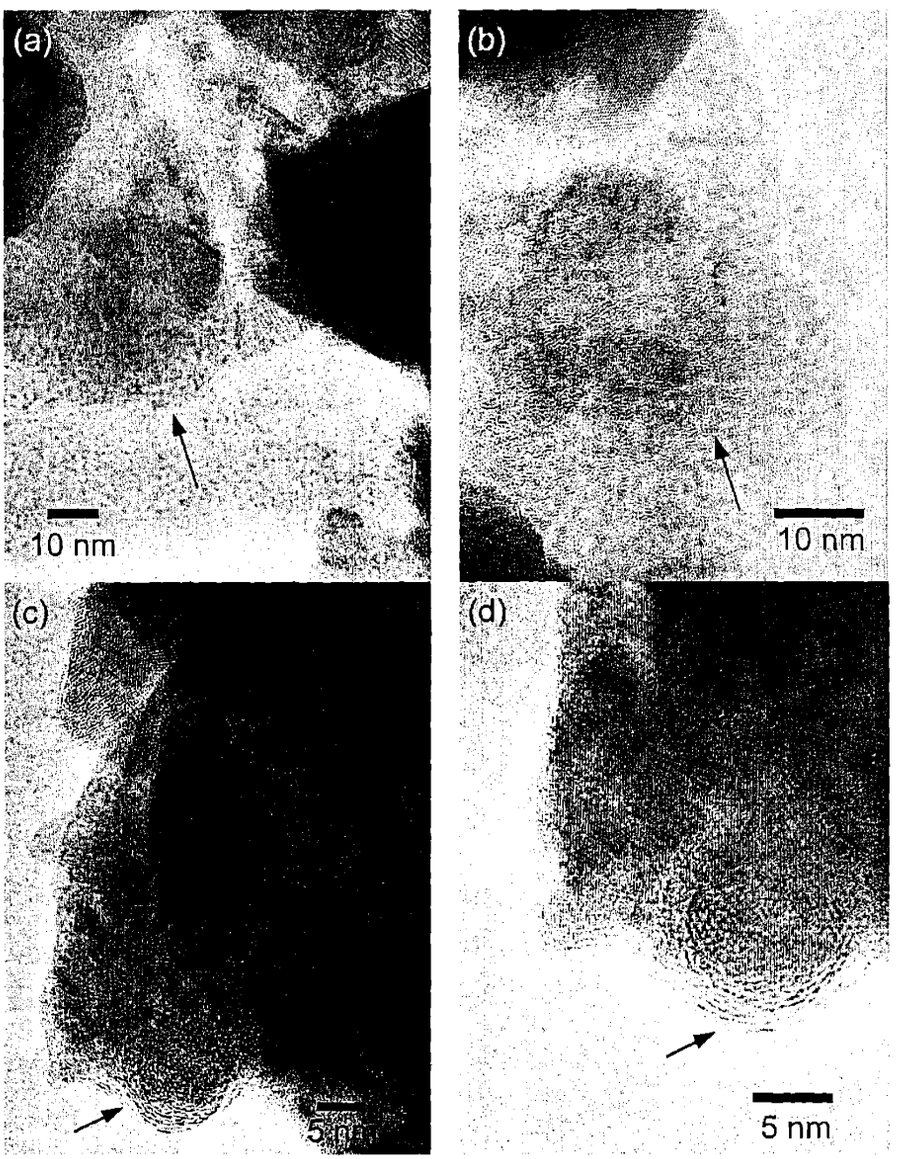

Figure 2.10 HRTEM micrograph of 1000°C-calcined $Ce_{0.6}Zr_{0.4}O_{2-\delta}$ showing (a) and (b) segregated amorphous ZrO_2, and (c) and (d) thin coatings of ZrO_2 around $Ce_{1-x}Zr_xO_{2-\delta}$ crystallites.

2.3.2 Temperature-Programmed Reduction of $Ce_xM_{1-x}O_{2-\delta}$

The purpose of introducing dopants into CeO_2 was to improve thermal stability as well as O_2 storage capacity. O_2 accessibility of $Ce_{1-x}M_xO_{2-\delta}$ materials was examined by analyzing weight change associated with O_2 evolution from the samples under a reducing atmosphere. H_2 was selected as the reducing gas to avoid effects of weight gain due to surface complex formation associated with gases such as CO and CH_4.

2.3.2.1 Reducibility of $Ce_{0.8}M_{0.2}O_{2-\delta}$ with Non-Lanthanide Dopants

The overall reducibility of $Ce_{0.8}M_{0.2}O_{2-\delta}$ with Ca, Zr and Sc dopants at 800°C in 2.5% H_2 was significantly higher than that of pure CeO_2 (Figure 2.11). For pure CeO_2, an initial H_2 uptake was seen between 150°C and 550°C, followed by a significant reduction above 550°C. The increase in reduction temperature from that seen in the literature (482°C) [1] could be attributed to the lower H_2 concentration used in this TPR study. $Ce_{0.8}Ca_{0.2}O_{2-\delta}$ also experienced an initial H_2 uptake, followed by an abrupt reduction between 350°C and 450°C equivalent to ~ 1% weight loss, with further reduction above 575°C. An overall weight loss of 1.7% (equivalent to 47% of the total available oxygen) was noted for $Ce_{0.8}Ca_{0.2}O_{2-\delta}$. Both $Ce_{0.8}Sc_{0.2}O_{2-\delta}$ and $Ce_{0.8}Zr_{0.2}O_{2-\delta}$ showed continuous reduction in the TPR studies, achieving 1.3% and 1.7% weight loss by 800°C, with significant reduction starting at 500°C and 350°C, respectively. Although $Ce_{0.8}Y_{0.2}O_{2-\delta}$ provided only a minor overall improvement in reducibility at 800°C, its low-temperature oxygen availability was noticeably higher than pure CeO_2 with significant reduction beginning at 500°C.

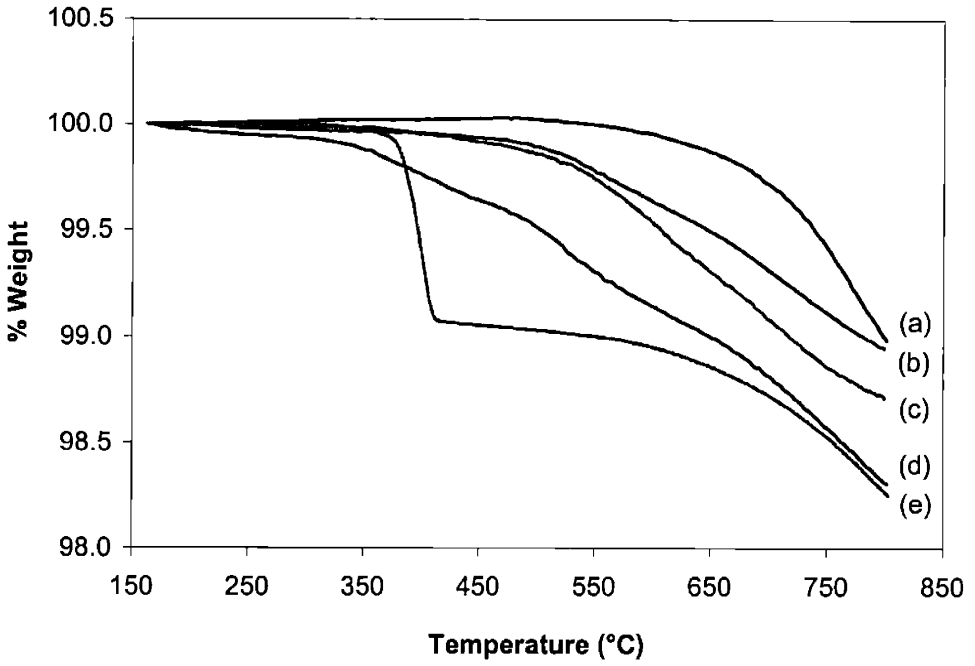

Figure 2.11 TPR analysis of (a) CeO_2 and $Ce_{0.8}M_{0.2}O_{2-\delta}$ doped with (b) Y, (c) Sc, (d) Zr and (e) Ca. The 800°C-calcined materials were first pretreated *in situ* at 800°C in O_2, followed by TPR at 150-800°C under 2.5% H_2 in He.

2.3.2.2 Reducibility of $Ce_{0.8}M_{0.2}O_{2-\delta}$ with Lanthanide Dopants

Reducibility of $Ce_{0.8}M_{0.2}O_{2-\delta}$ increased in the order: Ce < Sm < Tb < Pr, achieving 1.0, 1.1, 1.3 and 1.8 wt% reduction by 800°C (Figure 2.12). The lanthanide-doped materials were reducible at lower temperatures than pure CeO_2; reduction of $Ce_{0.8}Sm_{0.2}O_{2-\delta}$, $Ce_{0.2}Tb_{0.8}O_{2-\delta}$ and $Ce_{0.8}Pr_{0.2}O_{2-\delta}$ began below 500°C, 300°C and 275°C, respectively. Unlike CeO_2 and $Ce_{0.8}Sm_{0.2}O_{2-\delta}$, $Ce_{0.2}Pr_{0.8}O_{2-\delta}$ and $Ce_{0.2}Tb_{0.8}O_{2-\delta}$ experienced multiple reduction stages associated with the reduction of not only Ce^{+4}, but also the lanthanide cations. The absence of a secondary reduction stage for $Ce_{0.2}Sm_{0.8}O_{2-\delta}$ suggested that Sm^{+3} did not undergo reduction to Sm^{+2} in the temperature range investigated. Of the lanthanide-doped materials, $Ce_{0.8}Pr_{0.2}O_{2-\delta}$ experienced the greatest weight loss over the temperature range examined. Relative to $Ce_{0.8}M_{0.2}O_{2-\delta}$ with non-lanthanide dopants, $Ce_{0.8}Pr_{0.2}O_{2-\delta}$ achieved significant reducibility at 250-380°C and above 520°C, whereas $Ce_{0.2}Ca_{0.2}O_{2-\delta}$ had a higher reducibility between 380°C and 520°C. $Ce_{0.8}Pr_{0.2}O_{2-\delta}$ achieved a slightly higher overall reduction relative to $Ce_{0.8}Ca_{0.2}O_{2-\delta}$ by 800°C.

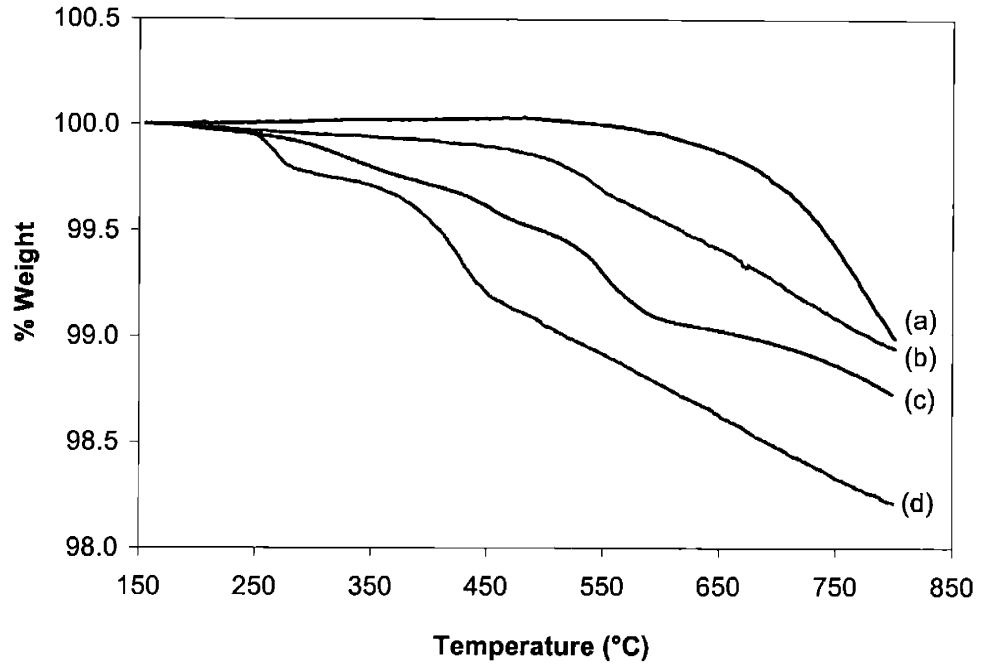

Figure 2.12 TPR analysis of (a) CeO_2 and $Ce_{0.8}M_{0.2}O_{2-\delta}$ doped with (b) Sm, (c) Tb and (d) Pr. The 800°C-calcined materials were first pretreated *in situ* at 800°C in O_2, followed by TPR at 150-800°C under 2.5% H_2 in He.

2.3.2.3 Reducibility of $Ce_{1-x}M_xO_{2-\delta}$ with Zr, Pr and Tb Dopants

Figure 2.13 shows that reducibility of $Ce_{1-x}Zr_xO_{2-\delta}$ increased with x. However, the overall reducibility for $Ce_{1-x}Zr_xO_{2-\delta}$ was similar for $x = 0.3$ and 0.4 at 800°C, suggesting that excess Zr dopants were not contributing significantly to the oxygen availability of $Ce_{1-x}Zr_xO_{2-\delta}$ since they were not fully substituted into the CeO_2 lattice. For all $Ce_{1-x}Zr_xO_{2-\delta}$ materials, reduction began below 400°C, with some reducibility below 250°C for $x \geq 0.2$ suggesting low-temperature oxygen release.

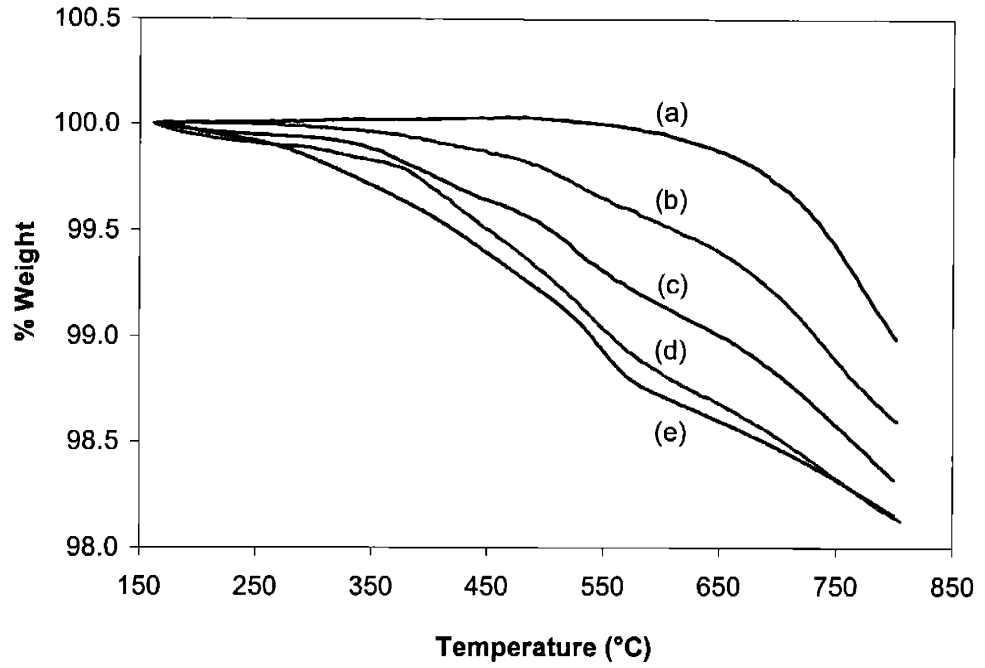

Figure 2.13 TPR analysis of $Ce_{1-x}Zr_xO_{2-\delta}$ with x = (a) 0.0, (b) 0.1, (c) 0.2, (d) 0.3 and (e) 0.4. The 800°C-calcined materials were first pretreated *in situ* at 800°C in O_2, followed by TPR at 150-800°C under 2.5% H_2 in He.

Both $Ce_{1-x}Tb_xO_{2-\delta}$ and $Ce_{1-x}Pr_xO_{2-\delta}$ showed increased overall reducibility at 800°C with increasing x (Figures 2.14 and 2.15). $Ce_{1-x}Pr_xO_{2-\delta}$ achieved greater reducibility than $Ce_{1-x}Tb_xO_{2-\delta}$ at all dopant levels. PrO_2 underwent an initial weight loss of 1.5% to Pr_6O_{11} by 360°C, and was converted to Pr_2O_3 by 800°C with a total weight loss of 4.8%. Of the $Ce_{1-x}Pr_xO_{2-\delta}$ materials, the lowest initial reduction temperature of 260°C was achieved at $x = 0.2$. However, the initial reduction was more significant (1.5 wt%) for $x \geq 0.6$. For the $Ce_{1-x}Tb_xO_{2-\delta}$ series, superior reducibility was achieved below 600°C compared to CeO_2. In particular, $TbO_{2-\delta}$ gave rise to 3% weight loss by 600°C, with limited reduction above that temperature. Assuming that its final reduced state was pure Tb_2O_3, the starting material was calculated to be $TbO_{1.8}$. This is not unexpected since Tb is less stable than Pr in the +4 oxidation state [15].

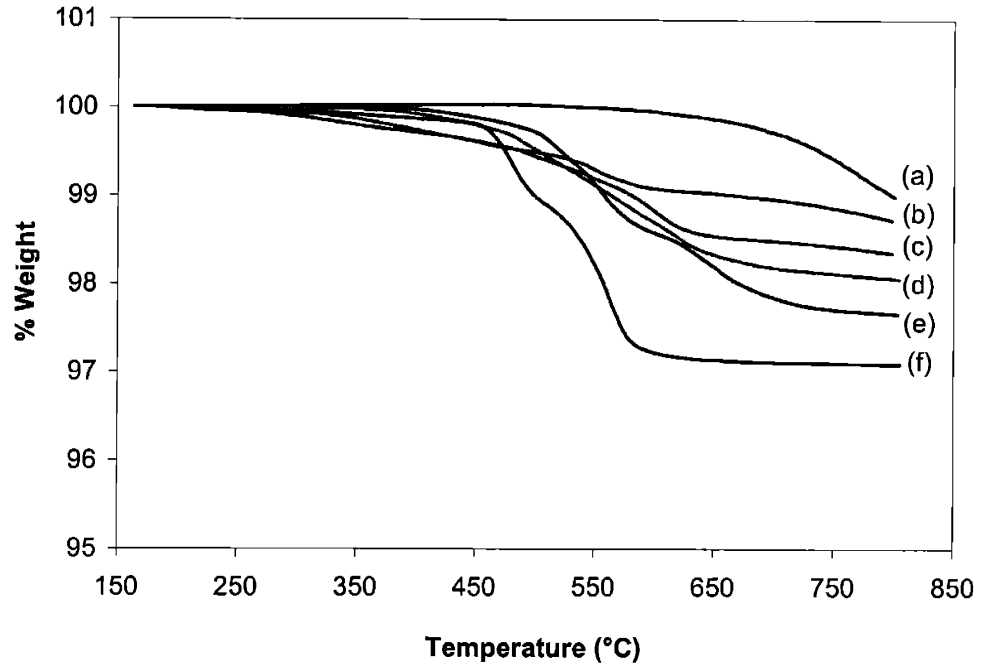

Figure 2.14 TPR analysis of $Ce_{1-x}Tb_xO_{2-\delta}$ with x = (a) 0.0, (b) 0.2, (c) 0.4, (d) 0.6, (e) 0.8 and (f) 1.0. The 800°C-calcined materials were first pretreated *in situ* at 800°C in O_2, followed by TPR at 150-800°C under 2.5% H_2 in He.

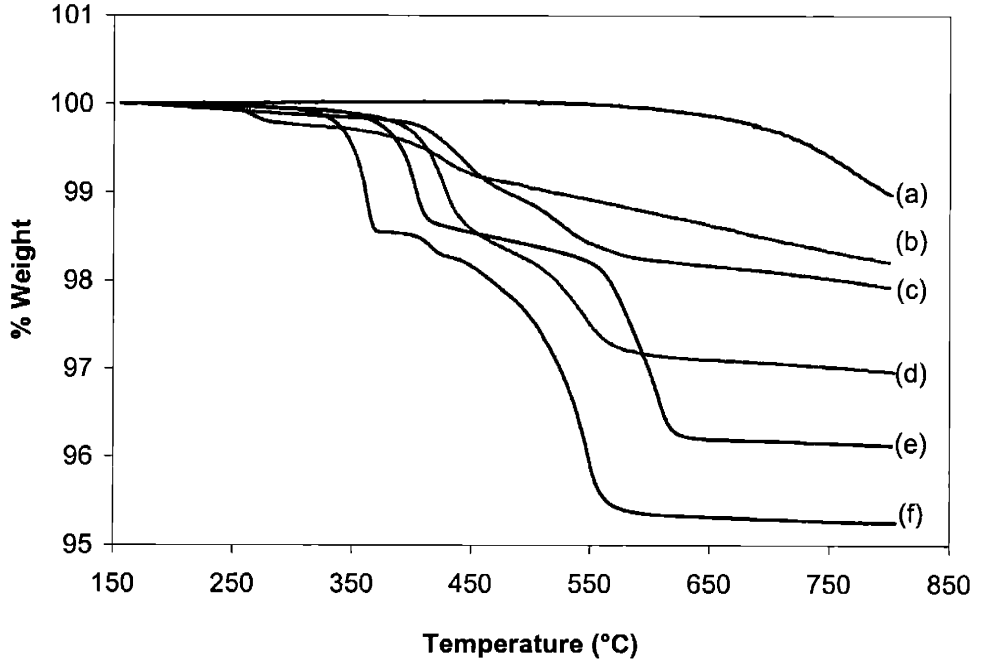

Figure 2.15 TPR analysis of $Ce_{1-x}Pr_xO_{2-\delta}$ with x = (a) 0.0, (b) 0.2, (c) 0.4, (d) 0.6, (e) 0.8 and (f) 1.0. The 800°C-calcined materials were first pretreated *in situ* at 800°C in O_2, followed by TPR at 150-800°C under 2.5% H_2 in He.

2.3.3 Catalytic CO Oxidation Studies

To develop an understanding of the effect of dopants on CO oxidation over $Ce_{1-x}M_xO_{2-\delta}$, the catalytic activity of these nanocomposites was examined as a function of temperature. A feedstream composition of 1% CO and 0.75% O_2 in He was used so that gas-phase O_2 availability would not affect the catalytic CO conversion over the materials. The samples were first pretreated at 500°C in 0.75% O_2 in He. CO conversion was then monitored by measuring both CO and CO_2 in the exhaust stream as the temperature was decreased in 25°C increments. The CO light-off temperature corresponding to 10% CO conversion was obtained for the various materials to compare their CO oxidation activity.

2.3.3.1 CO Conversion over $Ce_{0.8}M_{0.2}O_{2-\delta}$

In the absence of Pd, none of the non-lanthanide doped $Ce_{0.8}M_{0.2}O_{2-\delta}$ materials attained significant CO oxidation activity below 300°C (Figure 2.16). Only $Ce_{0.8}Sc_{0.2}O_{2-\delta}$ and $Ce_{0.8}Zr_{0.2}O_{2-\delta}$ achieved a lower light-off temperature (247°C and 264°C, respectively) than CeO_2 (285°C). $Ce_{0.8}Sc_{0.2}O_{2-\delta}$ and CeO_2 attained nearly full conversion by 400°C and 425°C, respectively. With the exception of $Ce_{0.8}Pr_{0.2}O_{2-\delta}$, the lanthanide doped $Ce_{0.8}M_{0.2}O_{2-\delta}$ materials showed a lower CO oxidation activity than CeO_2 (Figure 2.17). $Ce_{0.8}Tb_{0.2}O_{2-\delta}$ and $Ce_{0.8}Sm_{0.2}O_{2-\delta}$ achieved light-off at 299°C and 295°C, respectively. $Ce_{0.8}Pr_{0.2}O_{2-\delta}$ attained light-off at 274°C, with full conversion by 425°C. It was not as active for CO oxidation as $Ce_{0.8}Sc_{0.2}O_{2-\delta}$ and $Ce_{0.8}Zr_{0.2}O_{2-\delta}$.

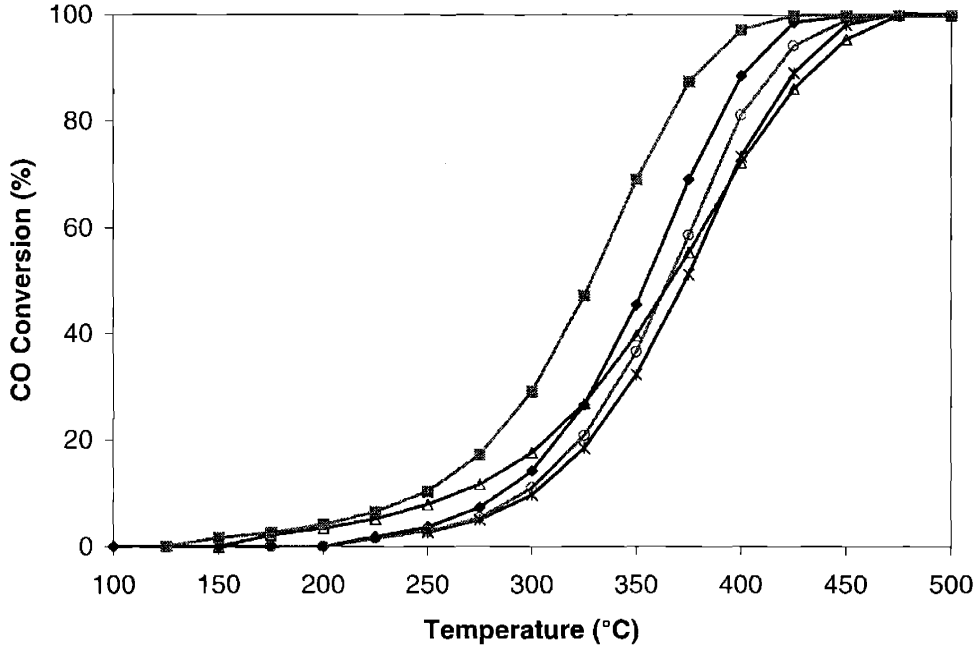

Figure 2.16 CO conversion over 600°C-calcined (■) $Ce_{0.8}Sc_{0.2}O_{2-\delta}$, (Δ) $Ce_{0.8}Zr_{0.2}O_{2-\delta}$, (♦) CeO_2, (○) $Ce_{0.8}Ca_{0.2}O_{2-\delta}$ and (*) $Ce_{0.2}Y_{0.8}O_{2-\delta}$. The reaction was conducted with 1% CO and 0.75% O_2 in He at 120,000 hr^{-1}.

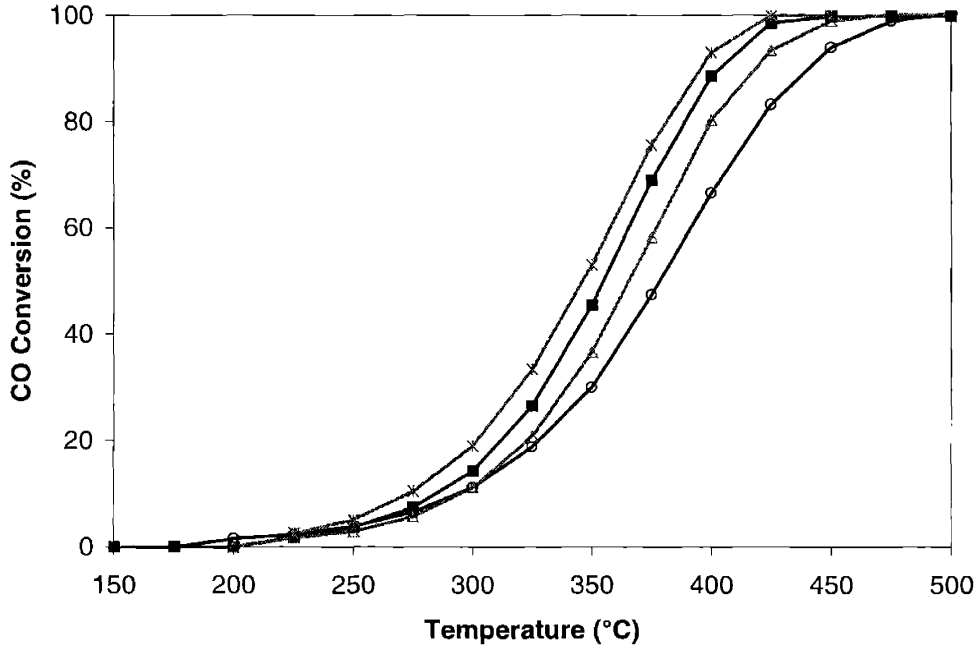

Figure 2.17 CO conversion over 600°C-calcined (*) $Ce_{0.8}Pr_{0.2}O_{2-\delta}$, (■) CeO_2, (Δ) $Ce_{0.8}Tb_{0.2}O_{2-\delta}$ and (○) $Ce_{0.2}Sm_{0.8}O_{2-\delta}$. The reaction was conducted with 1% CO and 0.75% O_2 in He at 120,000 hr^{-1}.

2.3.3.2 CO Conversion over $Ce_{1-x}Zr_xO_{2-\delta}$ and $Ce_{1-x}Pr_xO_{2-\delta}$

$Ce_{0.9}Zr_{0.1}O_{2-\delta}$ and $Ce_{0.8}Zr_{0.2}O_{2-\delta}$ achieved significantly lower light-off temperatures for CO oxidation (252°C and 264°C, respectively) compared to CeO_2 (285°C) (Figure 2.18). However, they did not obtain full CO conversion until 475°C while CeO_2 provide for full conversion at 450°C. Further increasing the Zr content to x = 0.3 and 0.4 decreased the light-off temperature slightly to 278°C and 283°C, respectively, with full conversion at ~ 500°C.

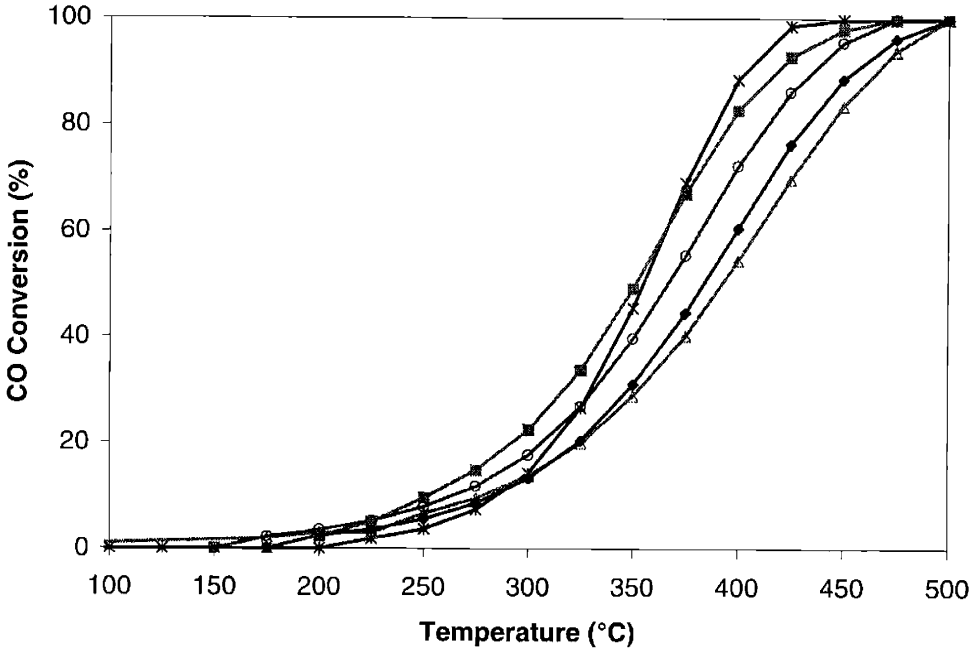

Figure 2.18 CO conversion over 600°C-calcined (■) $Ce_{0.9}Zr_{0.1}O_{2-\delta}$, (○) $Ce_{0.8}Zr_{0.2}O_{2-\delta}$, (*) CeO_2, (♦) $Ce_{0.7}Zr_{0.3}O_{2-\delta}$ and (Δ) $Ce_{0.6}Zr_{0.4}O_{2-\delta}$. The reaction was conducted with 1% CO and 0.75% O_2 in He at 120,000 hr^{-1}.

CO light-off was attained at 274°C and 264°C, respectively, by $Ce_{0.8}Pr_{0.2}O_{2-\delta}$ and $Ce_{0.6}Pr_{0.4}O_{2-\delta}$ (Figure 2.19). Full conversion was achieved by 425°C over these materials. $Ce_{0.4}Pr_{0.6}O_{2-\delta}$ showed little improvement over pure CeO_2, with light-off and full conversion temperatures of 283°C and 450°C, respectively. $Ce_{0.2}Pr_{0.8}O_{2-\delta}$ and $PrO_{2-\delta}$ showed significantly lower CO oxidation activity, with light-off at 309°C and 327°C, respectively, and full conversion by 475°C.

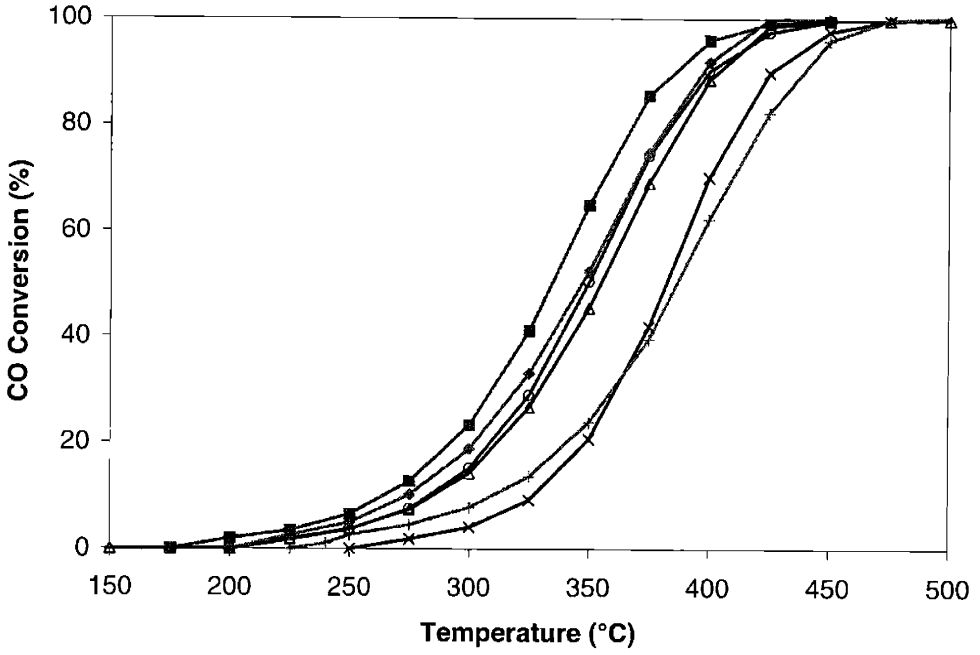

Figure 2.19 CO conversion over 600°C-calcined (■) $Ce_{0.6}Pr_{0.4}O_{2-\delta}$, (♦) $Ce_{0.8}Pr_{0.2}O_{2-\delta}$, (○) $Ce_{0.4}Pr_{0.6}O_{2-\delta}$, (Δ) CeO_2, (+) $Ce_{0.2}Pr_{0.8}O_{2-\delta}$ and (×) $PrO_{2-\delta}$. The reaction was conducted with 1% CO and 0.75% O_2 in He at 120,000 hr^{-1}.

2.4 Summary

Oxygen storage materials with low-temperature activity are necessary for automotive emission reduction in the current internal combustion engines and modified lean-burn engines. In an effort to improve upon the existing technology, CeO_2 was modified with various dopants and analyzed for structural stability, reducibility and catalytic CO oxidation activity. For $Ce_{0.8}M_{0.2}O_{2-\delta}$, Pr doping led to a higher surface area of 95 m^2/g compared to Zr doping (82 m^2/g) at 600°C. However, at 1000°C, $Ce_{0.8}Zr_{0.2}O_{2-\delta}$ retained the finest nanostructure with a grain size of < 30 nm. The effect of doping level on thermal stability was determined for $Ce_{1-x}Tb_xO_{2-\delta}$ and $Ce_{1-x}Pr_xO_{2-\delta}$ for $x \leq 1.0$, as well as for $Ce_{1-x}Sm_xO_{2-\delta}$ and $Ce_{1-x}Zr_xO_{2-\delta}$ for $x \leq 0.4$. $Ce_{1-x}Pr_xO_{2-\delta}$ materials with $x \leq 0.4$ were shown to possess superior surface areas compared to other compositions. In particular, $Ce_{0.9}Pr_{0.1}O_{2-\delta}$ showed the highest surface area (60 m^2/g) at 800°C. $Ce_{1-x}Zr_xO_{2-\delta}$ attained the highest grain size stability at 1000°C with grain sizes of < 20 nm for $x = 0.3$ and 0.4. For this series, the materials benefited not only from dopant stabilization, but

also from a segregated amorphous ZrO_2 phase, which acted as a diffusion barrier against grain growth.

Reducibility of the CeO_2-based nanocomposites was investigated between 150°C and 800°C to understand the effect of dopant selection and concentration on oxygen availability. All nanocomposites showed superior reducibility compared to pure CeO_2, which experienced an initial H_2 uptake, followed by significant reduction above 550°C. Both $Ce_{0.8}Ca_{0.2}O_{2-\delta}$ and $Ce_{0.8}Pr_{0.2}O_{2-\delta}$ attained significant reducibility below 450°C, with nearly 1% weight loss. $Ce_{1-x}Zr_xO_{2-\delta}$ showed increased reduction with increasing Zr content up to $x = 0.3$. Reduction for both $Ce_{1-x}Pr_xO_{2-\delta}$ and $Ce_{1-x}Tb_xO_{2-\delta}$ increased significantly with increasing x. Pure $PrO_{2-\delta}$ showed the greatest weight loss, corresponding to an overall reduction of PrO_2 to Pr_2O_3 by 800°C; it gave rise to a low-temperature reduction of 1.5 wt% at 350°C consistent with a transition from PrO_2 to Pr_6O_{11}.

Catalytic CO oxidation studies showed Sc-, Zr- and Pr-doped $Ce_{0.8}M_{0.2}O_{2-\delta}$ to have lower light-off temperatures of 247°C, 264°C and 274°C, respectively, compared to CeO_2 (285°C). For $Ce_{1-x}Zr_xO_{2-\delta}$, the lowest light-off temperature of 252°C was attained by $Ce_{0.9}Zr_{0.1}O_{2-\delta}$. $Ce_{1-x}Pr_xO_{2-\delta}$ with $x \leq 0.6$ achieved lower CO light-off temperatures than CeO_2, with x = 0.4 attaining light-off at the lowest temperature of 264°C.

2.5 References

[1] Zhang, Y., Andersson, S., Muhammed, M., *Appl. Catal. B: Environ.* **1995**, *6*, 325.
[2] Delmon, B., Yates, J. T., *Stud. Surf. Sci. Catal.* **1998**, *115*, 1.
[3] Feeley, J., Deeba, M., Farrauto, R. J., *Stud. Surf. Sci. Catal.* **1998**, *116*, 529.
[4] Logan, A. D., Shelef, M., *J. Mater. Res.* **1994**, *9*, 468.
[5] Palmqvist, A. E. C., Wirde, M., Gelius, U., Muhammed, M., *Nanostruct. Mater.* **1999**, *11*, 995.
[6] Shuk, P., Greenblatt, M., Croft, M., *Chem. Mater.* **1999**, *11*, 473.
[7] Gonzalez-Velasco, J. R., Gutierrez-Ortiz, M. A., Marc, J. L., Botas, J. A., Gonzalez-Marcos, M. P., Blanchard, G., *Appl. Catal. B: Environ.* **1999**, *22*, 167.
[8] Balducci, G., Kaspar, J., Fornasiero, P., Graziani, M., Islam, M. S., *J. Phys. Chem. B* **1998**, *102*, 557.
[9] Masui, T., Ozaki, T., Machida, K., Adachi, G., *J. Alloy. Comp.* **2000**, *303*, 49.
[10] Masui, T., Nakano, K., Ozaki, T., Adachi, G., Kang, Z., Eyring, L., *Chem. Mater.* **2001**, *13*, 1834.
[11] Madier, Y., Descorme, C., Le Govic, A. M., Duprez, D., *J. Phys. Chem. B* **1999**, *103*, 10999.
[12] Rossignol, S., Micheaud-Especel, C., Duprez, D., *Stud. Surf. Sci. Catal.* **2000**, *130*, 3327.
[13] Ozawa, M., Kimura, M., Isogai, A., *J. Alloy. Comp.* **1993**, *193*, 73.
[14] Lide, D. R., *CRC Handbook of Chemistry and Physics*, 72 ed., CRC Press, Boston, **1991**.
[15] Kang, Z. C., Eyring, L., in *Key Engineering Materials*, Vol. 155-156 (Ed.: Boulesteix, C.), Trans Tech Publications Ltd., Zuerich, **1998**, pp. 301.
[16] Kimura, S., Arai, F., Ikezawa, M., *J. Electron Spectrosc. Relat. Phenom.* **1996**, *78*, 135.
[17] Jen, H. W., Graham, G. W., Chun, W., McCabe, R. W., Cuif, J. P., Deutsch, S. E., Touret, O., *Catal. Today* **1999**, *50*, 309.
[18] Shigapov, A. N., Jen, H.-W., Graham, G. W., Chun, W., McCabe, R. W., *Stud. Surf. Sci. Catal.* **2000**, *130*, 1373.
[19] Su, E. C., Rothschild, W. G., *J. Catal.* **1986**, *99*, 506.
[20] Barin, I., *Thermochemical Data of Pure Substances*, VCH, New York, **1993**.

3 – Metal Oxide Nanocomposites for Low-Temperature SO_2 Adsorption

3.1 Introduction

New automotive emissions regulations call for a 40% reduction in CO and hydrocarbon emissions and a 30% reduction in NO_x emission by 2004. To conform to these regulations, researchers have explored the idea of a lean-burn engine [1]. CO is eliminated and NO_x formation is reduced by 87% by operating under the lean-burn condition (i.e. at an air to fuel ratio > 20) [2], whereby the excess oxygen present inhibits further NO_x removal. To address this problem, NO_x storage systems have been developed to adsorb NO_x with the intent of using the periodic fuel-rich pulses to remove and reduce the NO_x to nitrogen [1, 3-5]. However, SO_2 is competitively adsorbed on the NO_x storage system, and its presence, particular in diesel fuel, makes implementation of this process difficult [3, 6, 7]. Thus it is critical to treat the SO_2 upstream of the NO_x storage material to prevent poisoning of the latter.

Current SO_2 removal technology falls into two categories: (1) high-temperature SO_x transfer in fluidized catalytic cracking, and (2) low-temperature SO_2 scrubbing in flue gas application. Increased attention has been devoted to magnesium aluminates for high-temperature applications, especially with substitution of secondary ions such as iron to modify their regeneration temperature [8-11]. In contrast, low-temperature processes have utilized a low-cost calcium hydroxide-based system in a powder or slurry form [2]. For automotive applications where the sorbent weight is important, regenerability and removal efficiency are critical in the material selection. Recent research has explored CuO/Al_2O_3 for its high SO_2 adsorption capacity and regenerability at moderate temperatures (< 450°C) in H_2, CO or CH_4 atmosphere [12, 13]. However, the limited reduction potential of the exhaust gases under the lean-burn conditions and the low operating temperatures of the NO_x storage system present significant challenges in SO_2 adsorption capacity and regeneration efficiency [3, 4].

Our research is focused on the development of CuO-based mixed metal oxides to improve the low-temperature regenerability of SO_2 adsorbents. The ideal material would provide for high adsorption capacity as well as efficient regeneration $\leq$ 400°C. By manipulating the structure and composition of SO_2 adsorbent materials, the interaction

between SO_2 and the metal oxide surfaces might be varied to facilitate adsorption and regeneration at low temperatures.

3.2 Experimental

3.2.1 Materials Synthesis

Simple and mixed metal oxides were synthesized by chemical precipitation of metal nitrates (Alfa Aesar) with tetraethyl ammonium hydroxide (Alfa Aesar, 40 wt% in water). Typical precipitation involved dropwise addition of the metal nitrate solution (0.1 M) into the base solution (0.1 M) under vigorous stirring to achieve a final pH of 10. The precipitate was allowed to age for 18 hours before recovery by centrifuging at 3000 rpm for over 10 min. The supernatant was decanted, and the recovered powders were washed three times with isopropanol. The materials were then dried at 25°C, ground by mortal and pestle to break up loss agglomerates prior to calcination at 500°C (ramp = 2°C/min).

3.2.2 Materials Characterization

The surface area of the powders was determined from nitrogen adsorption analysis by the five-point BET (Brunauer-Emmett-Teller) method with a Micromeritics ASAP 2000 gas adsorption analyzer. Phase identification was performed by powder X-ray diffraction (XRD) using a Siemens D5000 θ-θ diffractometer (45 kV, 40 mA, Cu-K_α). Grain size of $CuCr_2O_4$ was obtained by peak broadening analysis of the <211> reflection (2θ = 35.159) using the Scherrer method and correcting for instrumental line broadening. The *a* and *c* lattice parameters of $CuCr_2O_4$ were calculated from the <211> and <200> peak positions and corrected for instrumental error using the <111> peak of a Si reference.

3.2.3 SO_2 Adsorption and Regeneration

A vertical tubular flow reactor was used to perform adsorption and regeneration studies (Figure 3.1). The sample was supported on a bed of quartz wool in a ¼"-OD quartz reactor tube. An Omega K-type thermocouple protected by a quartz sheath was used in conjunction with a vertically mounted Lindberg Blue-M tube furnace and an Omega temperature controller to maintain the reaction temperature (200-700°C) within 2°C. MKS mass flow controllers were used to control the feedstream composition and

maintain the flow rate at a constant space velocity of ~ 240,000 hr^{-1}. The effluent stream was analyzed by a Hewlett-Packard 6890 gas chromatograph equipped with a thermal conductivity detector, a Chromosil 310 column to separate and quantify CO, CO_2 and SO_2, and a 5-ml sample loop. Following SO_2 adsorption at 400°C in a stream of 130 ppm SO_2 and 1% O_2 in He, a temperature-programmed desorption (TPD) study was performed by reducing the temperature first to 200°C and then introducing 2000 ppm CO in He for experiments at 500-700°C (ramp = 1°C/min). By monitoring the effluent gas concentration, the quantity of SO_2 desorbed by a specific temperature was determined. Prior to analysis, each sample was compacted at 175 lb/in^2, crushed and sieved to 60 mesh to ensure consistent interparticle diffusion and minimal pressure drop.

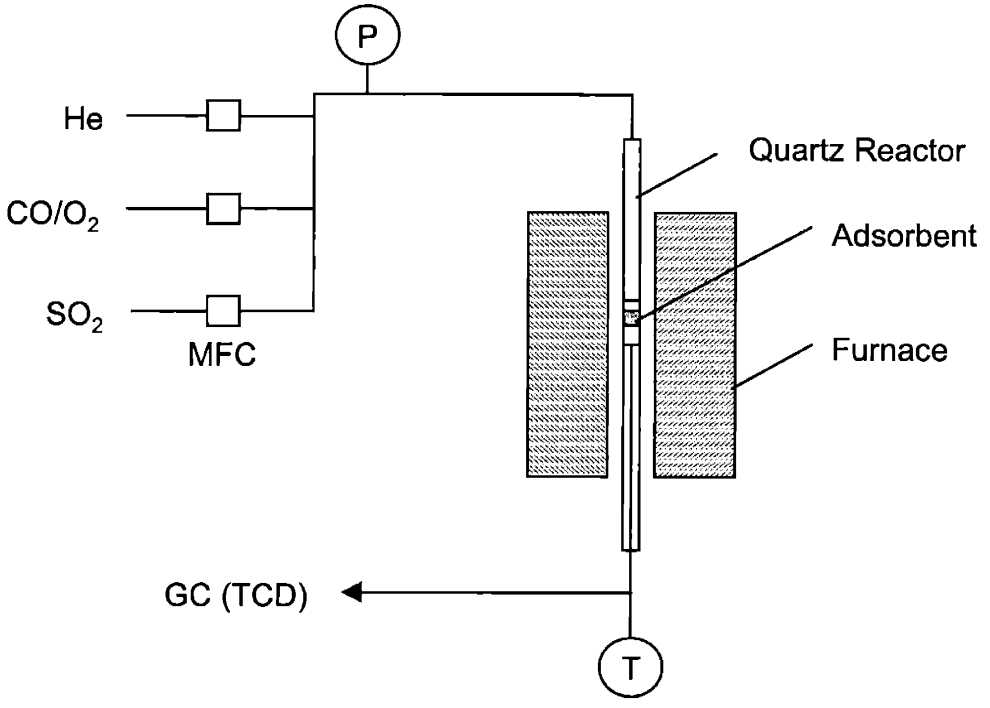

Figure 3.1 SO_2 adsorption reactor setup.

SO_2 adsorption was examined as a function of time using a Perkin Elmer System 7HT Thermal Gravimetric Analyzer (TGA). Samples were first pretreated at 400°C in 1% O_2 in He for 30 min, before the introduction of 130 ppm SO_2 in He. The feedstream flow rate was maintained at 400 sccm, and a sample weight of < 5 mg was used to minimize the effects of diffusion.

A vertical tubular flow reactor was used to perform pulse SO_2 adsorption analysis (Figure 2.1). The sample was supported on a bed of quartz wool in a ¼"-OD quartz reactor tube. An Omega K-type thermocouple protected by a quartz sheath was used in conjunction with a vertically mounted Lindberg tube furnace and an Omega temperature controller to maintain the reaction temperature (400°C) within 2°C. Sierra and MKS mass flow controllers were used to control the feedstream composition and maintain the flow rate at a constant space velocity of ~ 120,000 hr^{-1}. A continuous feed of 300 ppm SO_2 in He was introduced. To control the feedstream composition, Lab View was used in conjunction with solenoid valves for CO and O_2, as well as a 6-port gas chromatograph (GC) sampling valve to switch between He and either CO or O_2. A 1-min He flush was used in between pulses to remove residual O_2 or CO from the reactor. A quartz blank was placed at the top of the reactor tube, and the inlet and outlet tubing was adjusted to minimize dead volume. The effluent stream was analyzed by a VG Gas Lab 300 mass spectrometer operating with a ThO_2 filament and a secondary electron multiplier (1000 V). Masses of 40 and 64 were monitored with a constant feed of 3000 ppm Ar in He as a reference. Typical sampling time was < 3 sec to ensure multiple sampling over the 10-min pulse. Prior to analysis, each material was pressed at 175 lb/in^2, crushed and sieved to 60 mesh to ensure consistent interparticle diffusion and minimal pressure drop. The catalyst weight was varied from 50 mg to 120 mg to maintain a constant bed height of 4 mm.

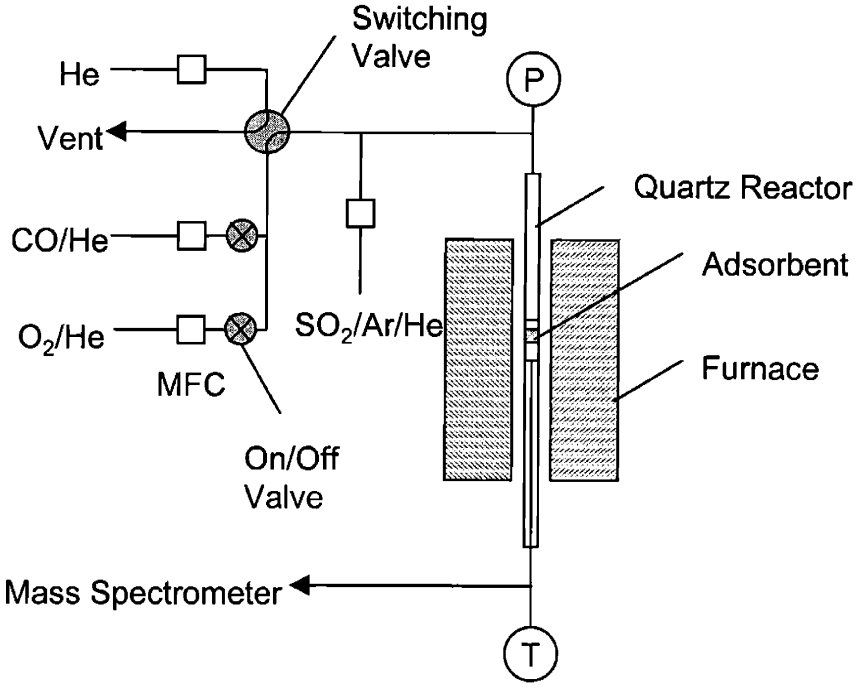

Figure 3.2 Schematic of pulsing reactor setup.

3.3 Results and Discussion

3.3.1 SO_2 Sorption Characteristics of Mixed Oxides

The ideal metal oxide adsorbent should form a stable sulfate at 400°C to promote SO_2 adsorption, and form a sulfite that would decompose < 400°C to allow for reduction and decomposition during the fuel-rich pulses. The challenge lies in the fact that most metal sulfates are stable above 600°C. Lowell *et al.* have performed a comprehensive study on the interaction of SO_2 with metal oxides. No simple metal oxide possesses a high adsorption capacity with efficient regenerability below 400°C [14]. Thus, a mixed metal oxide needs to be developed with these desired properties. By combining CuO with other first row transition metal oxides, which have the lowest sulfate decomposition temperatures, low temperature regenerability may be achieved.

3.3.1.1 Synthesis and Characteristics of CuO-based Mixed Oxides

Selected CuO-based mixed metal oxides were synthesized through chemical co-precipitation as 50 wt%-50 wt% mixture, and examined for SO_2 adsorption capacity, low-temperature desorption and regenerability (Table 3.1). SO_2 was first adsorbed onto the

mixed oxides at 400°C for a period of ≥ 30 min in a stream of 130 ppm SO_2 and 1% O_2 in He at 120,000 hr^{-1}, followed by a TPD study between 200°C and 700°C in a stream of 2000 ppm CO in He at 120,000 hr^{-1}. Mixing of CuO and MnO_2 produced a pure $Cu_{1.5}Mn_{1.5}O_4$ phase having the highest adsorption capacity with respect to weight (118.6 mg SO_2/g). However, the presence of MnO_2 resulted in a high peak SO_2 desorption temperature of 630°C (Figure 3.3). All the mixed oxides achieved > 60% SO_2 desorption by 700°C, with the Co_2O_3-CuO mixture desorbing the largest amount of SO_2 (6.48 mg/m^2). However, as with MnO_2-CuO, the peak SO_2 desorption temperature for Co_2O_3-CuO was well above 400°C. In_2O_3 and Fe_2O_3, which would release SO_2 below 400°C in the pure oxide form, did not provide for SO_2 desorption below 400°C when mixed with CuO. It was interesting to find, however, that Cr_2O_3-CuO gave a peak desorption at a remarkably low-temperature of 340°C, which was below that for pure Cr_2O_3 (580°C) and pure CuO (460°C). This mixed oxide completed its desorption by 400°C.

Table 3.1 Characteristics of 500°C-calcined 50 wt% MO_x-50 wt% CuO mixed oxides. SO_2 adsorption was established for each material when breakthrough was attained in a feed of 130 ppm SO_2 and 1% O_2 in He at GHSV ~ 120,000 hr^{-1} and 400°C. Desorption was achieved by introducing 1% O_2 in He at 200°C, and then 2000 ppm CO in He at GHSV ~ 120,000 hr^{-1} and 200-700°C (ramp = 1°C/min).

MO_x	Mixed Phase Present	Surface Area (m^2/g)	SO_2 Adsorption (mg/g)	SO_2 Adsorption (mg/m^2)	SO_2 Desorption by 700°C (mg/m^2)
Cr_2O_3	$CuCr_2O_4$	26	34.0	1.31	0.84
NiO	-	17	31.9	1.81	1.45
Fe_2O_3	$CuFe_2O_4$	19	38.2	2.01	1.80
In_2O_3	-	25	64.4	2.58	2.27
MnO_2	$Cu_{1.5}Mn_{1.5}O_4$	19	118.6	6.24	4.97
Co_2O_3	$CuCo_2O_4$	7	48.0	6.86	6.48
CuO	-	1	8.3	8.32	5.13

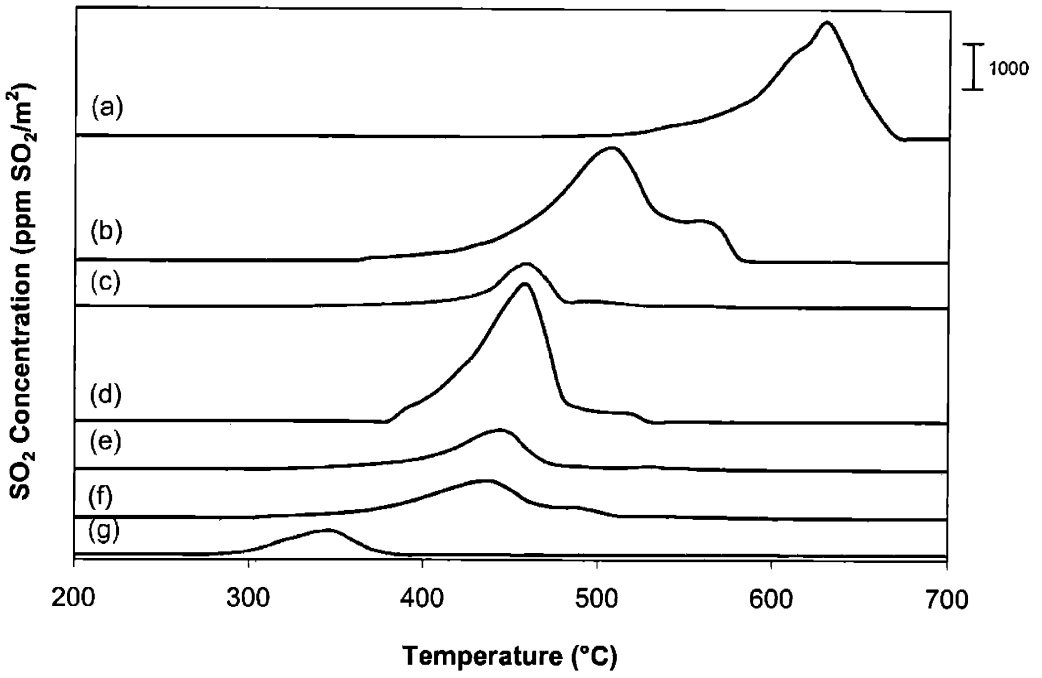

Figure 3.3 TPD of SO_2 over mixed oxides of CuO and (a) MnO_2, (b) Co_2O_3, (c) NiO, (d) CuO, (e) Fe_2O_3, (f) In_2O_3 and (g) Cr_2O_3. Following SO_2 adsorption at 400°C, SO_2 desorption was conducted by introducing 1% O_2 in He at 200°C, and then 2000 ppm CO in He at GHSV ~ 120,000 hr^{-1} and 200-700°C (ramp = 1°C/min).

3.3.1.2 Synthesis and Characteristics of Cr_2O_3-CuO Mixed Oxides

The phase diagram of Cr_2O_3 and CuO shows a mixed phase of $CuCr_2O_4$ at intermediate compositions (Figure 3.4 [15]), which has a spinel crystal structure with I42d symmetry, with Cr^{+3} predominantly at the octahedral sites and Cu^{+2} predominantly at the tetrahedral sites. The phase diagram shows the existence of two regimes: (1) $CuCr_2O_4$ with excess Cr_2O_3 and (2) $CuCr_2O_4$ with excess CuO. The 50 wt% Cr_2O_3-50 wt% CuO material contained 66 mol% CuO, and therefore consisted of $CuCr_2O_4$ with a large excess of CuO.

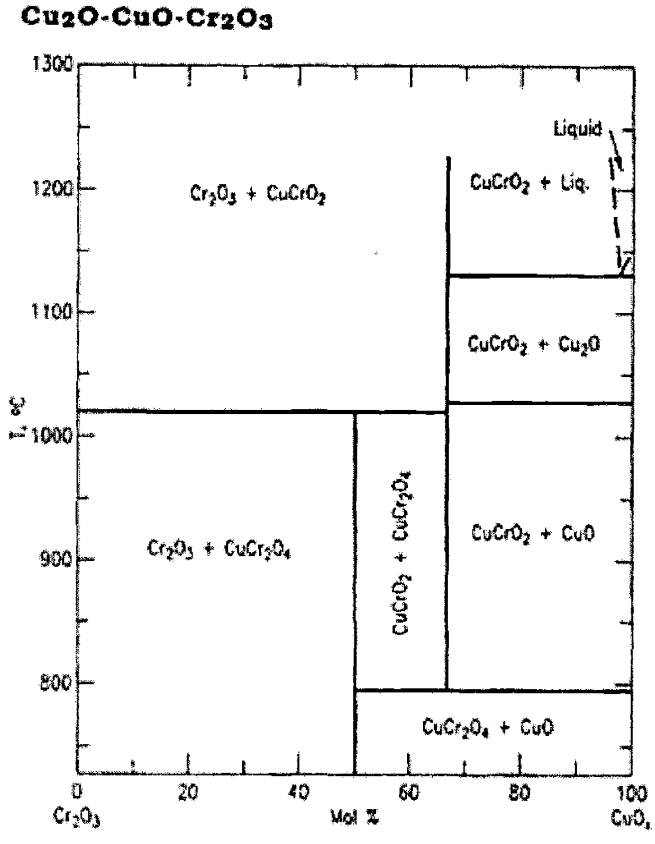

Figure 3.4 Phase diagram of Cr_2O_3 and CuO_x [15].

Cr_2O_3-CuO mixed oxides were synthesized with 0-100% CuO to gain an understanding of the effect of composition on microstructure and SO_2 adsorption/desorption characteristics. Grain sizes were calculated based on the <111>, <211> and <110> peaks of CuO, $CuCr_2O_4$ and Cr_2O_3 phases, respectively. The mixed oxides showed finer grain sizes and higher surface areas compared to pure CuO and pure Cr_2O_3 (Table 3.2). The 66 mol% CuO material achieved the highest surface area of 35 m^2/g with an ultrafine grain size of 13 nm.

Table 3.2 BET surface area and XRD grain size of 500°C-calcined Cr_2O_3-CuO mixed oxides.

CuO Content (mol%)	Surface Area (m^2/g)	Grain Size (nm)
100	7	33 (CuO)
75	24	25 ($CuCr_2O_4$)
66	35	13 ($CuCr_2O_4$)
56	25	18 ($CuCr_2O_4$)
33	10	29 ($CuCr_2O_4$)
0	10	28 (Cr_2O_3)

Phase analysis was performed on the 800°C-calcined Cr_2O_3-CuO mixed oxides (Figure 3.5). At 33 mol% CuO, both Cr_2O_3 and $CuCr_2O_4$ phases were present. The mixed oxides with $\geq$ 56 mol% CuO showed the characteristic peaks of CuO, which increased in intensity with increasing CuO content. The material with 75 mol% CuO consisted of $CuCr_2O_4$, CuO and $CuCrO_2$ phases.

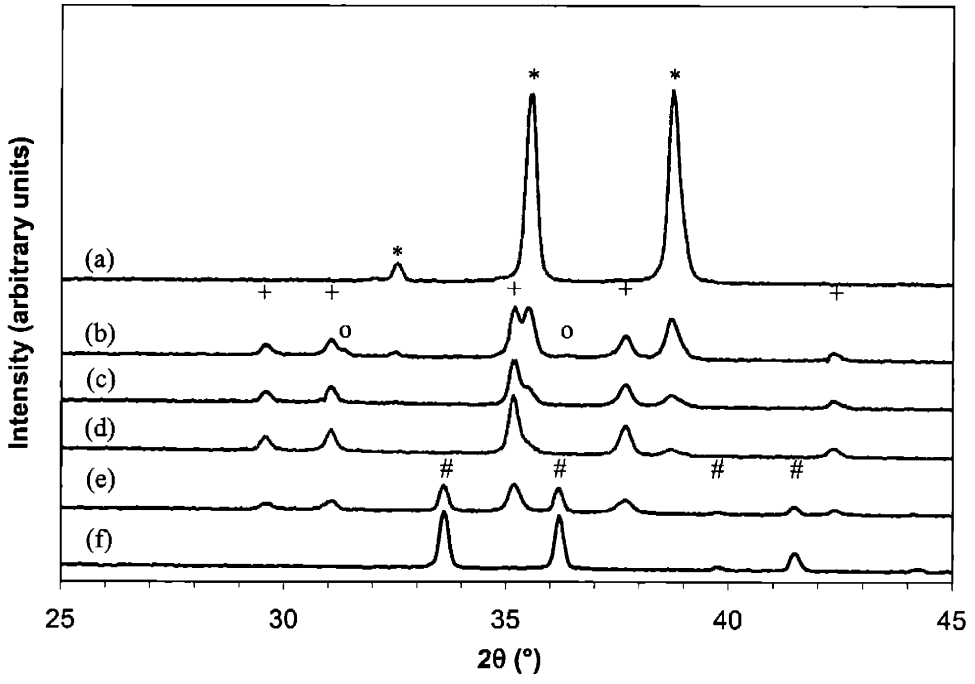

Figure 3.5 XRD patterns of 800°C-calcined Cr_2O_3-CuO mixed oxides with (a) 100%, (b) 75%, (c) 66%, (d) 56%, (e) 33% and (f) 0% CuO. Phases present include (*) CuO, (+) $CuCr_2O_4$, (o) $CuCrO_2$ and (#) Cr_2O_3.

An analysis of SO_2 adsorption capacity was performed for the Cr_2O_3-CuO nanocomposites at 400°C for 2 hours (Table 3.3). On a weight basis, all the materials containing $CuCr_2O_4$ with excess CuO compared quite well with both pure Cr_2O_3 and pure CuO, with the mixed oxide with 75 mol% CuO achieving the highest capacity of 83.5 mg SO_2/g adsorbent. The presence of $CuCr_2O_4$ with excess Cr_2O_3 showed a relatively low capacity of < 40 mg SO_2/g adsorbent. When normalized with respect to surface area, all the mixed oxide materials gave significantly lower capacities than pure Cr_2O_3 and pure CuO. The higher adsorption efficiency for the latter was not unexpected since accessibility of CuO and Cr_2O_3 in bulk absorption would be limited when these single metal oxides were incorporated into the $CuCr_2O_4$ structure. With the exception of the material with 75 mol% CuO, which removed 85% of the inlet SO_2 at a high space velocity of 240,000 hr^{-1}, all other mixed oxides showed < 70% SO_2 removal during the absorption cycle while CuO and Cr_2O_3 achieved 73 and 85% SO_2 removal. SO_2 desorption increased significantly with increasing CuO content from a minimum of 0.01 mg/m^2 for pure Cr_2O_3 to a maximum of 9.4 mg/m^2 for pure CuO. Of the mixed oxides, the material with 75 mol% CuO achieved the highest desorption amount of 2.7 mg/m^2 by 600°C.

Table 3.3 SO_2 adsorption/desorption over 500°C-calcined Cr_2O_3-CuO mixed oxides. A feed of 130 ppm SO_2 and 1% O_2 in He at GHSV ~ 240,000 hr^{-1} and 400°C was used for a two-hour adsorption. Desorption was conducted by introducing 1% O_2 in He at 200°C, and then 2000 ppm CO in He at GHSV ~ 240,000 hr^{-1} and 200-600°C (ramp = 1°C/min).

CuO Content (mol%)	SO_2 Adsorption (mg/g)	SO_2 Adsorption (mg/m^2)	SO_2 Desorption by 600°C (mg/m^2)
100	66.3	9.5	9.4
75	83.5	3.5	2.7
66	76.0	2.2	1.2
56	58.1	2.3	0.7
33	33.3	3.3	0.1
0	73.4	7.3	0.01

For the above analysis, the SO_2 desorbed was < 100% of that adsorbed, suggesting that a portion of the SO_2 remained on the material as sulfate. It was possible, however, that a portion of the SO_2 was oxidized to SO_3 and evolved from the adsorbent

during the adsorption process or that some of the SO_2 was reduced to elemental S over the mixed oxides. Equilibrium analysis confirmed that in the presence of 1% O_2, the conversion of pure Cr_2O_3 to sulfate was favorable with < 1 ppm SO_2 present in the gas stream. However, TGA analysis of the adsorption under similar conditions as in the vertical flow reactor showed the Cr_2O_3-rich materials gained < 0.6 wt% over 2 hours (Figure 3.6). Assuming the weight gain (< 0.6 wt%) was associated with the adsorption of SO_2 and O_2 to form SO_3, this involved < 4.2 mg SO_2/g. In contrast, the presence of excess CuO resulted in significant gains of 6.7 wt% and 11.6 wt% (or 54 mg SO_2/g adsorbent and 90.6 mg SO_2/g adsorbent), respectively, for the oxides with 66 mol% and 100 mol% CuO. Although the TGA studies depended on the proper diffusion of SO_2 to the oxide surface, which could result in a reduced adsorption capacity, this would not account for the order of magnitude difference between the adsorbed quantities measured for the Cr_2O_3-rich materials. Thus, in the vertical flow reactor and the TGA analysis, it was highly likely that some SO_2-to-SO_3 conversion occurred with SO_3 evolving from these materials during the TGA studies, so that no significant weight gain was registered. This agreed well with Kim *et al.*'s analysis of various metal oxides that showed Cr_2O_3 to be very efficient in SO_2-to-SO_3 conversion [16]. Therefore, the presence of excess CuO was necessary to ensure effective SO_2 adsorption.

TPD analysis showed that SO_2 evolution began below 300°C for Cr_2O_3-CuO with SO_2 desorption completing by 375°C (Figure 3.7). In contrast, SO_2 desorption for pure CuO began slightly above 300°C, not completing until 475°C. Cr_2O_3 showed negligible SO_2 desorption at 200-600°C, which was not surprising given its minor weight gain in Figure 3.6 that indicated little SO_2 adsorption.

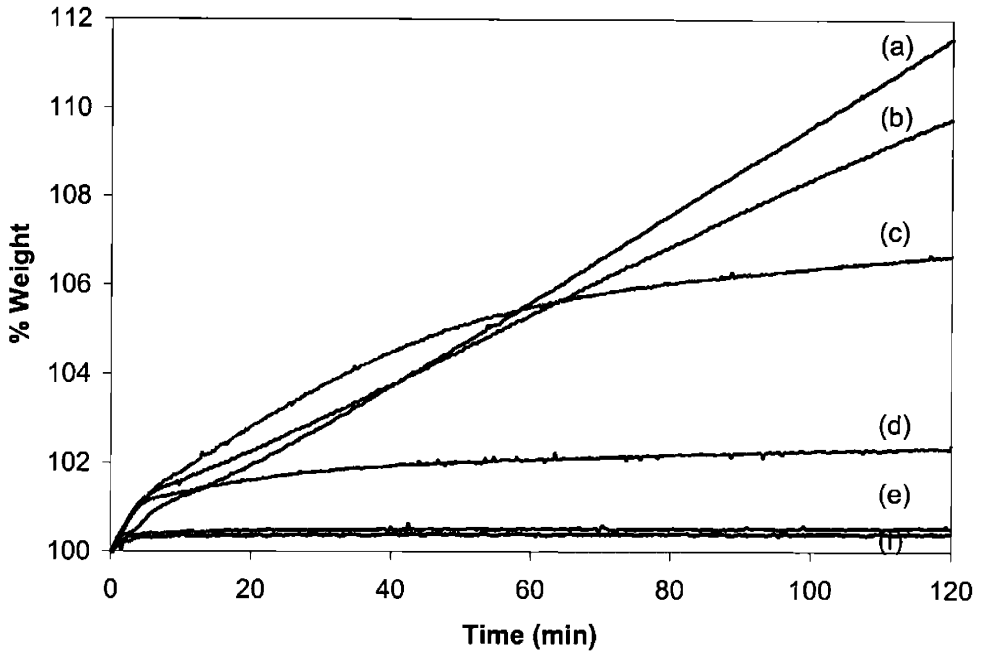

Figure 3.6 Weight gain associated with SO_2 adsorption over 500°C-calcined Cr_2O_3-CuO with (a) 100%, (b) 75%, (c) 66%, (d) 56%, (e) 33% and (f) 0% CuO. The TGA analysis was performed with a feedstream of 130 ppm SO_2 and 1% O_2 in He at a flow rate of 400 sccm and 400°C.

$CuCr_2O_4$ has been known to be active for CO oxidation, which could help promote sulfate removal from the surface [17]. CO_2 was found to evolve below 300°C (Figure 3.8), corresponding well with the SO_2 desorption from the Cr_2O_3-CuO mixed oxides. Lowell *et al.* showed that in the mixed oxide systems, the free energy of sulfate decomposition would be significantly influence by the solid state transition to an alternate phase [14]. This was noted in the $CuCr_2O_4$-containing materials, which were reduced to the $CuCrO_2$ phase in the presence of CO. The significant CO_2 evolution above 400°C for the CuO-rich materials could have resulted from the release and reduction of residual surface sulfates to elemental sulfur. In contrast, Cr_2O_3-rich materials experienced little CO conversion to CO_2.

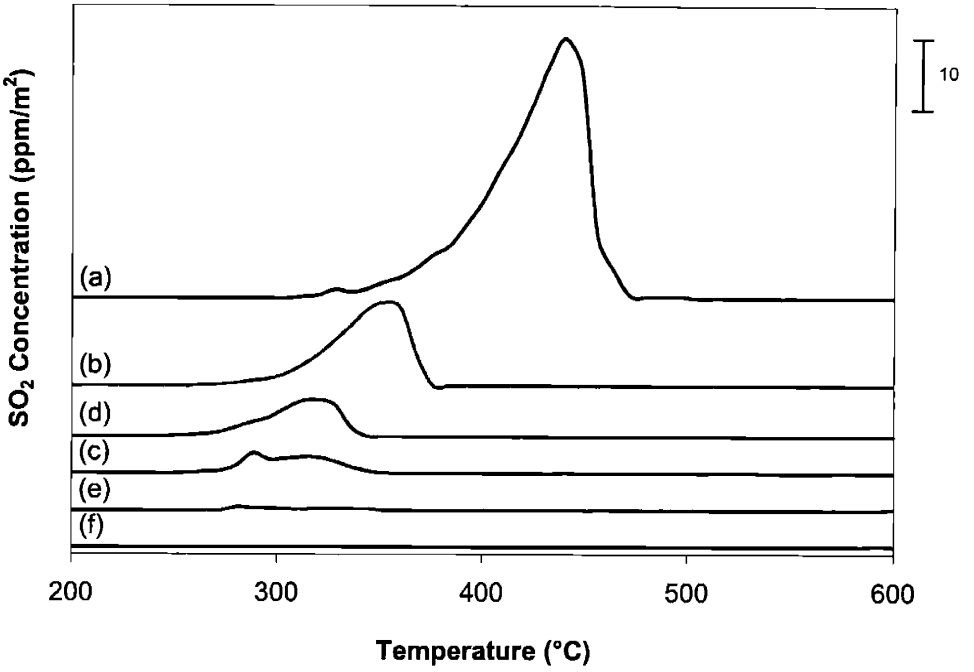

Figure 3.7 TPD of SO_2 over 500°C-calcined Cr_2O_3-CuO with (a) 100%, (b) 75%, (c) 66%, (d) 56%, (e) 33% and (f) 0% CuO. Following SO_2 adsorption at 400°C, SO_2 desorption was conducted by introducing 1% O_2 in He at 200°C, and then 2000 ppm CO in He at GHSV ~ 240,000 hr^{-1} and 200-600°C (ramp = 1°C/min).

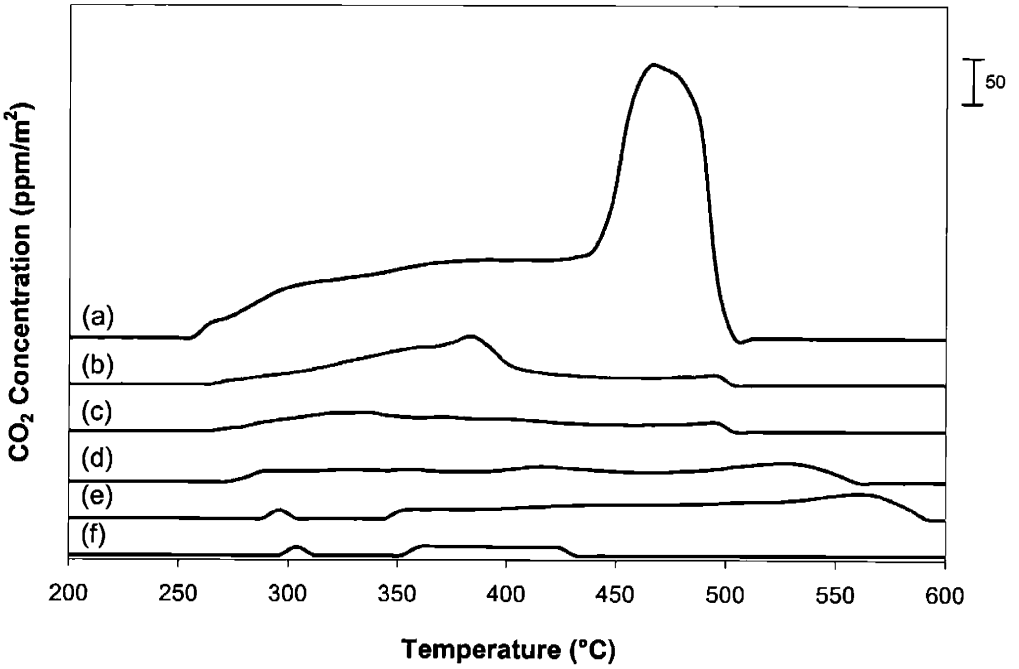

Figure 3.8 CO_2 evolution corresponding to the SO_2 TPD over 500°C-calcined Cr_2O_3-CuO with (a) 100%, (b) 75%, (c) 66%, (d) 56%, (e) 33% and (f) 0% CuO. Following SO_2 adsorption at 400°C, SO_2 desorption was conducted by introducing 1% O_2 in He at 200°C, and then 2000 ppm CO in He at GHSV ~ 240,000 hr^{-1} and 200-600°C (ramp = 1°C/min).

3.3.2 Doping of $CuCr_2O_4$ for Improved SO_2 Sorption Characteristics

Results in Section 3.3.1.2 indicated that Cr_2O_3-CuO mixed oxides provided for low-temperature SO_2 desorption, which might be attributed to the presence of the $CuCr_2O_4$ phase. However, the adsorption capacity of phase-pure $CuCr_2O_4$ was lower than the mixed phase Cr_2O_3-CuO nanocomposites, especially the CuO-rich materials. Substitution of secondary ions into the $MgAl_2O_4$ spinel crystal structure has been shown to significantly affect the SO_2 sorption characteristics [8, 18]. The introduction of various dopants was found to have a significant impact on the CO oxidation properties of $CuCr_2O_4$. For example, the doping of Al^{+3} resulted in Cu presence at the tetrahedral and octahedral sites and converted some Cu^{+2} to Cu^{+1}, causing a decrease in CO oxidation activity; whereas doping with Rh^{+3} forced the Cu to remain in the more active tetrahedral site, leading to increased oxidation activity [19]. Therefore, introduction of appropriate dopant ions might enhance the adsorption capacity of $CuCr_2O_4$, as well as decrease desorption temperature and improve regenerability, which would be very attractive for use in conjunction with a NO_x trap in automotive applications.

3.3.2.1 Synthesis and Sorption Characteristics of $Cu_{0.95}M_{0.05}Cr_2O_4$

Fe, Co, and Ni cations were selected for doping at the Cu site of $CuCr_2O_4$ since they would form the spinel crystal structure with Cr_2O_3 and have similar ionic radius as Cu^{+2} (Table 3.4). Upon calcination at 500°C, $Cu_{0.95}Co_{0.05}Cr_2O_4$ exhibited the lowest grain size (23 nm) and highest surface area (37 m^2/g), which was three times that of undoped $CuCr_2O_4$ (12 m^2/g). The <111> XRD peak of the Si reference was used along with the <211> and <200> peaks of 1000°C-calcined $Cu_{0.95}M_{0.05}Cr_2O_4$ to evaluate lattice expansion of the latter. Co, Fe and Ni dopants expanded the *c* lattice parameter by 1.6%, 1.3% and 0.8%, respectively. The *a* lattice parameters of the $Cu_{0.95}M_{0.05}Cr_2O_4$ were within experimental error as that of $CuCr_2O_4$.

Table 3.4 Effect of dopant composition on the surface area and grain size of 500°C-calcined $Cu_{0.95}M_{0.05}Cr_2O_4$. Lattice parameters of $Cu_{0.95}M_{0.05}Cr_2O_4$ were determined following calcination to 1000°C.

Dopant (M)	Surface Area (m^2/g)	Grain Size (nm)	Ionic Radius (Å)	Lattice Parameter *a* (Å)	Lattice Parameter *c* (Å)
Fe	14	33	0.74	6.029	7.865
Co	37	23	0.72	6.024	7.886
Ni	15	29	0.69	6.026	7.828
Cu	12	29	0.72	6.030	7.763

SO_2 adsorption analysis was performed on $Cu_{0.95}M_{0.05}Cr_2O_4$ to determine the effect of tetrahedral dopant (Table 3.5). $Cu_{0.95}Co_{0.05}Cr_2O_4$ achieved the highest capacity of 71.8 mg SO_2/g adsorbent, similar to that achieved by Cr_2O_3-CuO containing 66 mol% CuO. The equilibrium SO_2 adsorption of 72% was nearly 2 times higher than that of $CuCr_2O_4$ (37%). This increased adsorption and conversion could be attributed to the higher surface area of $Cu_{0.95}Co_{0.05}Cr_2O_4$, and when normalized by surface area, this material had a relatively low adsorption of 1.93 mg/m^2. $Cu_{0.95}M_{0.05}Cr_2O_4$ doped with Fe, Co and Ni showed less SO_2 desorption than $CuCr_2O_4$ (0.21 mg/m^2) by 500°C, but all four materials provided for complete desorption below 375°C (Figure 3.9). We note that the amount desorbed from $Cu_{0.95}M_{0.05}Cr_2O_4$ was much less than the CuO-rich Cr_2O_3-CuO mixed oxides (Table 3.3). This study illustrated that the $CuCr_2O_4$ phase was responsible for the low desorption temperature in Cr_2O_3-CuO mixed oxides, while the presence of CuO phase was critical for promoting SO_2 desorption.

Table 3.5 SO_2 adsorption/desorption over 500°C-calcined $Cu_{0.95}M_{0.05}Cr_2O_4$. A feed of 130 ppm SO_2 and 1% O_2 in He at GHSV ~ 240,000 hr^{-1} and 400°C was used for a two-hour adsorption. Desorption was conducted by introducing 1% O_2 in He at 200°C, and then 2000 ppm CO in He at GHSV ~ 240,000 hr^{-1} and 200-500°C (ramp = 1°C/min).

Dopant (M)	SO_2 Adsorption (mg/g)	SO_2 Adsorption (mg/m^2)	SO_2 Desorption by 500°C (mg/m^2)
Fe	34.9	2.47	0.17
Co	71.8	1.93	0.14
Ni	43.5	2.91	0.07
Cu	38.8	3.23	0.21

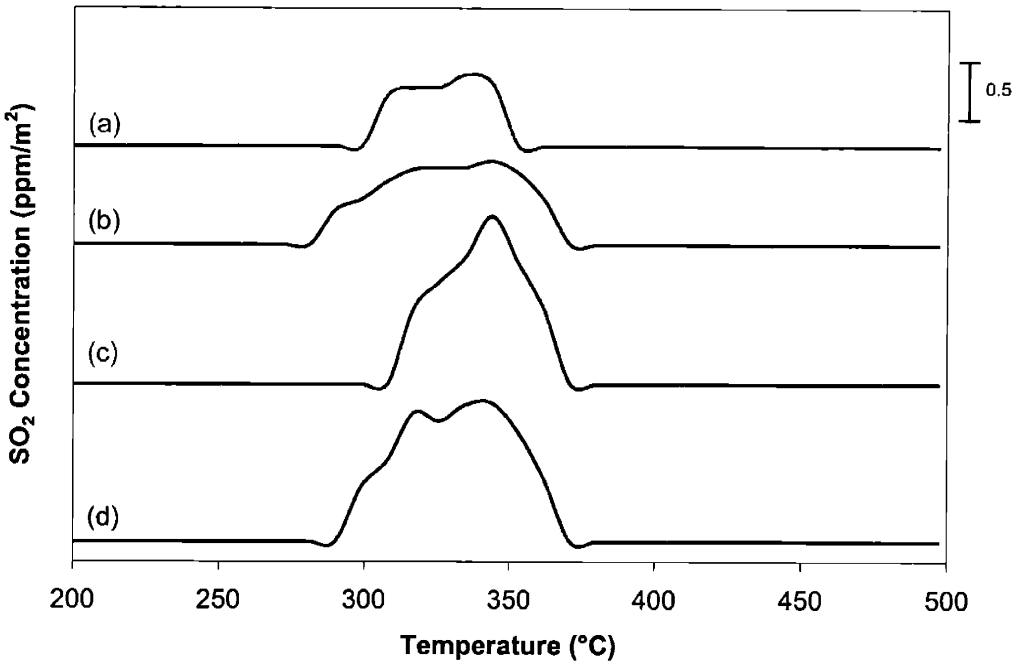

Figure 3.9 TPD of SO_2 over 500°C-calcined $Cu_{0.95}M_{0.05}Cr_2O_4$ with M = (a) Fe, (b) Co, (c) Ni and (d) Cu. Following SO_2 adsorption at 400°C, SO_2 desorption was conducted by introducing 1% O_2 in He at 200°C, and then 2000 ppm CO in He at GHSV ~ 240,000 hr^{-1} and 200-500°C (ramp = 1°C/min).

3.3.2.2 Synthesis and Sorption Characteristics of $CuCr_{1.9}M_{0.1}O_4$

Al, Fe, Co, and Ni were selected for doping at the Cr site of $CuCr_2O_4$ since they all would form the spinel crystal structure with CuO and have a similar ionic radius as Cr^{+3} (Table 3.6). Amongst the $CuCr_{1.9}M_{0.1}O_4$ material, $CuCr_{1.9}Co_{0.1}O_4$ achieved the finest grain size of 17 nm with a high surface area of 25 m^2/g. For $CuCr_{1.9}M_{0.1}O_4$ with M = Al, Fe, Co and Ni, there was a slight contraction in *a* of < 0.3% compared to $CuCr_2O_4$. In contrast, substantial expansion in *c* was noted with doping of $CuCr_2O_4$; most notably, $CuCr_{1.9}Co_{0.1}O_4$ showed a 2.8% increase in *c* compared to $CuCr_2O_4$.

Table 3.6 Effect of dopant composition on the surface area and grain size of 500°C-calcined $CuCr_{1.9}M_{0.1}O_4$. Lattice Parameters of $CuCr_{1.9}M_{0.1}O_4$ were determined following calcination to 1000°C.

Dopant (M)	Surface Area (m^2/g)	Grain Size (nm)	Ionic Radius (Å)	Lattice Parameter *a* (Å)	Lattice Parameter *c* (Å)
Al	28	28	0.51	6.015	7.853
Cr	12	29	0.63	6.030	7.763
Fe	21	29	0.64	6.026	7.827
Co	25	17	0.63	6.016	7.987
Ni	27	25	0.69*	6.014	7.935

* Based on a +2 oxidation state for nickel cation.

Unlike $Cu_{0.95}M_{0.05}Cr_2O_4$ materials, which showed a single phase in the XRD patterns, the $CuCr_{1.9}M_{0.1}O_4$ materials with the exception of M = Al consisted of a minor second phase based on $CuCrO_2$, the reduced form of $CuCr_2O_4$. This could have formed as a result of a minor non-stoichiometry or partial substitution of the dopant ion at the Cu site. Although non-stoichiometry was a possibility, it was unlikely since $CuCr_{1.9}Al_{0.1}O_4$ showed no evidence of $CuCrO_2$. On the other hand, $CuCr_{1.9}Ni_{0.1}O_4$ consisted of the highest $CuCrO_2$ content. As the Ni dopant would only adopt a +2 oxidation state, it was highly likely that there was partial substitution of dopant at the Cu site to give rise to the secondary $CuCrO_2$ phase.

Doping of Al, Fe, Co and Ni at the octahedral site of $CuCr_2O_4$ produced materials with improved SO_2 sorption characteristics (Table 3.7). As with $Cu_{0.95}M_{0.05}Cr_2O_4$, Co doping led to a high capacity on a weight basis (58.5 mg SO_2/g) in $CuCr_{1.9}M_{0.1}O_4$. On the basis of surface area, $CuCr_{1.9}Co_{0.1}O_4$ demonstrated a high capacity of 2.32 mg SO_2/m^2. $CuCr_{1.9}Co_{0.1}O_4$ also gave rise to a significantly larger amount of SO_2 desorption of 0.48 mg/m^2 than pure $CuCr_2O_4$ (0.21 mg/m^2) by 500°C.

Table 3.7 SO_2 adsorption/desorption over 500°C-calcined $CuCr_{1.9}M_{0.1}O_4$. A feed of 130 ppm SO_2 and 1% O_2 in He at GHSV ~ 240,000 hr^{-1} and 400°C was used for a two-hour adsorption. Desorption was conducted by introducing 1% O_2 in He at 200°C, and then 2000 ppm CO in He at GHSV ~ 240,000 hr^{-1} and 200-500°C (ramp = 1°C/min).

Dopant (M)	SO_2 Adsorption (mg/g)	SO_2 Adsorption (mg/m^2)	SO_2 Desorption by 500°C (mg/m^2)
Al	60.0	2.14	0.12
Cr	38.8	3.23	0.21
Fe	47.7	2.24	0.13
Co	58.5	2.32	0.48
Ni	26.7	0.98	0.10

TPD studies illustrated that $CuCr_{1.9}Co_{0.1}O_4$ facilitated SO_2 desorption between 250°C and 350°C, with a peak at 295°C (Figure 3.10). In contrast, $CuCr_2O_4$'s desorption took place at a higher temperature range of 290-375°C. $CuCr_{1.9}Co_{0.1}O_4$'s peak SO_2 evolution temperature range correlated well with a significant CO_2 formation peak at 270-350°C (Figure 3.11 (b)).

A TGA analysis of weight gain with temperature over 2 hours showed ~ 18 mg SO_2 adsorbed/g adsorbent (0.72 mg/m^2) for $Cu_{1.9}Co_{0.1}O_4$, which was ~ 31% of that obtained in the vertical flow reactor analysis (see Table 3.7). Assuming that the SO_2 adsorption determined by TGA reflected the true adsorption of SO_2 in the vertical reactor analysis, the 0.48 mg SO_2 desorbed/m^2 still did not equate to the SO_2 adsorbed. Therefore, it was likely that at least a portion of the CO_2 conversion seen at elevated temperatures resulted from the removal and reduction of strongly bound sulfate species.

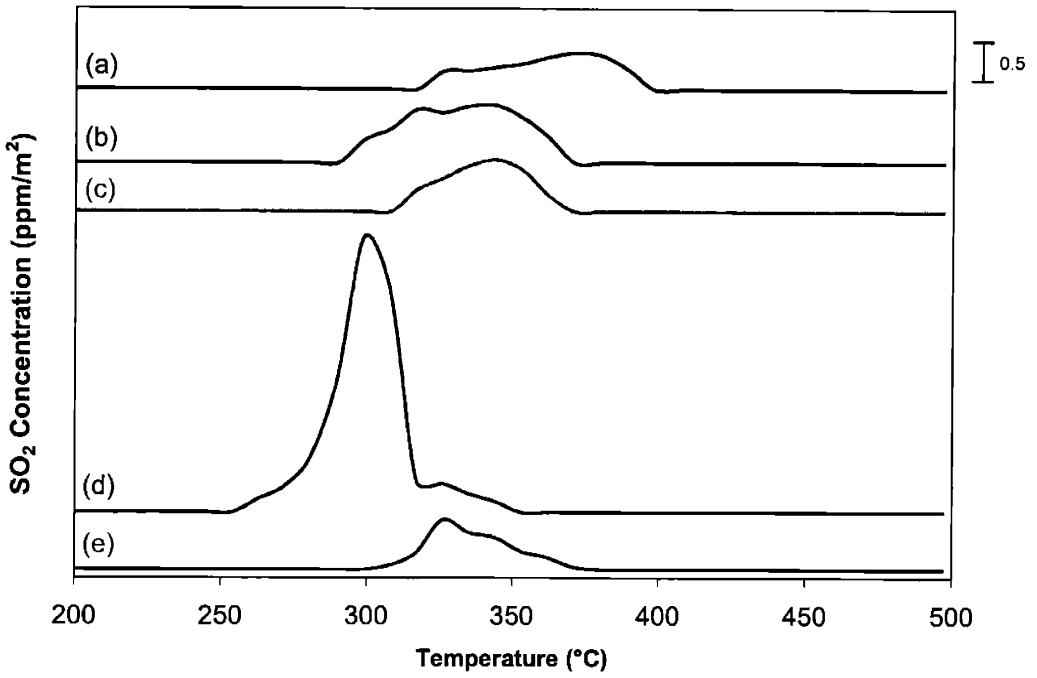

Figure 3.10 TPD of SO_2 over 500°C-calcined $CuCr_{1.9}M_{0.1}O_4$ with M = (a) Al, (b) Cr, (c) Fe, (d) Co and (e) Ni. Following SO_2 adsorption at 400°C, SO_2 desorption was conducted by introducing 1% O_2 in He at 200°C, and then 2000 ppm CO in He at GHSV ~ 240,000 hr^{-1} and 200-500°C (ramp = 1°C/min).

The improved low-temperature SO_2 evolution associated with $CuCr_{1.9}O_{0.1}O_4$ might be attributed to Co doping at the Cr site of $CuCr_2O_4$, which led to an ultrafine grain size of 17 nm and promoted the low-temperature CO_2 conversion. These unique characteristics in turn facilitated SO_2 release from the adsorbent compared to undoped $CuCr_2O_4$ and $CuCr_{1.9}M_{0.1}O_4$ doped with Al, Fe and Ni. Compared to $Cu_{0.95}Co_{0.05}Cr_2O_4$, $CuCr_{1.9}Co_{0.1}O_4$ showed > three times greater SO_2 desorption by 500°C, illustrating the advantage of Co doping at the octahedral Cr site. To further optimize the effect of Co doping, the $CuCr_{2-y}Co_yO_4$ series was examined for y = 0.00, 0.05, 0.10, 0.15 and 0.20.

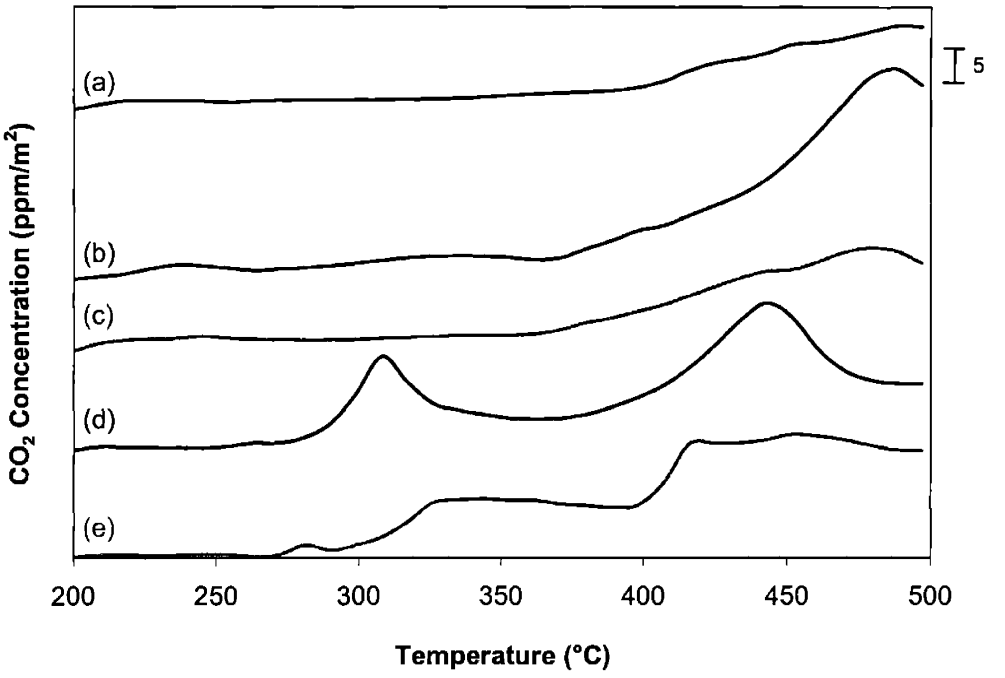

Figure 3.11 CO_2 evolution corresponding to the SO_2 TPD over 500°C-calcined $CuCr_{1.9}M_{0.1}O_4$ with M = (a) Al, (b) Cr, (c) Fe, (d) Co and (e) Ni. Following SO_2 adsorption at 400°C, SO_2 desorption was conducted by introducing 1% O_2 in He at 200°C, and then 2000 ppm CO in He at GHSV ~ 240,000 hr^{-1} and 200-500°C (ramp = 1°C/min).

3.3.2.3 Synthesis and Sorption Characteristics of $CuCr_{2-y}Co_yO_4$

Table 3.8 illustrates that surface area increased and grain size decreased in $CuCr_{2-y}Co_yO_4$ with increased Co-doping. A high surface area of 27 m^2/g and an ultrafine grain size of 13 nm were attained by $CuCr_{1.8}Co_{0.2}O_4$. Table 3.8 showed the steady contraction in *a* and expansion in *c* with increased Co doping in $CuCr_{2-y}Co_yO_4$. Compared to $CuCr_2O_4$, $CuCr_{1.8}Co_{0.2}O_4$ had a 3% increase in unit cell (from 282 to 291 $Å^3$).

Table 3.8 Effect of dopant concentration on surface area and grain size of 500°C-calcined $CuCr_{2-y}Co_yO_4$. Lattice parameters of $CuCr_{2-y}Co_yO_4$ were determined following calcination to 1000°C.

			Lattice Parameter	
	Surface Area	Grain Size	*a*	*c*
y	(m^2/g)	(nm)	(Å)	(Å)
0.00	12	29	6.030	7.763
0.05	22	19	6.020	7.854
0.10	25	16	6.012	7.872
0.15	25	14	6.000	7.934
0.20	27	13	5.985	8.130

Phase purity of the $CuCr_{2-y}Co_yO_4$ materials was analyzed after calcination to 1000°C (Figure 3.12). The Co-doped samples consisted of a $CuCrO_2$ secondary phase in addition to $CuCr_2O_4$. With increasing Co content, the peak intensity of the secondary phase increased while the peak shift (from 2θ = 35.159°) associated with *c* lattice expansion became more apparent. The extensive crystal structure deformation resulted in the resolution of the <202> and <103> peaks located at 2θ = 37.69° in the undoped $CuCr_2O_4$.

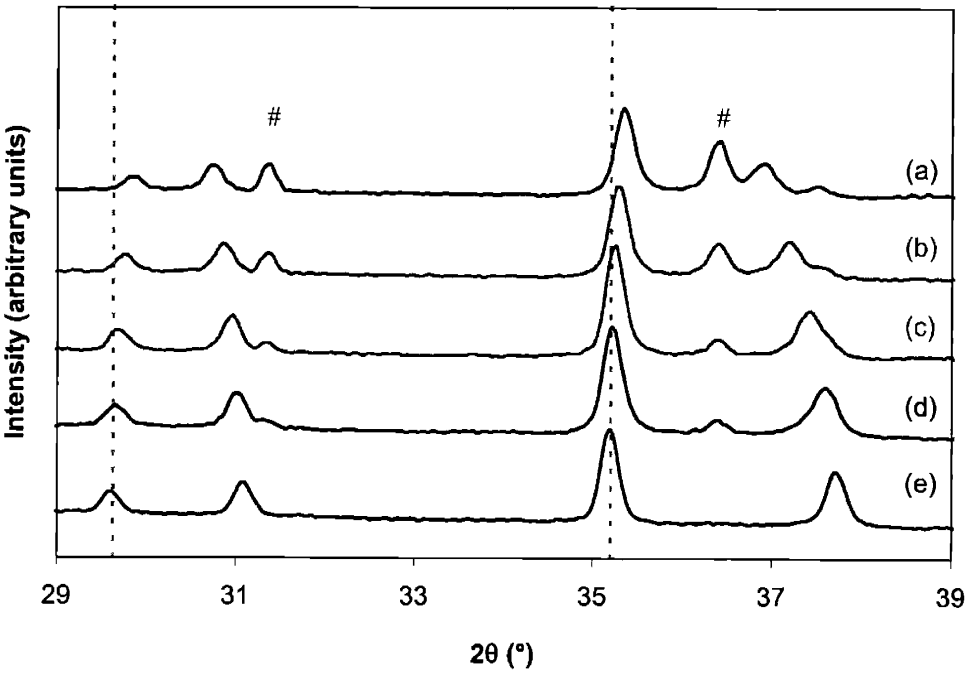

Figure 3.12 XRD patterns of 1000°C-calcined $CuCr_{2-y}Co_yO_4$ with *y* = (a) 0.20, (b) 0.15, (c) 0.10, (d) 0.05 and (e) 0.00. Besides the $CuCr_2O_4$ phase, peaks associated with the secondary $CuCrO_2$ phase were noted (#) in the Co-doped samples.

The Co-doped materials achieved significantly higher capacities on a weight basis than $CuCr_2O_4$ (Table 3.9). They all showed equilibrium conversions of > 55%, much higher than the 37% attained by the pure phase $CuCr_2O_4$. $CuCr_{1.8}Co_{0.2}O_4$ has the highest capacity of 64.1 mg SO_2/g adsorbent with 62% conversion. When analyzed on the basis of surface area, the $CuCr_{2-y}Co_yO_4$ materials adsorbed ~2.3-2.4 mg SO_2/m^2, which were less than the 3.2 mg SO_2/m^2 noted for pure $CuCr_2O_4$. $CuCr_{2-y}Co_yO_4$ showed increased SO_2 desorption by 500°C with increased Co concentration. $CuCr_{1.8}Co_{0.2}O_4$ gave the maximum desorption of 0.60 mg/m^2, which was almost three times higher than that of $CuCr_2O_4$.

Table 3.9 SO_2 adsorption/desorption over 500°C-calcined $CuCr_{1-y}Co_yO_4$. A feed of 130 ppm SO_2 and 1% O_2 in He at GHSV ~ 240,000 hr^{-1} and 400°C was used for a two-hour adsorption. Desorption was conducted by introducing 1% O_2 in He at 200°C, and then 2000 ppm CO in He at GHSV ~ 240,000 hr^{-1} and 200-500°C (ramp = 1°C/min).

y	SO_2 Adsorption (mg/g)	SO_2 Adsorption (mg/m^2)	SO_2 Desorption by 500°C (mg/m^2)
0.00	38.8	3.23	0.21
0.05	52.6	2.40	0.27
0.10	58.5	2.32	0.48
0.15	57.6	2.35	0.51
0.20	64.1	2.39	0.60

TPD of SO_2 showed that Co doping facilitated SO_2 desorption in $CuCr_{1-y}Co_yO_4$, and provided for SO_2 evolution at low temperatures (Figure 3.13). The low-temperature CO_2 evolution from $CuCr_{2-y}Co_yO_4$ correlated well with the SO_2 desorption (Figure 3.14). Significant CO_2 evolution below 300°C was noted for $CuCr_{2-y}Co_yO_4$ with $y \geq 0.10$, which corresponded nicely with the sharp SO_2 desorption from these Co-doped materials at the similar temperature range. All the $CuCr_{2-y}Co_yO_4$ materials showed major CO_2 evolution above 380°C, which could be associated with the removal and reduction of surface sulfate.

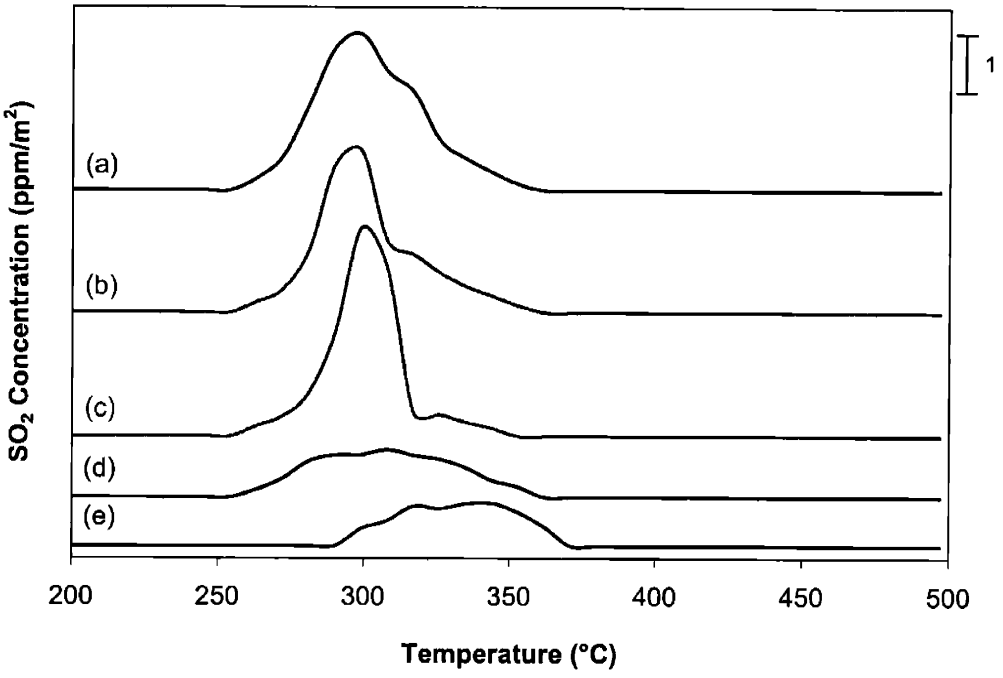

Figure 3.13 TPD of SO_2 over 500°C-calcined $CuCr_{2-y}Co_yO_4$ with y = (a) 0.20, (b) 0.15, (c) 0.10, (d) 0.05 and (e) 0.00. Following SO_2 adsorption at 400°C, SO_2 desorption was conducted by introducing 1% O_2 in He at 200°C, and then 2000 ppm CO in He at GHSV ~ 240,000 hr^{-1} and 200-500°C (ramp = 1°C/min).

Through introduction of dopants in $CuCr_2O_4$, particularly Co at the Cr site, we were able to significantly improve the low-temperature SO_2 desorption. However, the presence of excess CuO might be necessary to avoid SO_3 bypass (which would poison the downstream NO_x storage material) and promote complete SO_2 desorption. Thus, it would be of great interest to combine CuO with $CuCr_{2-y}Co_yO_4$ through different synthetic approaches to achieve a multifunctional SO_2 adsorbent with the desired microstructure, adsorption capacity, desorption temperature and regenerability.

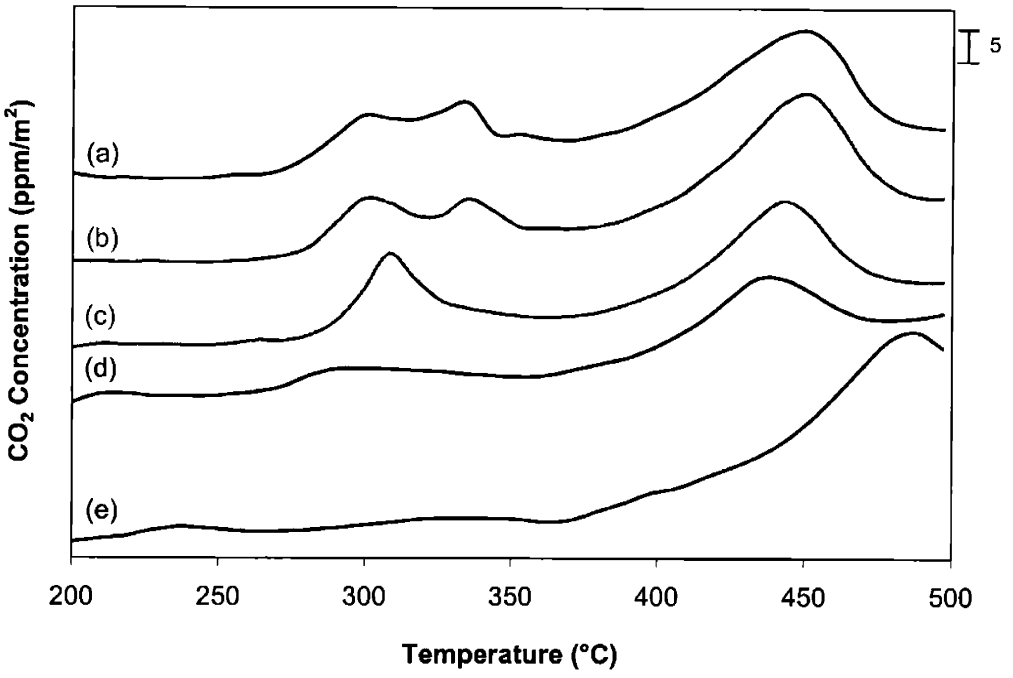

Figure 3.14 CO_2 evolution corresponding to the SO_2 TPD over 500°C-calcined $CuCr_{2-y}Co_yO_4$ with y = (a) 0.20, (b) 0.15, (c) 0.10, (d) 0.05 and (e) 0.00. Following SO_2 adsorption at 400°C, SO_2 desorption was conducted by introducing 1% O_2 in He at 200°C, and then 2000 ppm CO in He at GHSV ~ 240,000 hr^{-1} and 200-600°C (ramp = 1°C/min).

3.3.3 Adsorption Performance of $CuO/CuCr_{1.9}Co_{0.1}O_4$ Materials

3.3.3.1 Synthesis and Characteristics of $CuO/CuCr_{1.9}Co_{0.1}O_4$

Various synthesis routes were examined to control the dispersion and phase composition of $CuO/CuCr_{1.9}Co_{0.1}O_4$ system with a total of 50 cation% Cu: (1) chemical co-precipitation of $CuCr_{1.9}Co_{0.1}O_4$ and CuO (CP), (2) chemical precipitation of $Cu(OH)_2$ onto the pre-precipitated $CuCr_{1.9}Co_{0.1}(OH)_8$ (PP), (3) chemical precipitation of the $CuCr_{1.9}Co_{0.1}(OH)_8$ onto pre-precipitated $Cu(OH)_2$ (RP), and (4) impregnation of pre-calcined $CuCr_{1.9}Co_{0.1}(OH)_8$ precipitate with copper nitrate (IP). Following synthesis, these materials were calcined to 500°C, and compared with Cr_2O_3-CuO with 66 mol% CuO (i.e. $CuO/CuCr_2O_4$ with 50 cation% Cu) and $CuCr_{1.9}Co_{0.1}O_4$.

The four different methods all led to $CuO/CuCr_{1.9}Co_{0.1}O_4$ materials with high surface areas of $\geq$ 25 m^2/g (Table 3.10). Their ultrafine grain sizes of 13-16 nm for the

$CuCr_2O_4$ phase was similar to that achieved by $Cu/CuCr_2O_4$ (13 nm). All six materials in Table 3.10 showed a slight contraction in *a* and an expansion in *c* relative to pure $CuCr_2O_4$ phase (6.030 Å and 7.763 Å, respectively). This suggested that the presence of excess CuO resulted in the partial substitution of Cu at the Cr site in the case of the $CuO/CuCr_2O_4$ without Co doping.

Table 3.10 Surface area and grain size of 500°C-calcined $CuCr_{1.9}Co_{0.1}O_4$, $CuO/CuCr_{1.9}Co_{0.1}O_4$ (synthesized by 4 different methods) and $CuO/CuCr_2O_4$. Lattice parameters of the $CuCr_2O_4$ phase were determined following calcination at 1000°C.

Material	Surface Area (m^2/g)	$CuCr_2O_4$ Grain Size (nm)	Lattice Parameter *a* (Å)	Lattice Parameter *c* (Å)
$CuCr_{1.9}Co_{0.1}O_4$	25	16	6.012	7.872
$CuO/CuCr_{1.9}Co_{0.1}O_4$ (CP)	25	15	6.011	7.802
$CuO/CuCr_{1.9}Co_{0.1}O_4$ (PP)	25	13	6.011	7.869
$CuO/CuCr_{1.9}Co_{0.1}O_4$ (RP)	34	14	6.009	7.856
$CuO/CuCr_{1.9}Co_{0.1}O_4$ (IP)	25	16	6.012	7.997
$CuO/CuCr_2O_4$	35	13	6.011	7.873

Phase purity of the supported CuO materials was analyzed after calcination to 800°C. Except for $CuCr_{1.9}Co_{0.1}O_4$, the presence of excess CuO was evident in the samples illustrated in Figure 3.15. The $CuO/CuCr_{1.9}Co_{0.1}O_4$ material synthesized by the RP method and $CuO/CuCr_2O_4$ exhibited broader CuO peaks, indicating a finer CuO grain size.

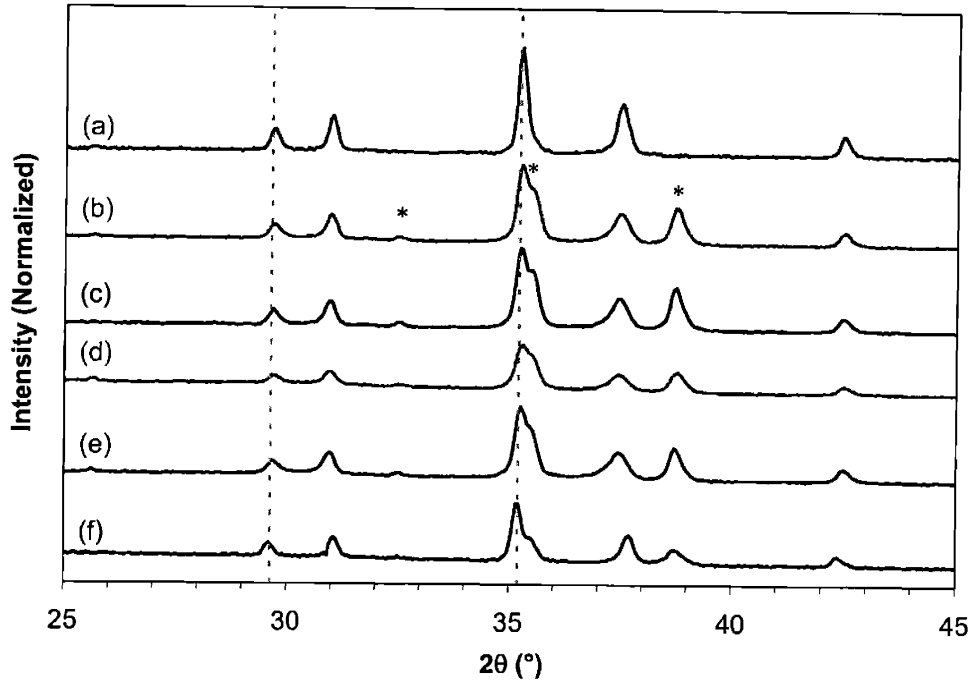

Figure 3.15 XRD patterns of 800°C-calcined (a) $CuCr_{1.9}Co_{0.1}O_4$, $CuO/CuCr_{1.9}Co_{0.1}O_4$ prepared by (b) CP, (c) PP, (d) RP and (e) IP methods, and (f) $CuO/CuCr_2O_4$. Besides the $CuCr_2O_4$ phase (↓), peaks associated with the secondary CuO phase were noted (*).

SO_2 adsorption capacities were high (> 55 mg SO_2/g and > 2.03 mg SO_2/m^2) for all materials in Table 3.11 except $CuO/CuCr_{1.9}Co_{0.1}O_4$ (IP) (48.2 mg SO_2/g and 1.93 mg SO_2/m^2). The five materials with excess CuO showed substantially higher SO_2 desorption by 500°C compared to $CuCr_{1.9}O_{0.1}O_4$ (0.48 mg SO_2/m^2). $CuO/CuCr_{1.9}Co_{0.1}O_4$ prepared by the PP and IP methods gave relatively lower SO_2 desorption of 0.60 mg/m^2 and 0.61 mg/m^2, respectively, compared to that synthesized by RP and CP methods (1.16 mg/m^2 and 1.24 mg/m^2, respectively). $CuO/CuCr_2O_4$ showed the highest SO_2 desorption of 1.61 mg/m^2 by 500°C.

Table 3.11 SO_2 adsorption/desorption over 500°C-calcined materials. A feed of 130 ppm SO_2 and 1% O_2 in He at GHSV ~ 240,000 hr^{-1} and 400°C was used for a two-hour adsorption. Desorption was conducted by introducing 1% O_2 in He at 200°C, and then 2000 ppm CO in He at GHSV ~ 240,000 hr^{-1} and 200-500°C (ramp = 1°C/min).

Material	SO_2 Adsorption (mg/g)	SO_2 Adsorption (mg/m^2)	SO_2 Desorption by 500°C (mg/m^2)
$CuCr_{1.9}Co_{0.1}O_4$	58.5	2.32	0.48
$CuO/CuCr_{1.9}Co_{0.1}O_4$ (CP)	55.0	2.20	1.24
$CuO/CuCr_{1.9}Co_{0.1}O_4$ (PP)	59.7	2.39	0.60
$CuO/CuCr_{1.9}Co_{0.1}O_4$ (RP)	69.0	2.03	1.16
$CuO/CuCr_{1.9}Co_{0.1}O_4$ (IP)	48.2	1.93	0.61
$CuO/CuCr_2O_4$	76.0	2.17	1.61

Figure 3.16 showed that the presence of excess CuO gave rise to greater SO_2 desorption. In all six samples, desorption was initiated just above 250°C and was completed by 400°C. However, the TPD profile was heavily dependent on the synthesis method for the $CuO/CuCr_{1.9}Co_{0.1}O_4$ system. The $CuO/CuCr_2O_4$ sample achieved full SO_2 desorption at a lower temperature than the four $CuO/CuCr_{1.9}Co_{0.1}O_4$ samples. However, improved SO_2 desorption below 300°C was attained with the $CuO/CuCr_{1.9}Co_{0.1}O_4$ samples prepared by the PP and IP methods, suggesting the benefit of pre-forming the $CuCr_{1.9}Co_{0.1}O_4$ particles prior to the deposition of CuO. Of the four $CuO/CuCr_{1.9}Co_{0.1}O_4$ samples, the one prepared by the CP method showed the greatest amount of SO_2 desorption and completed the SO_2 evolution by the lowest temperature (360°C).

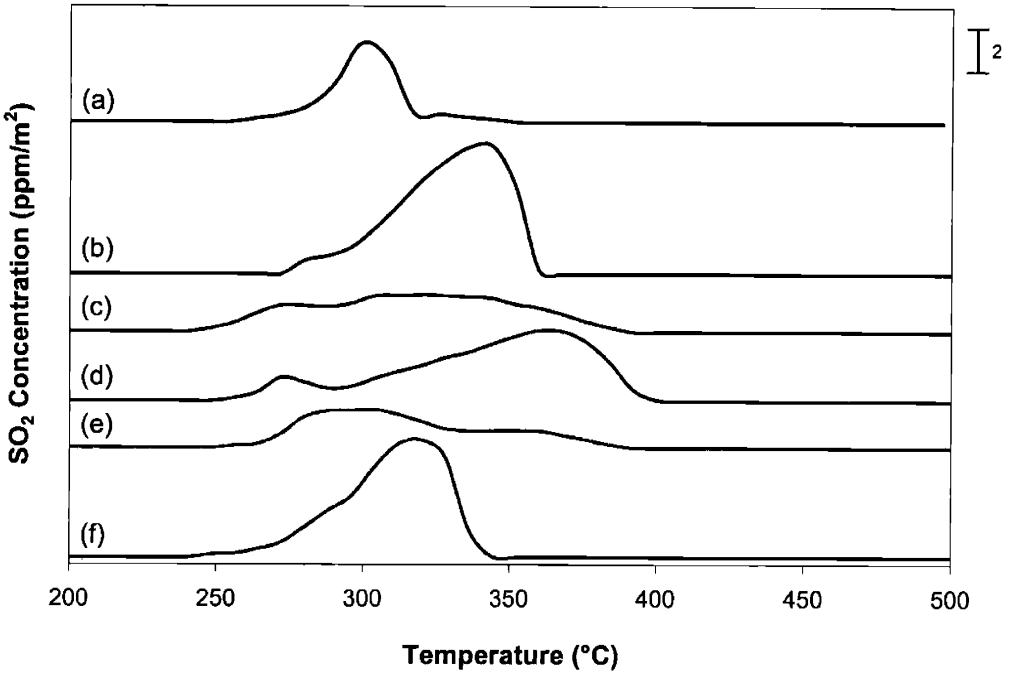

Figure 3.16 TPD of SO_2 over 500°C-calcined (a) $CuCr_{1.9}Co_{0.1}O_4$, $CuO/CuCr_{1.9}Co_{0.1}O_4$ prepared by (b) CP, (c) PP, (d) RP and (e) IP methods, and (f) $CuO/CuCr_2O_4$. Following SO_2 adsorption at 400°C, SO_2 desorption was conducted by introducing 1% O_2 in He at 200°C, and then 2000 ppm CO in He at GHSV ~ 240,000 hr^{-1} and 200-500°C (ramp = 1°C/min).

All the materials experienced similar low-temperature CO oxidation activity (Figure 3.17), which correlated well with the onset of SO_2 desorption. Also evident from the CO_2 profiles was enhanced CO conversion between 350°C and 450°C for the Co-doped systems. The presence of multiple CO_2 peaks suggested that further SO_x evolved from the adsorbent above 400°C, which might be associated with bulk sulfate removal as elemental sulfur. In contrast, the material without Co doping experienced low CO_2 evolution above 400°C.

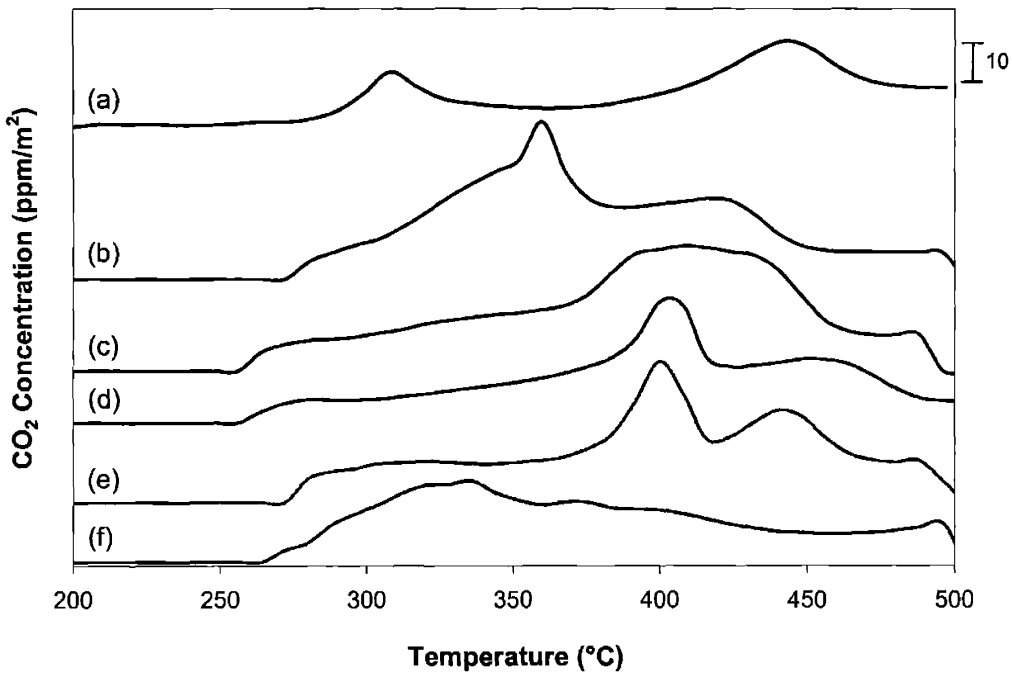

Figure 3.17 CO_2 evolution corresponding to the SO_2 TPD over 500°C-calcined (a) $CuCr_{1.9}Co_{0.1}O_4$, $CuO/CuCr_{1.9}Co_{0.1}O_4$ prepared by (b) CP, (c) PP, (d) RP and (e) IP methods, and (f) $CuO/CuCr_2O_4$. Following SO_2 adsorption at 400°C, SO_2 desorption was conducted by introducing 1% O_2 in He at 200°C, and then 2000 ppm CO in He at GHSV ~ 240,000 hr^{-1} and 200-600°C (ramp = 1°C/min).

3.3.3.2 Dynamic SO_2 Adsorption/Desorption Studies

The nanocomposites were examined in pulse studies to determine their dynamic SO_2 adsorption/desorption characteristics over multiple cycles (Figure 3.18). 20 wt% CuO/Al_2O_3 was used as a reference material. It was prepared by precipitating $Cu(OH)_2$ onto a high surface area nanocrystalline Al_2O_3 (300 m^2/g), followed by calcination at 500°C. The feed of GHSV ~ 120,000 hr^{-1} contained 300 ppm SO_2 constantly, and alternating 10-min pulses of 0.5% O_2 in He and 10-min pulses of 1% CO in He were used to mimic the oxidizing and reducing automotive exhaust streams. Prior to each pulse, a 1-min He purge was introduced.

$CuCr_{1.9}Co_{0.1}O_4$, $CuO/CuCr_2O_4$ and the four $CuO/CuCr_{1.9}Co_{0.1}O_4$ samples achieved 100% SO_2 removal over the first pulse. With the exception of the $CuO/CuCr_{1.9}Co_{0.1}O_4$ materials synthesized by the CP and IP methods, these samples all showed a sharp SO_2 desorption with the introduction of CO, followed by the SO_2 concentration falling below the constant 300 ppm feed level (Figure 3.18). This coupled

with the initial SO_2 desorption peak in the subsequent pulse suggested that the surface sulfate was decomposed to elemental sulfur by the highly active $CuCr_{1.9}Co_{0.1}O_4$ nanocrystals, and was desorbed as SO_2 when O_2 was introduced. Although the sulfur condensation was not desired, the systems operated at temperatures such that sulfur would remain in the gas phase. All these materials showed a rapid SO_2 evolution during the second to fifth pulses, with the $CuO/CuCr_{1.9}Co_{0.1}O_4$ material synthesized by the RP method achieving the fastest and greatest SO_2 desorption. The effective SO_2 desorption in all five $CuCr_2O_4$-based materials allowed for nearly 100% SO_2 removal over the second to fifth adsorption cycles.

In contrast, CuO/Al_2O_3 showed significant SO_2 uptake over the first two adsorption cycles with nearly 100% SO_2 removal over the entire 10-min pulses. However, the introduction of CO into the system resulted in a more gradual SO_2 desorption. Substantial decay in SO_2 adsorption activity was noted in subsequent cycles for this conventional adsorbent.

Average SO_2 adsorption and desorption characteristics over the first five cycles were calculated for the seven samples, correcting for SO_2 desorption that resulted from elemental sulfur (Table 3.12). CuO/Al_2O_3 achieved the highest adsorption capacity on a weight basis (29.4 mg SO_2/g adsorbent) as a result of higher support surface area. However, this was only 85% of the total SO_2 introduced (34.5 mg SO_2/g) due to incomplete SO_2 removal after the second adsorption cycle. This in large part was associated with the slow SO_2 desorption, which resulted in only 0.07 mg SO_2 desorbed/m^2 (only 70% of that adsorbed). In contrast, $CuO/CuCr_2O_4$, $CuCr_{1.9}Co_{0.1}O_4$ and the four $CuO/CuCr_{1.9}Co_{0.1}O_4$ materials removed $\geq$ 95% of the SO_2 introduced (11.5 mg/g) during their adsorption cycles. $CuO/CuCr_{1.9}Co_{0.1}O_4$ synthesized by the RP method not only showed a high adsorption capacity (0.32 mg SO_2/m^2), but also achieved excellent desorption of > 95% of that adsorbed (0.31 mg SO_2/m^2).

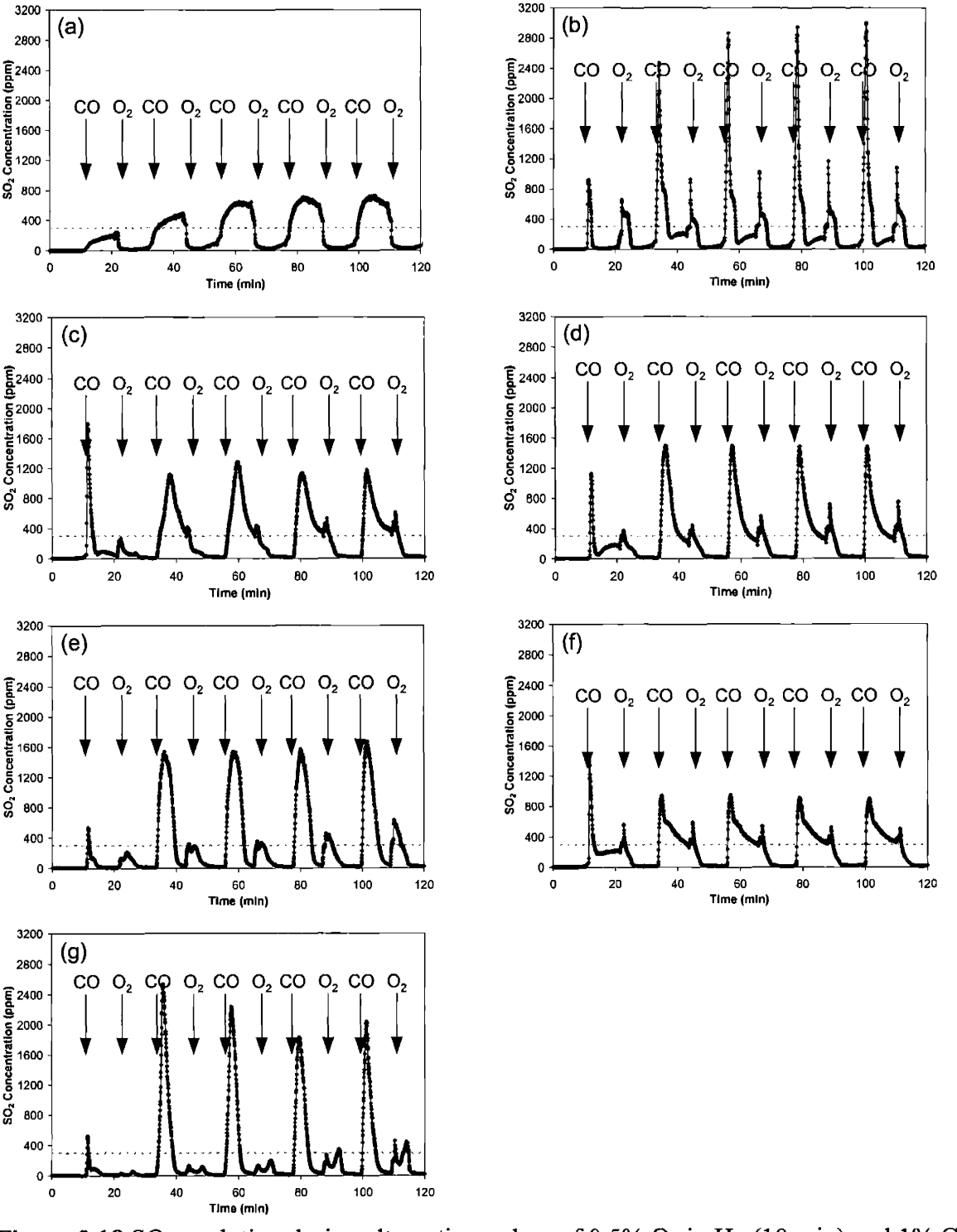

Figure 3.18 SO_2 evolution during alternating pulses of 0.5% O_2 in He (10 min) and 1% CO in He (10 min) over 500°C-calcined (a) CuO/Al_2O_3, (b) $CuCr_{1.9}Co_{0.1}O_4$, $CuO/CuCr_{1.9}Co_{0.1}O_4$ prepared by (c) CP, (d) PP, (e) RP and (f) IP methods, and (g) $CuO/CuCr_2O_4$. A constant feed of 300 ppm SO_2 (---) was introduced at GHSV ~ 120,000 hr^{-1} and 400°C. Prior to each pulse, a 1-min He purge was fed.

Table 3.12 SO_2 adsorption/desorption averaged over five cycles during alternating pulses of 0.5% O_2 in He (10 min) and 1% CO in He (10 min) over 500°C-calcined materials. A constant feed of 300 ppm SO_2 was introduced at GHSV ~ 120,000 hr^{-1} and 400°C. Prior to each pulse, a 1-min He purge was fed.

Material	SO_2 Adsorption (mg/g)	SO_2 Adsorption (mg/m^2)	SO_2 Desorption (mg/m^2)
CuO/Al_2O_3	29.4	0.10	0.07
$CuCr_{1.9}Co_{0.1}O_4$	10.9	0.44	0.37
$CuO/CuCr_{1.9}Co_{0.1}O_4$ (CP)	10.9	0.44	0.40
$CuO/CuCr_{1.9}Co_{0.1}O_4$ (PP)	10.9	0.44	0.39
$CuO/CuCr_{1.9}Co_{0.1}O_4$ (RP)	10.9	0.32	0.31
$CuO/CuCr_{1.9}Co_{0.1}O_4$ (IP)	11.0	0.44	0.35
$CuO/CuCr_2O_4$	11.0	0.32	0.25

3.4 Summary

The use of NO_x storage materials to provide pollutant control for lean-burn engines requires a material that can protect the base metal oxide NO_x adsorbent from sulfate poisoning. The conventional SO_2 adsorbent material, $Ca(OH)_2$, has a low adsorption and regeneration efficiency, and is not suitable for automotive application. Recent research has focused on CuO/Al_2O_3, which possesses both high SO_2 adsorption efficiency and regenerability. However, this SO_2 trap material requires an adsorption temperature of ~ 450°C, which is above the 400°C maximum operating temperature for NO_x storage.

Various CuO-based mixed oxides were examined as potential candidates for SO_2 adsorption. Cr_2O_3-CuO was found to promote low-temperature desorption. For this mixed oxide series, higher SO_2 adsorption capacity and regenerability were attained with increasing CuO content. In fact, the presence of a secondary CuO phase on the surface of $CuCr_2O_4$ spinel nanocrystals was important towards high sulfate incorporation, and helped to prevent SO_3 bypass that was observed over pure Cr_2O_3. The $CuCr_2O_4$ spinel was useful towards adsorbent regeneration. This could be attributed to the reduction of $CuCr_2O_4$ by CO and the subsequent solid-state reaction that promoted surface sulfate decomposition.

The effect of various dopants at the Cu and Cr sites of $CuCr_2O_4$ was examined. It was found that Co doping at the Cr site provided improved thermal stability and low-

temperature SO_2 desorption activity. The enhanced SO_2 desorption correlated well with the low-temperature CO_2 evolution, and the introduction of Co dopants might have promoted the conversion of CO to CO_2. Low-temperature regenerability of $CuCr_{2-y}Co_yO_4$ was optimized at $y = 0.1$.

Finally, CuO was introduced as a secondary phase on $CuCr_{1.9}Co_{0.1}O_4$ via four different synthesis routes to yield SO_2 traps with excellent thermal stability, SO_2 adsorption capacity and desorption characteristics. Co-precipitation of $CuCr_{1.9}Co_{0.1}O_4$ and CuO promoted the greatest amount of SO_2 desorption by the lowest temperature (360°C). Dynamic pulsing studies illustrated that $CuCr_{1.9}Co_{0.1}O_4$, $CuO/CuCr_2O_4$ and $CuO/CuCr_{1.9}Co_{0.1}O_4$ materials exhibited faster and more efficient SO_2 regenerability than CuO/Al_2O_3, although the latter has a higher surface area. Of the $CuO/CuCr_{1.9}Co_{0.1}O_4$ materials, co-precipitation of $CuCr_{1.9}Co_{0.1}O_4$ and CuO provided for superior SO_2 adsorption capacity and the greatest desorption amount over multiple adsorption/desorption cycles. Precipitation of $CuCr_{1.9}Co_{0.1}(OH)_8$ onto a pre-precipitated $Cu(OH)_2$ gave rise to the best regenerability over multiple cycles.

3.5 References

[1] Bogner, W., Kramer, M., Krutzsch, B., Pischinger, S., Voigtlander, D., Wenninger, G., Wirbeleit, F., Brogan, M. S., Brisley, R. J., Webster, D. E., *Appl. Catal. B: Environ.* **1995**, *7*, 153.

[2] Cooper, C. D., Alley, F. C., *Air Polution Control: A Design Approach*, 2nd ed., Waveland Press, Inc., Prospect Heights, **1994**.

[3] Feeley, J., Deeba, M., Farrauto, R. J., *Stud. Surf. Sci. Catal.* **1998**, *116*, 529.

[4] Mahzoul, H., Brilhac, J. F., Gilot, P., *Appl. Catal. B: Environ.* **1999**, *20*, 47.

[5] Machida, M., in *Catalysis, Vol. 15* (Ed.: Spivey, J. J.), Royal Society of Chemistry, Cambridge, **2000**, pp. 73.

[6] Engstrom, P., Amberntsson, A., Skoglundh, M., Fridell, E., Smedler, G., *Appl. Catal. B: Environ.* **1999**, *22*, L241.

[7] Adams, K. M., Cavataio, J. V., Hammerle, R. H., *Appl. Catal. B: Environ.* **1996**, *10*, 157.

[8] Corma, A., Palomares, A. E., Rey, F., *Appl. Catal. B: Environ.* **1994**, *4*, 29.

[9] Waqif, M., Saur, O., Lavalley, J. C., Wang, Y., Morrow, B. A., *Appl. Catal.* **1991**, *71*, 319.

[10] Bhattacharyya, A. A., Woltermann, G. M., Yoo, J. S., Karch, J. A., Cormier, W. E., *Ind. Eng. Chem. Res.* **1988**, *27*, 1356.

[11] Wang, J. A., Zhu, Z. L., Li, C. L., *J. Mol. Catal. A - Chem.* **1999**, *139*, 31.

[12] Macken, C., Hodnett, B. K., *Ind. Eng. Chem. Res.* **1998**, *37*, 2611.

[13] Kiel, J. H. A., Prins, W., Vanswaaij, W. P. M., *Appl. Catal. B: Environ.* **1992**, *1*, 13.

[14] Lowell, P. S., Schwitzgebel, K., Parsons, T. B., Sladek, K. J., *Ind. Eng. Chem. Proc. Des. Develop.* **1971**, *10*, 384.

[15] Jacob, K. T., Kale, G. M., Iyengar, G. N. K., *J. Mater. Sci.* **1986**, *21*, 2753.

[16] Kim, G., *Ind. Eng. Chem. Prod. Res. Develop.* **1982**, *21*, 267.

[17] Murthy, K., Ghose, J., *J. Catal.* **1994**, *147*, 171.

[18] Wang, J.-A., Chen, L.-F., Li, C.-L., *React. Kinet. Catal. Lett.* **1998**, *64*, 73.

[19] Ghose, J., Murthy, K., *J. Catal.* **1996**, *162*, 359.

4 – Synthesis and Stabilization of Zinc Oxide Nanocrystals for H_2S Absorption

4.1 Introduction

Converting heavy hydrocarbons into H_2 as feed for fuel cell systems requires fuel processing such as catalytic cracking and steam reforming. The sulfur present in the hydrocarbon feedstream is frequently converted to H_2S during fuel processing. H_2S has to be carefully removed since it can poison the catalyst, membrane and fuel cell materials downstream. Various metal oxides have been examined for H_2S removal at 300-500°C [1, 2]. ZnO and Fe_2O_3 have been used commercially as H_2S absorbents [3]. Although Fe_2O_3 is effective at absorbing H_2S at 300-600°C, the reduction of Fe_2O_3 to FeO not only lowers the absorbent efficiency, but may also introduce a sulfur bypass in the form of SO_2 [4]. In contrast, ZnO is highly efficient at H_2S removal over a wider temperature range due to its rapid surface kinetics and oxygen-sulfur counter-diffusion.

The reaction between H_2S and ZnO has been well-characterized and falls into three regimes: (i) 300-500°C where absorption is diffusion-controlled, (i) 500-600°C where both reaction and diffusion play an important role, and (iii) above 600°C where absorption is kinetically limited [5, 6]. Since diffusion is rate-limiting between 300°C and 500°C, the absorbent utilization would be maximized by using ultrafine particles for a confined diffusion depth. However, the commercially available ZnO has coarse grain sizes, and special synthesis for nanocrystalline ZnO has to be developed. The low melting point of ZnO makes it highly challenging to prevent grain growth above 350°C [7].

Previous studies [8-10] have focused on improving ZnO stability and absorption by co-precipitating ZnO with secondary oxides such as TiO_2 and ZrO_2. The presence of the secondary oxides not only provided microstructural stability, but also prevented ZnO reduction at sulfation temperatures above 600°C, thus improving H_2S absorption performance. Although the thermal stability achieved provided for greater H_2S absorption capacity at elevated temperatures, the low surface area of these mixed oxides offered limited improvement over the conventional ZnO absorbent at temperatures $\leq$ 500°C. Additionally, the use of a large amount of inert secondary oxides was undesirable especially for mobile applications since it would reduce the overall absorption efficiency on a weight or volume basis.

Our research focuses on the synthesis of ZnO nanoparticles through wet-chemical processing. To provide for thermal stability and regenerability, secondary metal oxides are coated onto the ZnO nanoparticles to suppress grain growth. With the use of a nanocrystalline material, the distance for oxygen-sulfur counter-diffusion is greatly reduced, increasing substantially the overall material utilization. Since regeneration rate is dependent on both sulfate decomposition and oxygen-sulfur diffusion, the regeneration temperature and/or time can potentially be decreased through the use of nanoparticles. By optimizing the nanocrystalline ZnO synthesis, as well as the composition and loading of the secondary oxide, ZnO-based nanocomposites ideal for regenerable H_2S absorption can be achieved.

4.2 Experimental

4.2.1 Materials Synthesis

ZnO was synthesized by chemical precipitation of $Zn(NO_3)_2 \cdot 6H_2O$ (Aldrich, 98%) using various bases (tetraethyl ammonium hydroxide (Alfa Aesar, 35 wt% in water) and ammonium carbonate (Alfa Aesar)). Typical precipitation involved the addition of 0.1 M zinc nitrate solution dropwise to a 0.1 M base solution under vigorous stirring. The precipitate was allowed to age in solution for 18 hours before recovery by centrifuging at 3000 rpm for over 10 min. The supernatant was decanted, and the recovered powders were washed three times with ethanol. The materials were then dried at 25°C, ground by mortar and pestle to break up loose agglomerates prior to calcination between 200°C and 700°C.

The ZnO nanoparticles were subject to oxide coating with metal alkoxide precursors (titanium isopropoxide (Alfa Aesar, 98 wt% in propanol), zirconium n-propoxide (Alfa Aesar, 70 wt% in propanol) and vanadium triisopropoxide (Aldrich, 95-99 wt% in propanol)). The nanoparticles were first introduced to a hexane solution and sonicated to ensure good dispersion. A hexane solution containing metal alkoxide precursor was then added to the ZnO suspension under vigorous stirring. The mixture was then heated to 60°C and aged overnight. The coated particles were recovered by centrifuging at 3000 rpm for 10 min. The supernatant was decanted, and the recovered powder was washed sequentially with hexane, isopropanol and hexane. The materials

were then dried at 25°C, ground by mortar and pestle to break up loose agglomerates prior to calcination between 500°C and 900°C.

4.2.2 Materials Characterization

The surface area of the ZnO powders was determined from nitrogen adsorption analysis using the five-point BET (Brunauer-Emmett-Teller) method with a Micromeritics ASAP 2000 gas adsorption analyzer. Phase identification was performed by powder X-ray diffraction (XRD) using a Siemens D5000 θ-θ diffractometer (45 kV, 40 mA, Cu-K_α). Grain size was obtained by peak broadening analysis of the ZnO <100> reflection ($2\theta = 31.772°$) using Scherrer's method and corrected for instrumental line broadening. Transmission electron microscopy (TEM) and high-resolution transmission electron microscopy (HR-TEM) were performed on JEOL 2000 and JEOL 2010 microscopes (200 kV), respectively. Photoacuoustic Fourier-transform infrared (PA-FTIR) spectra were obtained with a Bio-Rad FTS 60A spectrometer using a model 200 photoacoustic cell. X-ray photoelectron spectroscopy (XPS) was used in surface analysis; a Kratos AXIS XPS was employed with an Al source (1486.6 eV). Chemical analysis was performed by Desert Analytics using a Jarrel-Ash 61ICP (Tucsan, AZ).

4.2.3 Absorption and Kinetic Analyses

A vertical tubular flow reactor was used to perform absorption and reaction analyses on both nanocrystalline and conventional ZnO materials (Figure 4.1). The sample (50 mg) was supported on a bed of quartz wool in a ¼"-O.D. quartz reactor tube. A K-type thermocouple (Omega) protected by a quartz sheath was used in conjunction with a vertically mounted Lindberg Blue M tube furnace and an Omega 2040 temperature controller to maintain absorption temperature within 2°C of the desired temperature (300-500°C). Sierra mass flow controllers (MFC) were used to control the feedstream composition and flow rate; a constant space velocity of ~ 30,000 hr^{-1} was maintained for all studies. The effluent stream was analyzed by a Hewlett-Packard 6890 gas chromatograph (GC) equipped with a thermal conductivity detector (TCD), a Chromosil 310 column to separate and quantify H_2S, COS and SO_2, and a 5-ml sample loop. Regeneration analysis was performed at 650°C in air at a space velocity of ~ 30,000 hr^{-1} followed by a helium purge. Prior to analysis, each powder sample was compacted at

175 lb/in^2, and then crushed and sieved (60 mesh) to ensure consistent interparticle diffusion and bed volume.

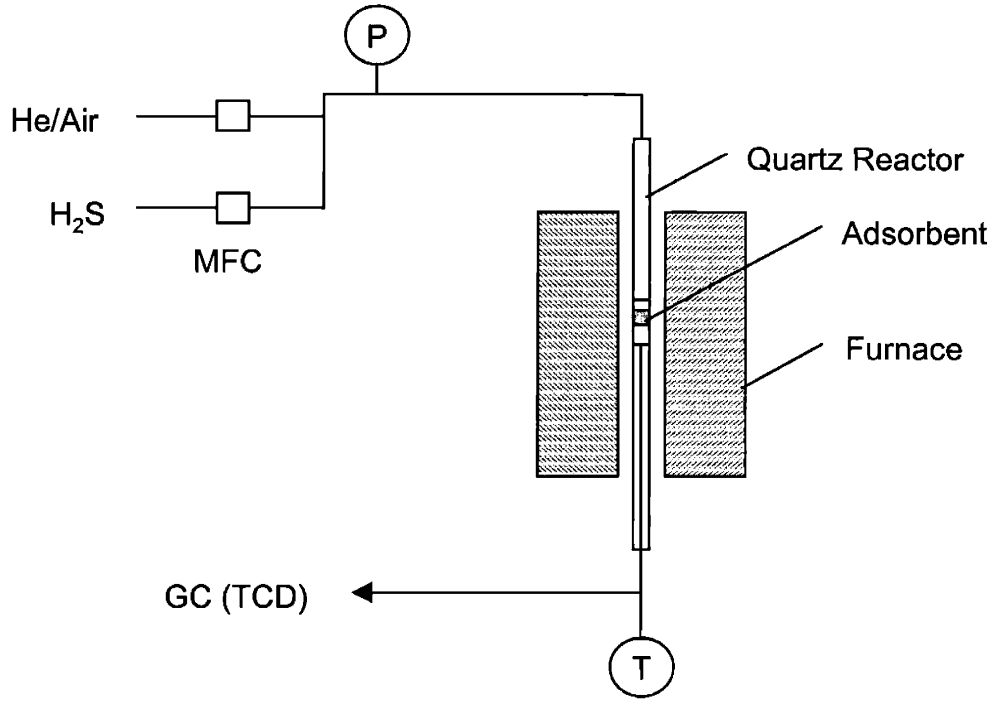

Figure 4.1 Schematic of reactor setup.

Analysis of weight change as a function of feedstream composition, temperature and ZnO grain size was performed with a Perkin Elmer System 7HT thermal gravimetric analyzer (TGA). ZnO powders were compacted and sieved as in the absorption studies. Samples were pretreated at the desired operating temperature (between 300°C and 500°C) in He prior to the introduction of H_2S. A quartz sample pan was used to avoid errors caused by any H_2S adsorption. A gas flow (500 sccm) of 0.4% H_2S in He was maintained to limit the effects of localized concentration gradient.

4.3 Results and Discussion

4.3.1 Synthesis of Nanocrystalline ZnO

ZnO synthesis has received much attention for H_2S absorption as well as electronic and photoactive applications. The two most common wet-chemical synthesis routes involve the precipitation of zinc hydroxide or zinc hydroxyl carbonate species, followed by calcination to achieve ZnO [11-17].

4.3.1.1 Effect of Base

ZnOH and $ZnCO_3$ were synthesized by chemical precipitation of zinc nitrate with tetraethyl ammonium hydroxide (TEAH) and ammonium carbonate ($(NH_4)_2CO_3$), respectively (Figure 4.2). There was a significant difference in material properties from the two synthesis routes. TEAH synthesis produced ZnO with a surface area of 15 m^2/g and a grain size of 28 nm at 300°C. The ZnO sample underwent sintering upon calcination to 500°C, resulting in a surface area of 7 m^2/g and a grain size of 33 nm. Although the ZnOH precipitate calcined to 300°C gave ZnO with significantly improved surface area over commercially available ZnO (Aldrich, surface area = 7 m^2/g, particle size ~ 130 nm), the $ZnCO_3$ produced by $(NH_4)_2CO_3$ synthesis gave rise to ZnO with three times higher surface area (47 m^2/g) and a finer grain size of 21 nm at 300°C. However, the ZnO from the $(NH_4)_2CO_3$ route also experienced a significant loss in surface area to 13 m^2/g at 500°C with a concomitant increase in grain size to 45 nm.

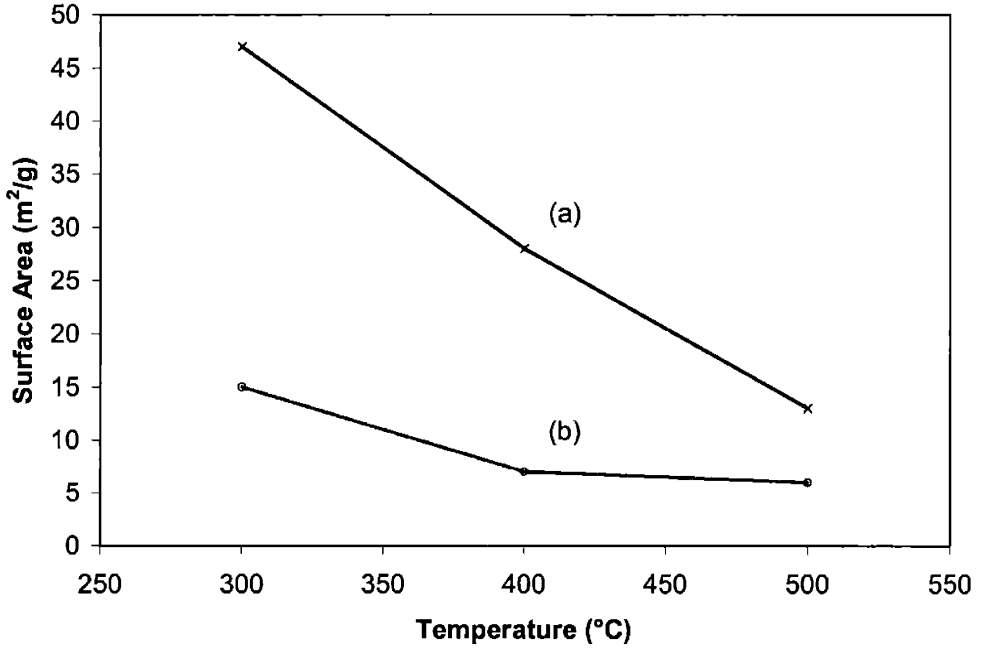

Figure 4.2 BET surface area of ZnO synthesized using (a) $(NH_4)_2CO_3$ and (b) TEAH as the base.

Percent agglomeration was calculated by dividing the difference between the geometric surface area and the BET surface area of ZnO by the geometric surface area

(Table 4.1). The geometric surface area was determined from the XRD crystallite size and the density of pure ZnO (5.41 g/cm^3), assuming spherical grains [18]. Although the grain sizes (and therefore the geometric surface areas) of ZnO materials derived by both routes were quite similar, there was a significant difference in their BET surface areas. The carbonate synthesis produced nanocrystalline particles with a much lower level of agglomeration than the hydroxide route.

Table 4.1 Physical characteristics of 300°C-calcined ZnO prepared by carbonate and hydroxide synthesis routes.

Base	<101> Crystallite Size (nm)	BET Surface Area (m^2/g)	Geometric Surface Area (m^2/g)	Agglomeration (%)
$(NH_4)_2CO_3$	21	47	53	11
TEAH	28	15	40	62

The extent of agglomeration as well as particle morphology were illustrated by TEM (Figure 4.3). The carbonate precipitate was in the form of filaments with uniform shape and size (20-50 nm in width and 200-600 nm in length). Upon calcination, the carbonate precipitate was crystallized as discrete ZnO particles with a narrow particle size distribution on the order of their XRD grain size. In contrast, the hydroxide precipitate exhibited various morphologies, including spider-like structures and segregated amorphous spheroidal particles. The micron-sized agglomerates of ZnOH precipitate led to heavily aggregated ZnO grains upon calcination to 300°C, corresponding to a material with a low BET surface area.

Hydroxide synthesis of ZnO with various morphologies has been reported previously in literature. By varying the temperature, base and solution concentration, researchers have been able to control the grain size and morphology, yielding ZnO crystallites of < 10 nm [12, 13, 16, 19]. However, unless a multi-step synthesis technique was employed, heavily aggregated ZnO grains would result, producing micron-sized particles with ~ 50% agglomeration [19, 20]. This confirmed that ultrafine, discrete ZnO nanocrystals could not be achieved via the hydroxide route. In contrast, our carbonate synthesis would give the desired ZnO nanoparticles with only a low degree of agglomeration, which should lead to better resistance against sintering and grain growth.

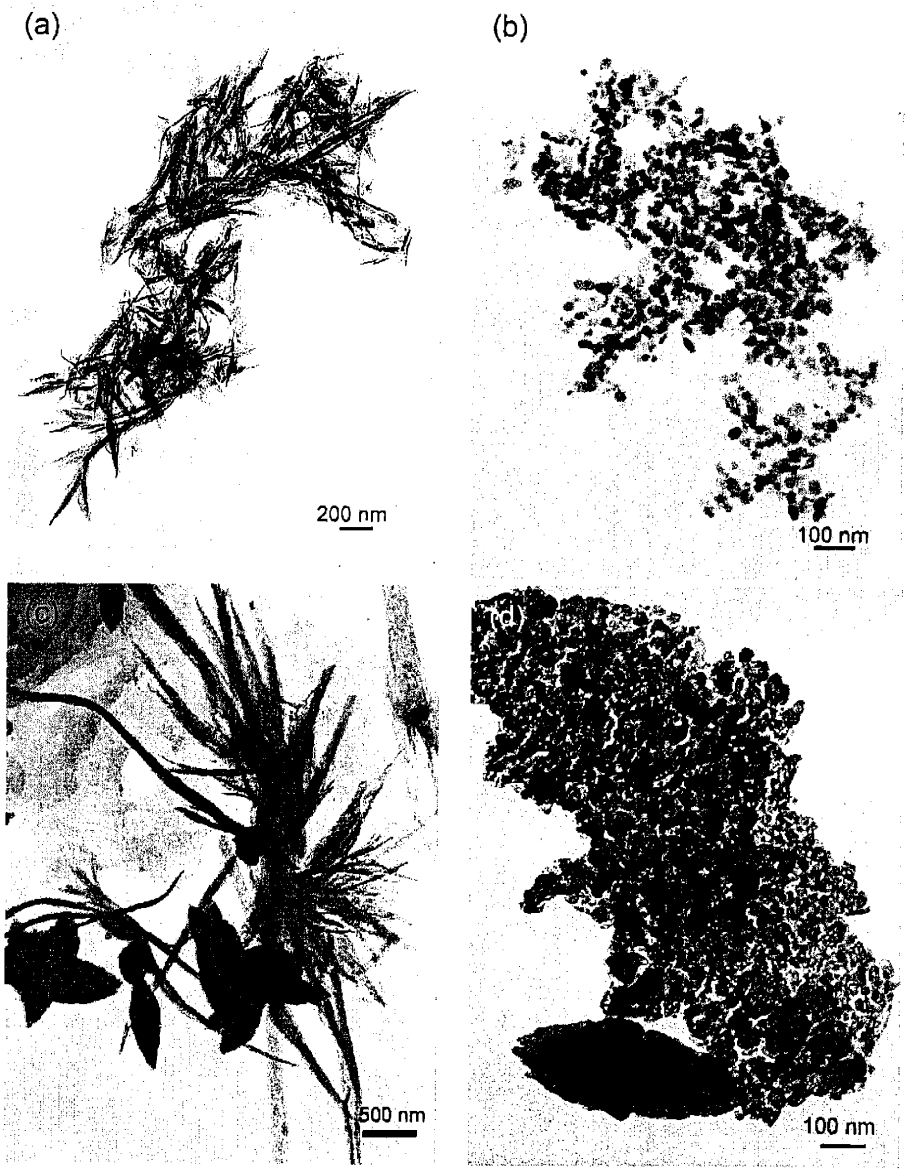

Figure 4.3 TEM micrographs of (a) $ZnCO_3$ precipitate, (b) 300°C-calcined ZnO nanoparticles by $(NH_4)_2CO_3$ synthesis, (c) ZnOH precipitate, and (d) 300°C-calcined ZnO nanoparticles by TEAH synthesis.

4.3.1.2 Effect of $Zn(NO_3)_2 \cdot 6H_2O$ Precursor Concentration

Synthesis parameters such as precursor concentration, aging time and pH can have a significant effect on the microstructure of the material derived. For the synthesis of ZnO nanoparticles, it was found that $Zn(NO_3)_2 \cdot 6H_2O$ concentration had the most significant impact (Figure 4.4). An increase in surface area from 40 m^2/g to 80 m^2/g with a concomitant reduction in grain size from 20 nm to 12 nm was achieved by reducing the $Zn(NO_3)_2 \cdot 6H_2O$ precursor concentration from 0.20 M to 0.01 M in the $(NH_4)_2CO_3$

synthesis. This effect was not unexpected since a lower precursor concentration would favor crystal nucleation over growth, as well as reduce particle aggregation [21].

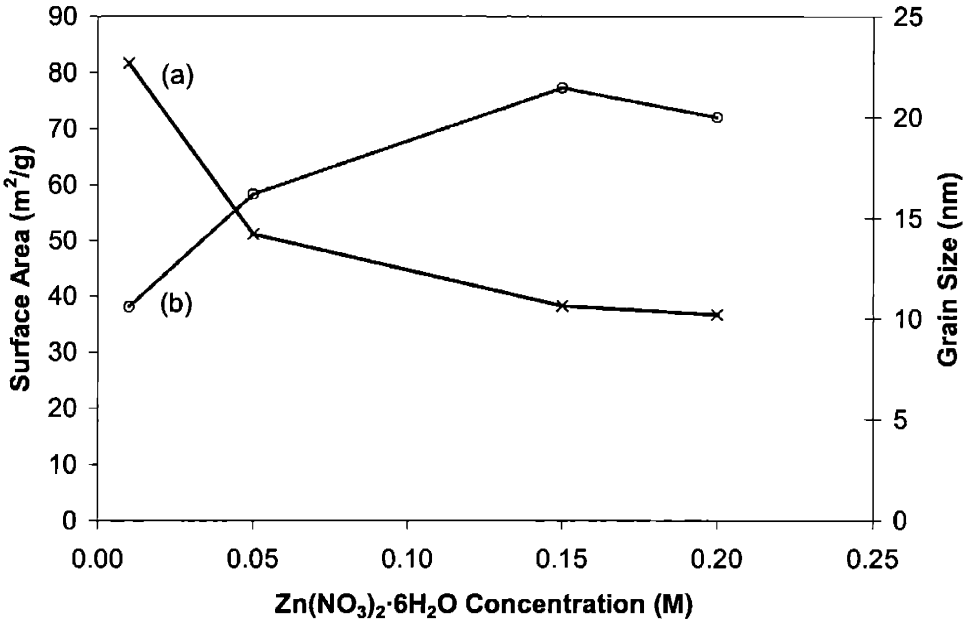

Figure 4.4 Effect of $Zn(NO_3)_2 \cdot 6H_2O$ concentration in the $(NH_4)_2CO_3$ synthesis on the (a) BET surface area and (b) XRD grain size of 300°C-calcined ZnO.

4.3.1.3 Effect of Calcination Temperature

Calcination above 350°C led to significant grain growth of the ZnO nanoparticles. Thus, to achieve ultrafine ZnO nanoparticles, the $ZnCO_3$ precipitate should be calcined at low temperatures. For the conventional $ZnCO_3$ particles, the decomposition temperature was ~ 300°C, but the as-precipitated zinc hydroxyl carbonate particles could be decomposed at temperatures below 300°C [22].

Temperature-programmed decomposition of the as-precipitated particles from $(NH_4)_2CO_3$ synthesis showed that $ZnCO_3$ underwent a two-stage transition to ZnO (Figure 4.5). The first crystallization occurred at ~ 200°C and was associated with the formation of zinc hydroxyl carbonate. The second crystallization step was accompanied by significant weight loss from the decomposition of zinc hydroxyl carbonate at 200-250°C. Following ZnO crystallization, ~ 2% weight loss was noted between 250°C and 500°C due to the removal of residual surface carbonate species. These carbonate species

were found not only on the as-calcined powders, but also on all forms of ZnO that have been exposed to CO- or CO_2-containing gas streams [23, 24].

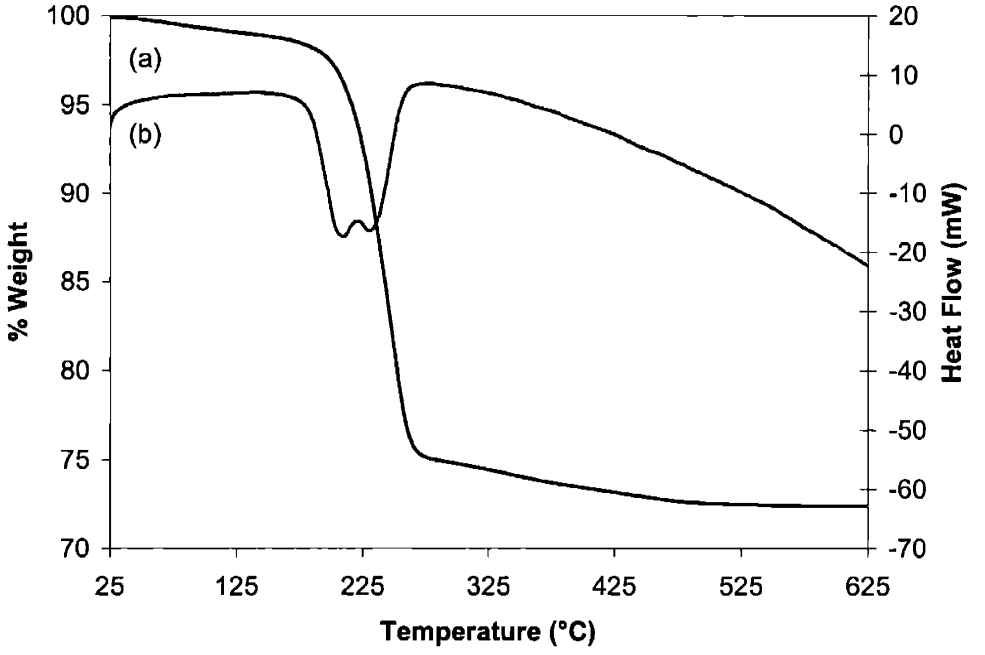

Figure 4.5 (a) Weight loss and (b) heat flow associated with the thermal decomposition of the $ZnCO_3$ precipitate in air (ramp = 10°C/min).

Although the ZnO crystallization was not complete until 250°C, both the initial zinc hydroxyl carbonate crystallization and the weight loss associated with carbonate decomposition began before 200°C. It was therefore possible to decompose the carbonate at 200°C by adjusting the calcination time and atmosphere. XRD patterns of the $ZnCO_3$ precipitate calcined at 200°C for 1 hour, 4 hours and 6 hours showed the formation of the ZnO crystalline phase (Figure 4.6).

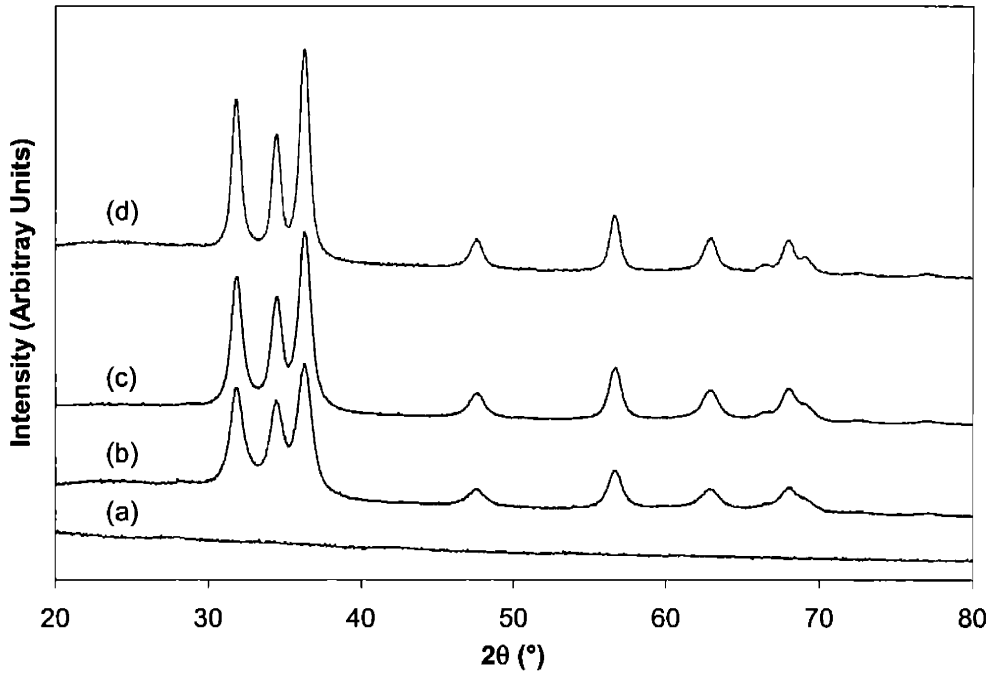

Figure 4.6 XRD patterns of (a) uncalcined $ZnCO_3$ precipitate, and $ZnCO_3$ calcined at 200°C in air for (b) 1 hour, (c) 4 hours and (d) 6 hours.

PA-FTIR spectrum of the uncalcined $ZnCO_3$ precipitate consisted of intense bands at 3000-3600 cm^{-1} due to hydrogen-bonded H_2O and hydroxyl groups [23], a doublet at 1200-1600 cm^{-1} from carbonate species [23], and multiple peaks below 1200 cm^{-1} due to bidentate carbonate species coordinated to Zn ions [24]. Upon calcination at 200°C for 1 hour, these peaks became greatly reduced in intensity while the ZnO phonon bands emerged below 1200 cm^{-1}. Calcination for 6 hours resulted in complete decomposition of $ZnCO_3$ and further growth of the ZnO phonon bands, while bands at 1200-1600 cm^{-1} emerged due to the adsorption of CO and CO_2 species on our high surface area material [23]. The $ZnCO_3$ precipitate calcined to 200°C for 1 hour, 4 hours and 6 hours in air retained 78%, 75% and 73% of the original weight, respectively. After 6 hours of calcination at 200°C, the total weight loss was similar to that seen in Figure 4.5 following heat treatment at 625°C that corresponded to complete carbonate decomposition.

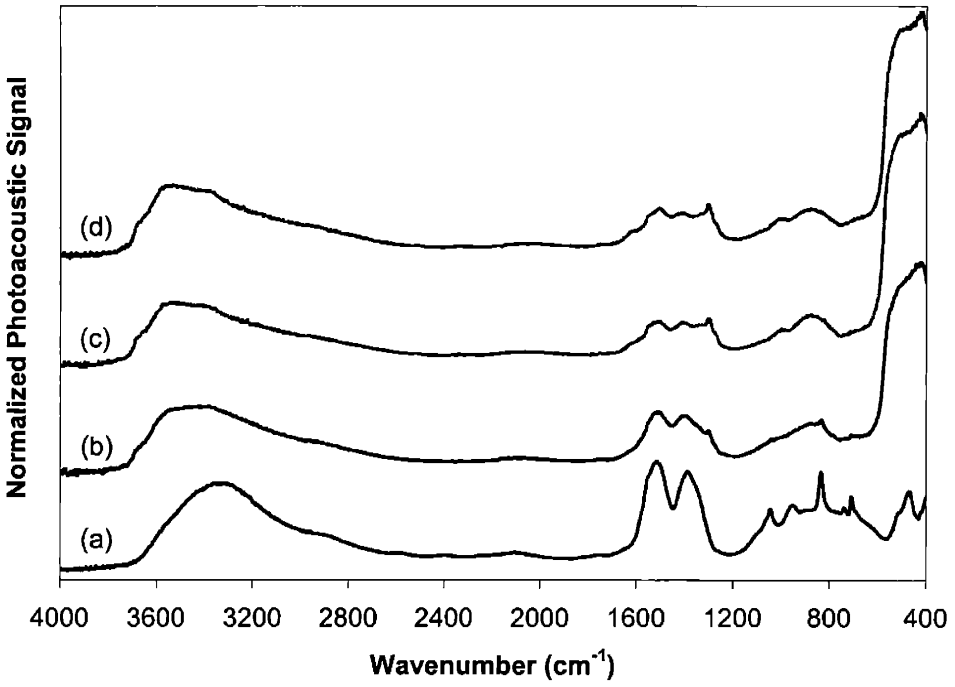

Figure 4.7 PA-FTIR spectra of (a) uncalcined $ZnCO_3$ precipitate, and $ZnCO_3$ calcined at 200°C in air for (b) 1 hour, (c) 4 hours and (d) 6 hours.

Calcination atmosphere also had a profound effect on the final ZnO characteristics (Table 4.2). The presence of water and oxygen during the calcination process promoted sintering. 3% water in N_2 caused a significant loss in surface area and grain growth to 25 nm. The highest surface area of 82 m^2/g and an ultrafine grain size of 11 nm were achieved by calcining $ZnCO_3$ precipitate under vacuum (Table 4.2). Through optimized synthesis by the $(NH_3)_2CO_3$ route using a low nitrate precursor concentration (0.01 M) and 200°C calcination under vacuum, we have achieved ZnO nanoparticles with a BET surface area as high as 152 m^2/g and a grain size as fine as 6 nm.

Table 4.2 Effect of calcination atmosphere on the characteristics of 200°C-calcined ZnO.

Calcination Atmosphere	BET Surface Area (m^2/g)	<101> Grain Size (nm)
Vacuum	82	11
Nitrogen	70	11
Oxygen	58	15
3% Water in Nitrogen	34	25

4.3.2 Stabilization of ZnO Nanocrystals through Secondary Oxide Coating

Although a grain size of < 10 nm could be achieved for ZnO by nanostructure processing, significant grain growth would occur upon calcining this simple metal oxide of low melting point to 500°C. Previous studies on the sintering of ZnO have shown that surface areas in excess of 30 m^2/g would be reduced to 15 m^2/g upon thermal treatment at 500°C for 6 hours [7].

To prevent sintering, it is critical to avoid close contact between grains, which would give rise to a gradual necking between grains, causing grain growth and loss of surface area. By coating a secondary metal oxide of greater thermal stability onto the ZnO grains, close contact and necking between ZnO grains could be prevented, thereby suppressing grain growth during heat treatment. TiO_2 and ZrO_2 were examined as secondary oxides in this work since their co-precipitation with ZnO has been shown to improve the ZnO's stability and H_2S absorption activity [8, 9]. V_2O_5 was also of interest since it could react with H_2S and SO_2, and might promote H_2S absorption and SO_2 desorption processes [1, 25].

Ideally, the 'coating' would constitute less than a monolayer of secondary oxide to provide stability for ZnO, while minimizing the inert secondary phase and providing access to the ZnO particle. Gao *et al.* have shown that the presence of ~ 2.6, ~ 4.0 and ~ 2.2 atoms/nm^2 represented a monolayer coverage of V_2O_5, TiO_2 and ZrO_2 on a silica support [26-28]. Assuming similar characteristics for dispersion on ZnO, 4-5 wt% V_2O_5, 5-7 wt% TiO_2 and 4.5-6 wt% ZrO_2 should be introduced onto ZnO particles of 100-130 m^2/g to achieve less than a monolayer coverage of these secondary oxides.

Ocaña *et al.* have reported the introduction of TiO_2 onto micron-sized ZnO particles using an ethanol solution containing titanium butoxide and water to give a 20 nm-thick coating [29]. However, the introduction of water provided for the hydrolysis/condensation of discrete TiO_2 particles besides TiO_2 deposition on ZnO particles. To prevent the precipitation of a segregated secondary phase in this study, a hydrophobic hexane solution was used for the metal alkoxide precursor, which would then only undergo hydrolysis and condensation with the surface hydroxyl groups of ZnO particles.

4.3.2.1 Effect of Coating Composition

Titanium, vanadium and zirconium alkoxides were introduced onto ZnO nanoparticles (130 m^2/g, 7 nm) to give ~ 7 wt% secondary oxide loading (Figures 4.8 and 4.9). Excellent surface area was retained when these secondary oxide-coated ZnO nanoparticles were calcined to 500°C. For example, TiO_2-coated ZnO had a surface area of 88 m^2/g and a grain size of 9 nm, whereas the uncoated ZnO nanoparticles had a surface area of only 14 m^2/g and a much larger grain size of 45 nm. At 700°C, TiO_2- and ZrO_2-coated ZnO nanoparticles achieved surface areas of 48 and 31 m^2/g and grain sizes of 17 and 24 nm, respectively. In contrast, V_2O_5-coated ZnO experienced significant reduction in surface area to 10 m^2/g at 700°C due to solid-state reaction between the V_2O_5 coating and ZnO particles that formed a $Zn_3(VO_4)_2$ phase (Figure 4.10(c)). Although it showed a similarly low surface area, the V_2O_5-coated ZnO still provided better stability against grain growth compared to the uncoated ZnO, suggesting that its final microstructure at 700°C consisted of a highly agglomerated network of ZnO grains separated by $Zn_3(VO_4)_2$. ZrO_2-coated ZnO also showed evidence of a secondary ZrO_2 phase with a grain size of < 5 nm at 700°C (Figure 4.10(b)). No secondary phase was observed in TiO_2-coated ZnO until 900°C when $ZnTiO_3$ was formed. Despite the secondary phase formation, the ZrO_2- and TiO_2-coated materials still maintained ZnO grain sizes of < 100 nm at 900°C, with the former retaining an impressive surface area of 12 m^2/g.

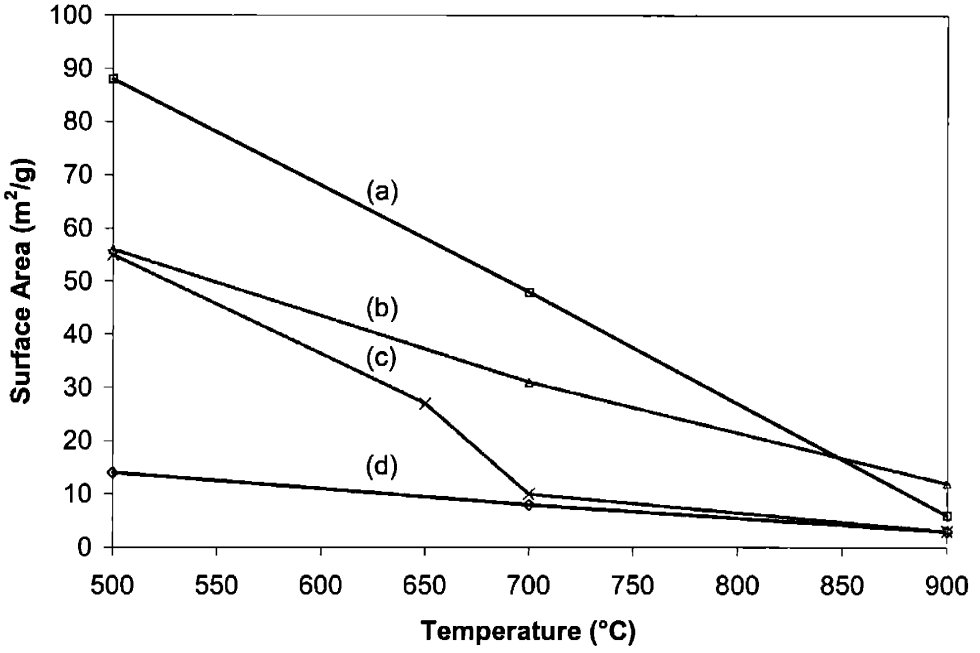

Figure 4.8 BET surface area of (a) TiO_2-, (b) ZrO_2- and (c) V_2O_5-coated ZnO nanoparticles, and (d) uncoated ZnO nanoparticles calcined to 500-900°C.

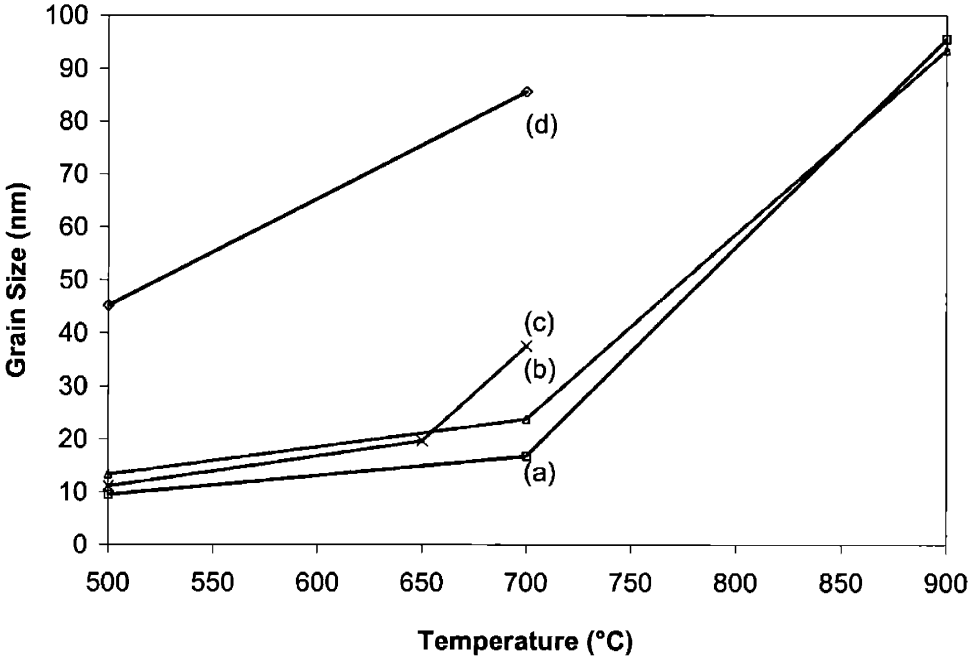

Figure 4.9 XRD grain size of (a) TiO_2-, (b) ZrO_2- and (c) V_2O_5-coated ZnO nanoparticles, and (d) uncoated ZnO nanoparticles calcined to 500-900°C.

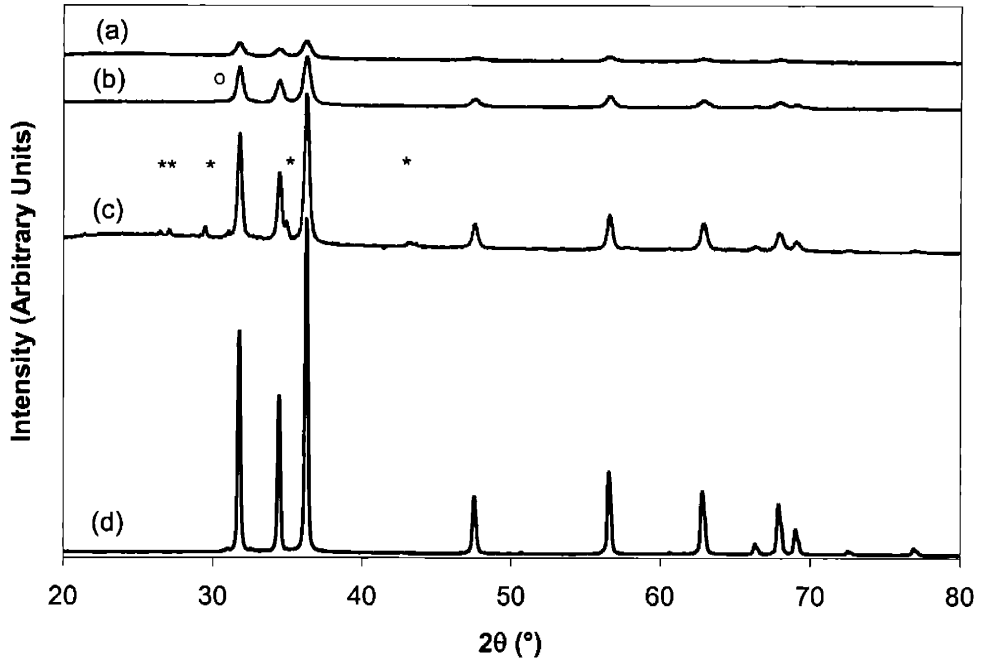

Figure 4.10 XRD patterns of (a) TiO_2-, (b) ZrO_2- and (c) V_2O_5-coated ZnO nanoparticles, and (d) uncoated ZnO nanoparticles calcined to 700°C. Peaks corresponding to secondary phases are denoted: (o) ZrO_2 and (*) $Zn_3(VO_4)_2$.

TEM showed nanocrystalline ZnO to have a broad particle size distribution of 10-100 nm at 500°C and 20-300 nm at 700°C (Figure 4.11). In contrast, the three coated ZnO materials achieved a narrowly distributed particle size of < 20 nm at 500°C, confirming the stabilizing effect of the secondary metal oxide. Upon calcination to 700°C, TiO_2-coated ZnO still maintained an ultrafine microstructure with particles of < 20 nm. ZrO_2-coated ZnO experienced a broadening of particle size distribution (10-50 nm) at 700°C, with an increase in average particle size to ~ 25 nm. The particle size distribution of 10-75 nm for V_2O_5-coated ZnO calcined to 700°C was broader than the other two coated ZnO materials. Agglomeration in the V_2O_5-coated ZnO was more significant than that in the other coated ZnO materials at both 500°C and 700°C.

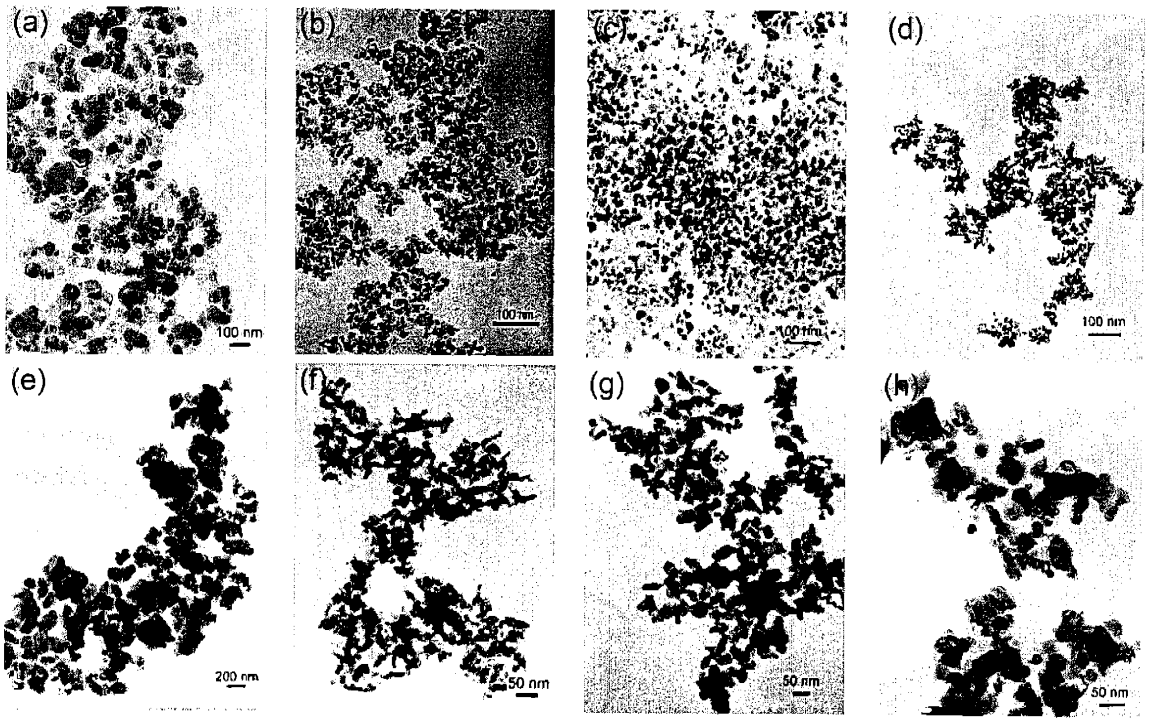

Figure 4.11 TEM micrographs of (a,e) nanocrystalline ZnO, (b,f) TiO_2-, (c,g) ZrO_2- and (d,h) V_2O_5-coated ZnO nanoparticles calcined to 500°C (a-d) and 700°C (e-h).

4.3.2.2 Surface Characterization of the Coated ZnO Nanoparticles

The improved thermal stability indicated that effective coating of secondary oxides has been successfully achieved on ZnO nanoparticles. To gain further insight into the dispersion of the secondary oxides, surface analyses were performed. For uniformly distributed compositions, the weight ratio of Zn to the secondary metal measured via chemical analysis (ICP) and XPS should be the same. In the case of a surface coverage or coating of secondary metal oxide on ZnO, the weight ratio of Zn to the secondary metal would be lower when analyzed by XPS since this characterization technique is surface-sensitive. This was shown to be the case for both TiO_2- and ZrO_2-coated ZnO nanoparticles with XPS weight ratios being lower by 31% and 25%, respectively (Table 4.3). The V_2O_5-coated ZnO material, however, showed less variation between the two characterization methods, likely due to $Zn_3(VO_4)_2$ phase formation at 700°C.

Table 4.3 Weight ratios of Zn to secondary metals analyzed by ICP and XPS for nominally 9 wt% TiO_2-, ZrO_2- and V_2O_5-coated ZnO nanoparticles calcined to 500°C.

Secondary Metal (M)	ICP Zn/M Ratio	XPS Zn/M Ratio
Ti	14.0	9.7
Zr	11.3	8.4
V	13.7	15.2

The 2p electrons of Ti of TiO_2-coated ZnO nanoparticles have binding energies of 458.75 eV, 458.68 eV and 458.70 eV after calcination at 500°C, 700°C and 900°C, respectively (Figure 4.12). This matched well with the TiO_2 binding energy of 458.79 eV, and was significantly different from the $ZnTiO_3$ binding energy of 458.55 eV. The similarity in XPS peak position as pure TiO_2, the surface Ti enrichment in XPS analysis, and the absence of TiO_2 XRD peaks even at 900°C strongly suggested that the TiO_2-coated ZnO nanoparticles consisted of an ultrahigh dispersion of TiO_2 on the surface of ZnO nanoparticles.

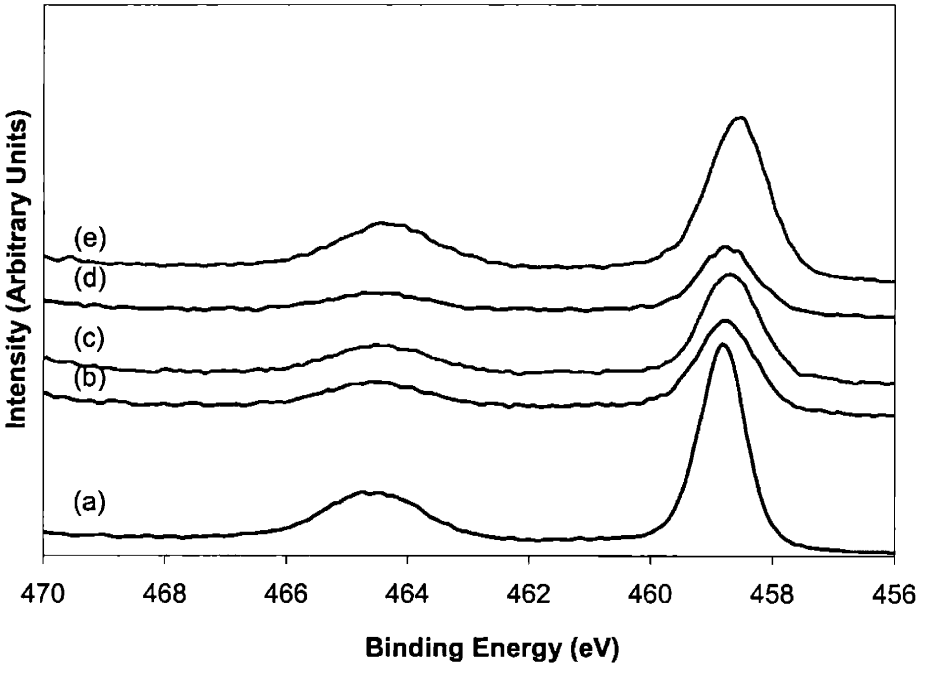

Figure 4.12 XPS spectra of (a) conventional TiO_2, TiO_2-coated ZnO nanoparticles calcined at (b) 500°C, (c) 700°C and (d) 900°C, and (e) conventional $ZnTiO_3$.

TiO_2-, ZrO_2- and V_2O_5-coated ZnO materials were shown with EDS to contain 7 wt%, 15 wt% and 4 wt% secondary metal oxide, respectively (Figure 4.13). HRTEM studies illustrated that the ZrO_2-coated ZnO material consisted of phase segregated ZrO_2 in the form of an amorphous network around ZnO nanoparticles. Separate ZrO_2 nanocrystals of < 5 nm were also noted. No lattice defects were observed in the ZnO nanoparticles; random sampling of the lattice spacing showed a repeat distance of 2.6 Å, which was consistent with the <002> plane of the ZnO lattice (d_{002} = 2.603 Å). This further confirmed that the secondary metals were present as metal oxides on the ZnO nanoparticle surface instead of being incorporated into the ZnO crystals.

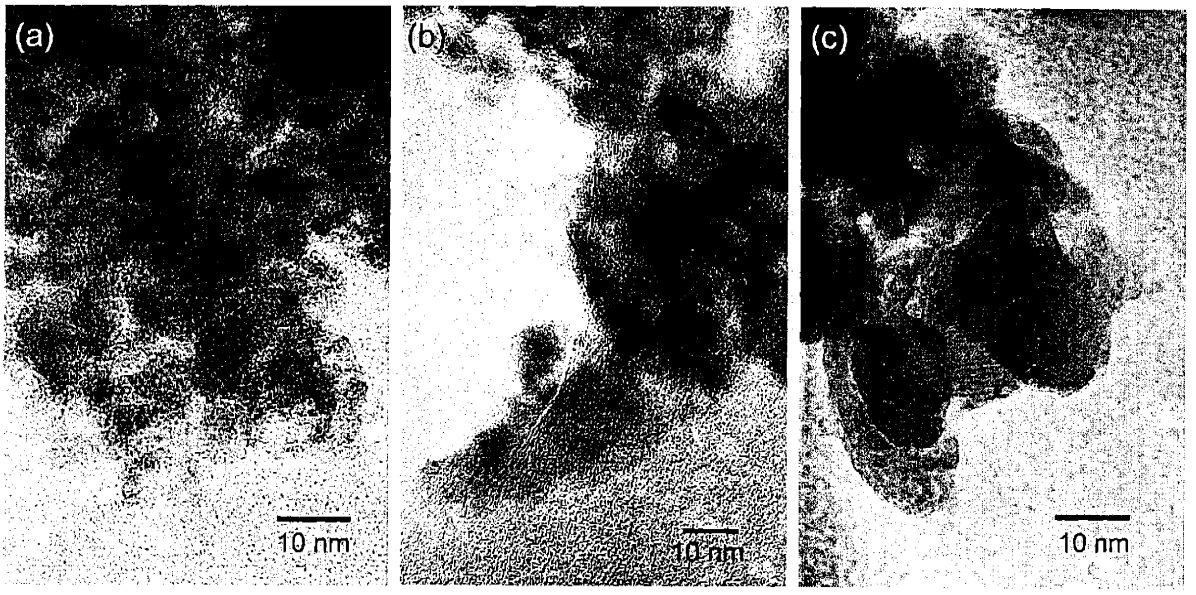

Figure 4.13 HR-TEM micrographs of (a) TiO_2- and (b) ZrO_2-coated ZnO nanoparticles calcined to 700°C, and (c) V_2O_5-coated ZnO nanoparticles calcined to 500°C.

4.3.2.3 Effect of ZnO Pretreatment on Secondary Oxide Loading

Deposition of a controlled amount of secondary metal oxide on the ZnO nanoparticle surface was found to be unrelated to the metal alkoxide concentration, coating temperature or wash conditions. The secondary oxide coating was supposed to have developed from the reaction of the metal alkoxide precursor with the active surface hydroxyl groups present on the ZnO nanoparticles. Thus, it was thought that the secondary oxide loading might be controlled by pretreating the ZnO nanoparticles (106 m^2/g, 12 nm) under a H_2O-containing He atmosphere. A fixed alkoxide concentration was used such that a maximum of 25 wt% secondary oxide could be introduced onto the

ZnO nanoparticles. It was found that the loading of TiO_2 and ZrO_2 coatings could be increased controllably from 3.0 to 5.5 wt% and from 2.5 to 7.3 wt%, respectively, by pretreating the ZnO nanoparticles in atmospheres containing increasing H_2O contents at 25°C (Figure 4.14). Further investigation on TiO_2-coated ZnO showed that pretreatment of ZnO in vacuum at 25°C and 100°C led to lower TiO_2 loadings of 2.5 and 2.2 wt%, respectively. Thus, free water was not essential for metal alkoxide to adsorb and react with the ZnO nanoparticle surface, rather, the ZnO's surface hydroxyl content was critical for controlling secondary oxide loading. The latter could be tailored through water content in the ZnO pretreatment atmosphere.

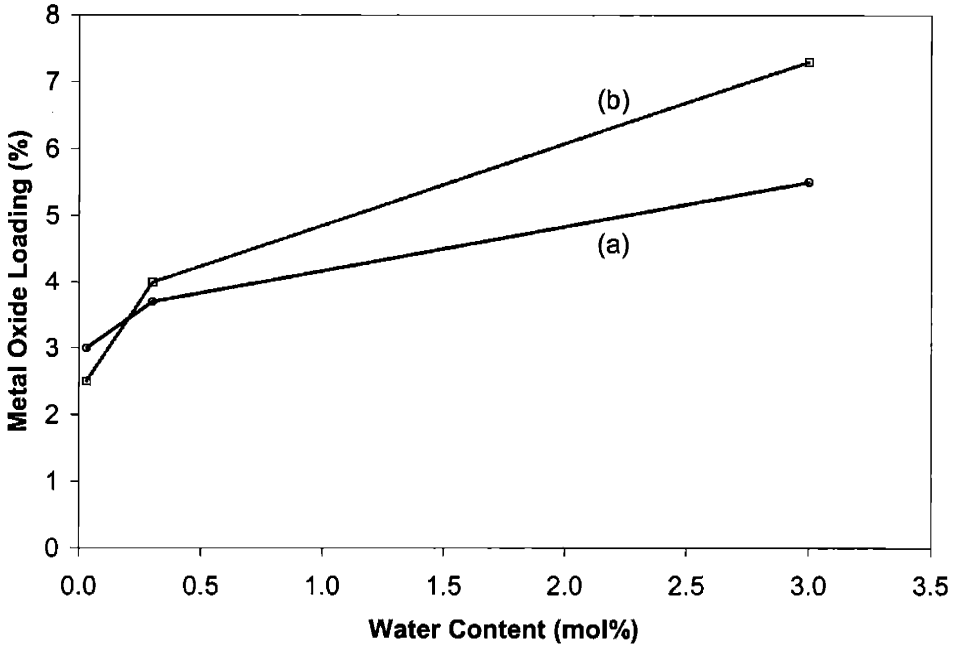

Figure 4.14 (a) TiO_2 and (b) ZrO_2 loadings on ZnO nanoparticles that were pretreated at 25°C in a flowing He gas stream containing different water contents.

For the ZrO_2-coated ZnO materials, 4.0 wt% ZrO_2 loading provided greater microstructural stability than 2.5 wt% ZrO_2 loading (Figures 4.15 and 4.16). Increasing the ZrO_2 loading to 7.3 wt% did not give rise to further improvement in surface area and grain size at 500°C, but was beneficial at 700°C where a maximum surface area of 21 m^2/g and a minimum grain size of 33 nm were achieved for ZrO_2-coated ZnO. The TiO_2-coated ZnO materials achieved superior microstructural stability to ZrO_2-coated ZnO regardless of secondary oxide loading at both 500°C and 700°C. Increasing the TiO_2

loading above 3 wt% increased the surface area and reduced the grain size of TiO_2-coated ZnO slightly at both 500°C and 700°C. 5.5 wt% TiO_2 loading resulted in materials that retained a high surface area of 70 m^2/g and an ultrafine grain size of 13 nm at 500°C.

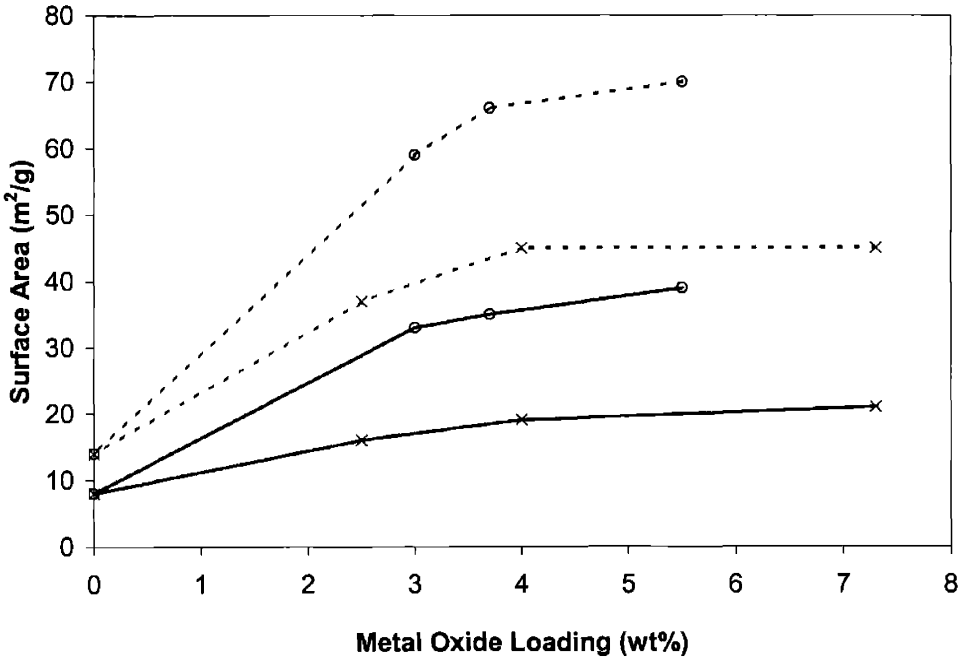

Figure 4.15 BET surface areas of (o) TiO_2- and (x) ZrO_2-coated ZnO nanoparticles calcined to 500°C (---) and 700°C (—).

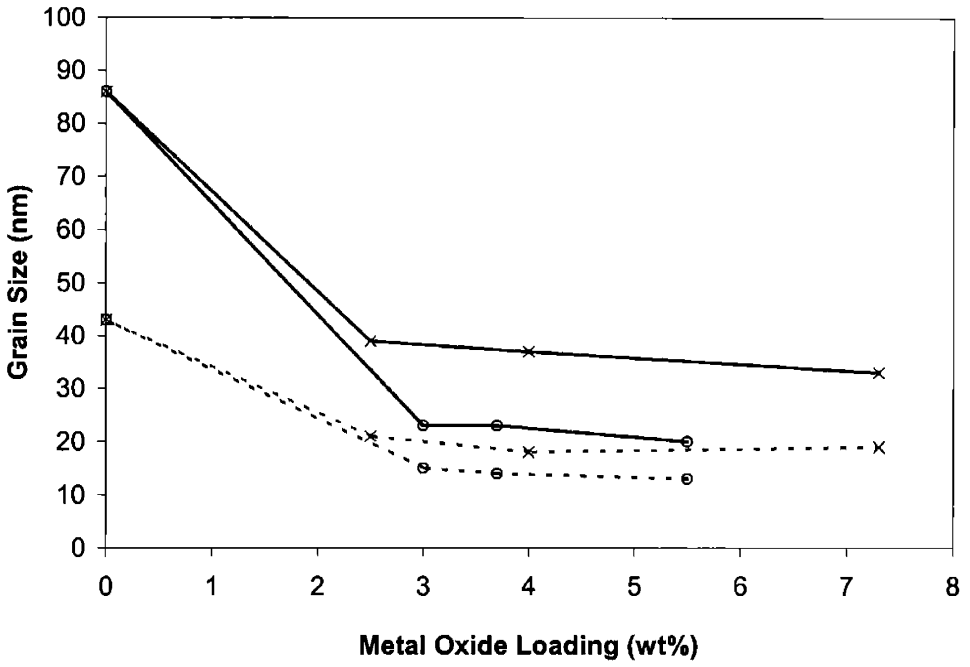

Figure 4.16 XRD grain sizes of (o) TiO_2- and (x) ZrO_2-coated ZnO nanoparticles calcined to 500°C (---) and 700°C (—).

4.3.3 H_2S Absorption Studies

The performance of the ZnO-based absorbents was evaluated by measuring the evolution of H_2S over time using the vertical packed bed reactor described in Section 4.2.3. Ideally, the absorption curve consists of an initial period of essentially zero H_2S emission ([H_2S] < 1 ppm). The point where H_2S is found in the effluent stream marks the absorption limit or breakthrough point for the absorbent. The breakthrough point represents the operational limit of the material prior to regeneration or replacement. The conversion is given by the amount of H_2S that was absorbed by the material prior to breakthrough relative to the theoretical maximum H_2S amount that can be absorbed for complete conversion of ZnO to ZnS. The secondary oxide coating is assumed to be inert in calculating the ZnO conversion. The literature indicated that 85-90% of the conventional ZnO can be converted to ZnS at 538°C prior to breakthrough at a GSHV of 2,000 hr^{-1} [10, 30]. For mobile source or off-shore sulfur treatment, however, minimizing the volume and weight of the absorbent bed becomes essential. With a fixed flow rate, the bed volume is simply an inverse function of space velocity. To ensure both absorbent

weight and vessel size are minimized, the operational limit for space velocity must be extended beyond the typical 2,000 hr^{-1}.

4.3.3.1 H_2S Absorption over Nanocrystalline ZnO

Absorption analysis of nanocrystalline and conventional ZnO at 300°C showed the 100% H_2S removal over 0.1, 0.8, 1.2 and 2.9 hours for conventional ZnO, 43-nm, 28-nm and 13-nm ZnO, respectively (Figure 4.17). This corresponded to conversions of 6%, 20%, 30% and 67%, and demonstrated the effect of reducing ZnO grain size on the H_2S absorption capacity. When the absorption temperature was increased to 500°C, a significant difference was still observed between the nanocrystalline and conventional ZnO (Figure 4.18). Absorption periods increased significantly from 0.8 to 3.0 hours for 43-nm ZnO, and from 0.1 to 2.1 hours for conventional ZnO. This corresponded to an increase in conversion from 20% to 70% and from 6% to 50%, respectively, for these materials.

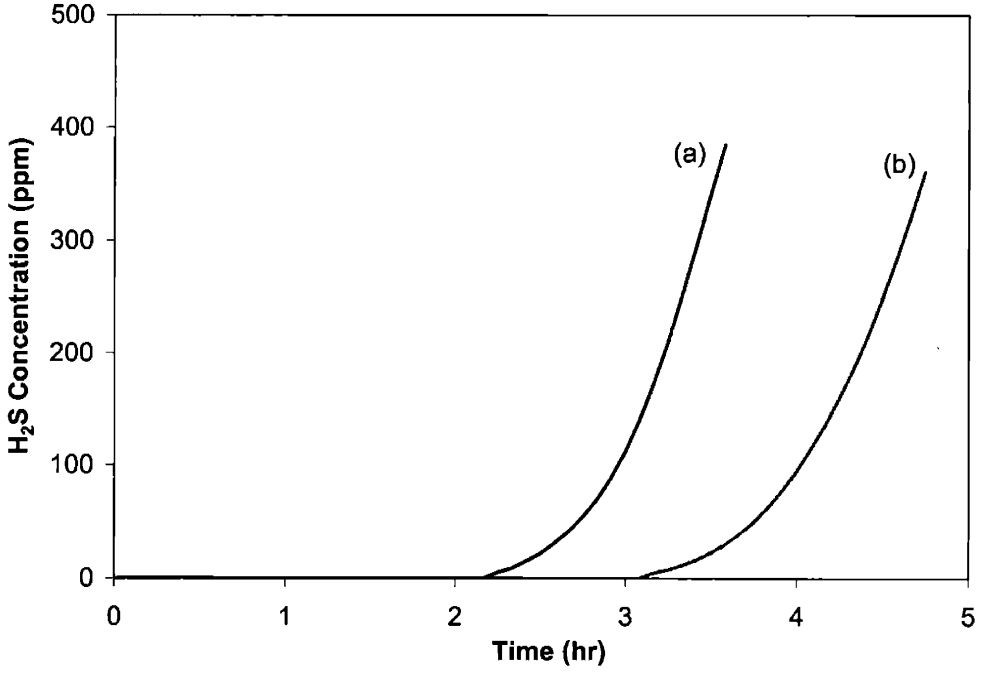

Figure 4.17 H_2S absorption analysis for (a) conventional ZnO (130 nm), (b) nanocrystalline ZnO calcined to 500°C (43 nm), (c) nanocrystalline ZnO calcined to 400°C (28 nm) and (d) nanocrystalline ZnO calcined to 300°C (13 nm), with 1000 ppm H_2S in He at 30,000 hr^{-1} and 300°C.

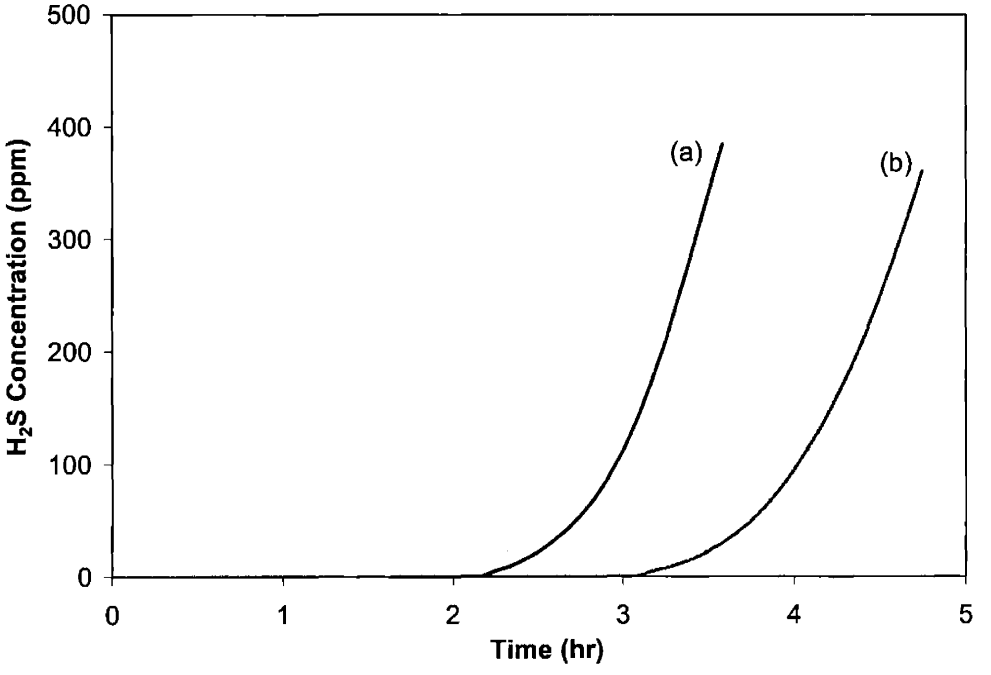

Figure 4.18 H_2S absorption analysis for (a) conventional ZnO (130 nm) and (b) nanocrystalline ZnO calcined to 500°C (43 nm), with 1000 ppm H_2S in He at 30,000 hr^{-1} and 500°C.

To verify the influence of diffusion, an analysis of sulfur penetration depth at breakthrough for the nanocrystalline and conventional ZnO was performed. The sulfur penetration depth within the materials should be the same if in fact diffusion was important. The analysis was simplified by assuming spherical particles and calculating a theoretical grain radius (r_o) to account for agglomeration:

$$r_o = \frac{3}{\rho\ A_s} \qquad (4.1)$$

where ρ is the density of pure ZnO (5.41 g/cm^3) and A_s is the surface area in cm^2/g. By assuming a uniform conversion at breakthrough over the bed (X), the theoretical unreacted radius (r_u) of ZnO can be calculated with Equation 4.2,

$$r_u = (1-X)^{1/3}\ r_o \qquad (4.2)$$

The penetration depth is then just the difference between r_o and r_u. The calculated penetration depth was 2 nm at 300°C (averaging over the three nanocrystalline materials and bulk ZnO) and 13 nm at 500°C (averaging over the 43-nm ZnO and bulk ZnO), with errors of 15% and 10%, respectively. The difference in penetration depth between 300°C

and 500°C showed that the effect of grain size was less significant at higher temperature, as expected for a diffusion-controlled process. The data also suggested that at 300°C, 100% conversion would be achieved by a 4-nm ZnO material.

The conversion at breakthrough as a function of grain radius (r_o) was examined to illustrate the effect of both temperature and diffusion on the performance of the various ZnO materials (Figure 4.19). At a given temperature, a significant increase in overall conversion was achieved with reduced grain radius, especially at low temperatures. When grain radius was decreased from 21.5 nm to 6.5 nm, the overall conversion increased by more than threefold at 300°C. By rearranging Equation 4.2, conversion was obtained as a function of r_o^{-3}; thus, prior to reaching the point of inflection, conversion should increase rapidly with just a slight decrease in grain size. This was evident in Figure 4.19(a), which showed significant increase in conversion at grain radius of $\leq$ 10 nm.

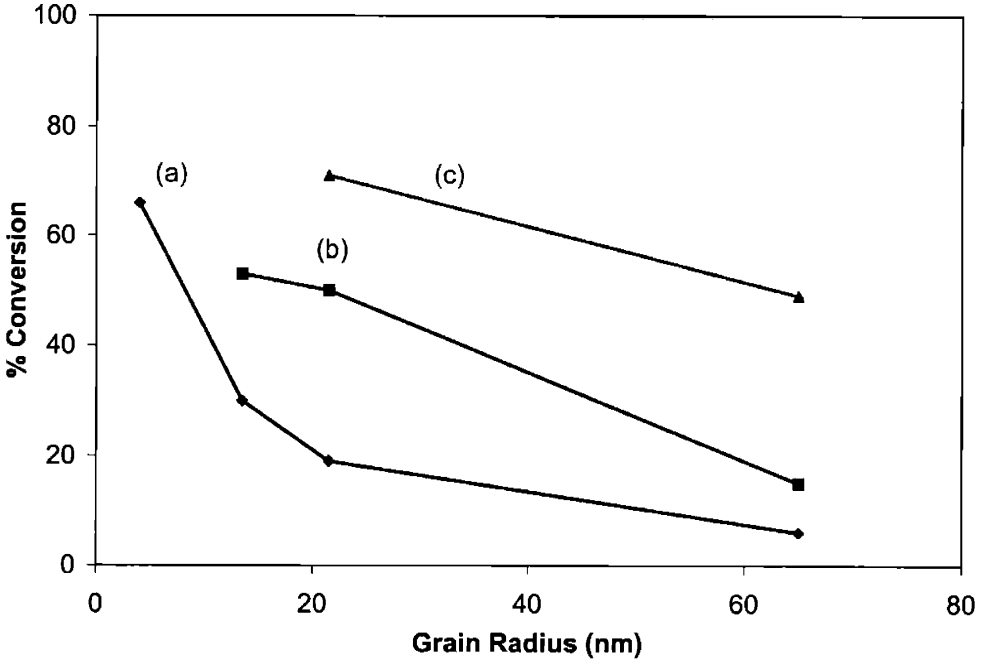

Figure 4.19 Effect of grain radius on ZnO breakthrough conversion at (a) 300°C, (b) 400°C and (c) 500°C, with 1000 ppm H_2S in He at 30,000 hr^{-1}.

4.3.3.2 H_2S Absorption over TiO_2- and ZrO_2-coated ZnO Nanocrystals

Through the use of a secondary oxide coating, the grain size of ZnO was stabilized against grain growth. In particular, TiO_2-coated ZnO calcined to 500°C showed an ultrafine grain size of only 10 nm. This material allowed for 100% H_2S removal over 3.2 hours at 300°C (Figure 4.20 (b)), which translated to 81% conversion at breakthrough. The ZrO_2-coated ZnO calcined to 500°C (17 nm) showed no improvement in absorption time (2.8 hours) over the nanocrystalline ZnO (13 nm, 2.8 hours) at 300°C. This was due to the presence of inactive ZrO_2, since the ZnO conversion of the former (72%) was higher than the 66% achieved by the pure nanocrystalline ZnO. Both TiO_2- and ZrO_2-coated ZnO calcined to 700°C achieved a similar absorption time of 2.5 hours, with ZnO conversions of 63% and 65%, respectively, despite the significant difference in their grain sizes (15 nm versus 29 nm). This could have resulted from either ZrO_2 providing improved H_2S adsorption or a less favorable interaction between TiO_2 and ZnO that inhibited conversion. Although the $ZnTiO_3$ phase was not evident at 700°C, the presence of a plateau in the absorption profile prior to accelerated absorption, which has been seen in the literature for mixed-phase TiO_2-ZnO materials, suggested that a secondary phase was present at the surface that inhibited absorption [10]. The penetration depths for TiO_2- and ZrO_2-coated ZnO of 2.5 nm and 4.0 nm, respectively, were higher than the 2.0 nm for the pure nanocrystalline ZnO, confirming that H_2S absorption was enhanced for coated ZnO materials, especially when ZrO_2 was deposited as the secondary oxide coating.

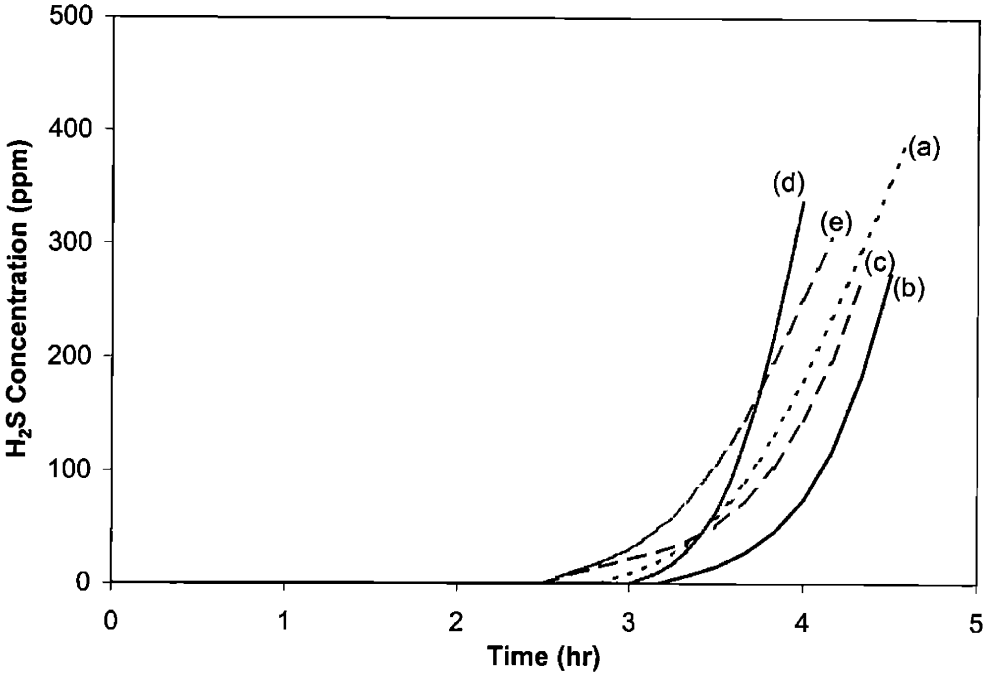

Figure 4.20 H_2S absorption analysis for (a) nanocrystalline ZnO calcined at 300°C, TiO_2-coated ZnO nanocrystals calcined at (b) 500°C and (c) 700°C, and ZrO_2-coated ZnO nanocrystals calcined at (d) 500°C and (e) 700°C, with 1000 ppm H_2S in He at 30,000 hr^{-1} and 300°C.

94% and 97% conversions at breakthrough and 100% H_2S removal over 3.9 hours were achieved at 500°C for ZrO_2- and TiO_2-coated ZnO calcined at 500°C (Figure 4.21). Unlike the 300°C absorption analysis, calcination of the coated ZnO materials at 700°C had no effect on absorption performance, with conversion and time to breakthrough remaining the same as the coated ZnO materials calcined at 500°C. This was not unexpected since for pure ZnO, the theoretical penetration depth was 13 nm at 500°C. Thus, assuming the diffusion depth to be the same for TiO_2- and ZrO_2-coated ZnO, complete conversion should be achieved for both materials calcined at 700°C since their grain sizes were only 15 nm and 29 nm, respectively.

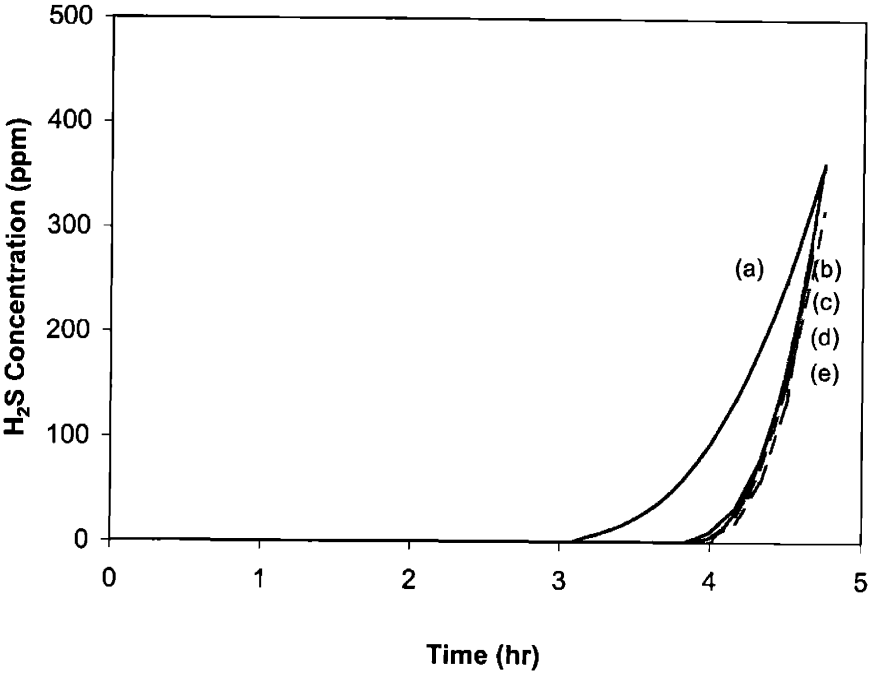

Figure 4.21 H_2S absorption analysis for (a) nanocrystalline ZnO calcined at 500°C, TiO_2-coated ZnO nanocrystals calcined at (b) 500°C and (c) 700°C, and ZrO_2-coated ZnO nanocrystals calcined at (d) 500°C and (e) 700°C, with 1000 ppm H_2S in He at ~30,000 hr^{-1} and 500°C.

4.3.4 Regeneration of Pure and Coated ZnO Nanocrystals

The main criteria for determining the effectiveness and viability of the regeneration process are the performance of the regenerated material compared to the fresh (unused) absorbent, and the time and condition required for complete regeneration. For the regeneration of solid H_2S absorbents, typically O_2 is introduced over the metal sulfide material to convert it to metal sulfate. The sulfate can then be decomposed either by thermal degradation above 600°C, or by a combination of thermal degradation and reduction. By decreasing the O_2 present in the gas stream to < 2%, ZnS can undergo a single-step conversion to ZnO with SO_2 evolving from the metal oxide prior to sulfate formation [10]. However, this process requires longer regeneration time, and the presence of a diluent stream to reduce the O_2 concentration.

4.3.4.1 Evolution of SO_2 from Pure and Coated ZnO Nanocrystals

Knowledge of the ZnS-to-ZnO conversion is critical towards achieving complete regeneration at the highest rate possible with minimal grain growth. An initial analysis

was performed on pure ZnO, and TiO_2- and ZrO_2-coated ZnO nanocrystals to evaluate the temperature needed for complete regeneration (Figure 4.22). H_2S was first absorbed onto these 500°C-calcined materials at 500°C, followed by a temperature-programmed oxidation between 200°C and 700°C (ramp = 1°C/min) in air. Peak SO_2 evolution occurred at 595°C, 598°C and 590°C for conventional ZnO, 500°C-calcined ZnO nanocrystals and ZrO_2-coated ZnO nanocrystals, respectively. TiO_2-coated ZnO nanocrystals had the highest peak SO_2 desorption temperature of 610°C. Complete SO_2 evolution was attained by 630°C for all materials. Therefore, a regeneration temperature of 650°C was employed to maximize regeneration rate while minimizing structural instability.

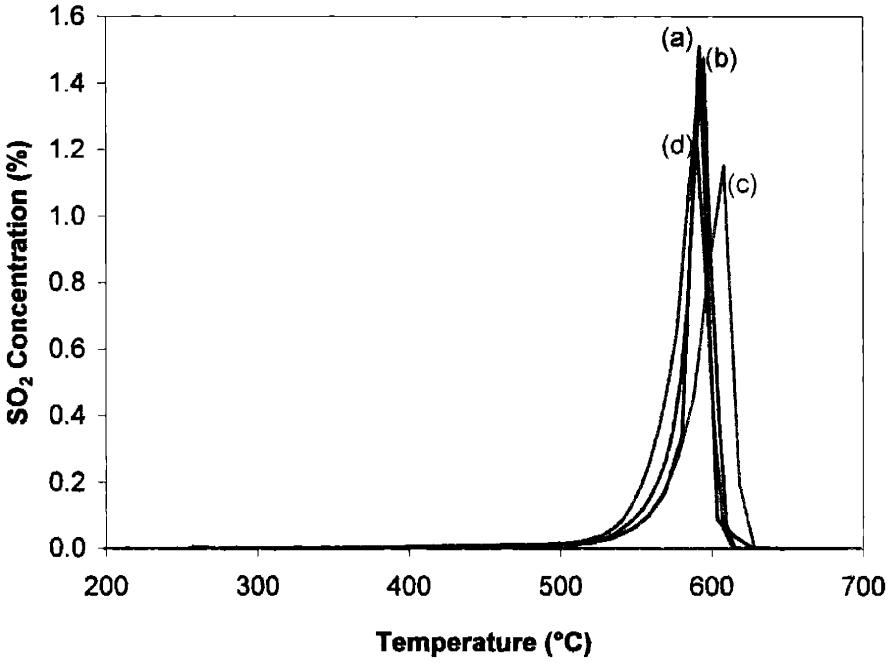

Figure 4.22 Temperature-programmed desorption of presulfided (a) conventional ZnO, (b) 500°C-calcined nanocrystalline ZnO, (c) TiO_2-coated ZnO nanocrystals and (d) ZrO_2-coated ZnO nanocrystals in air at 30,000 hr^{-1}.

4.3.4.2 Regeneration of Nanocrystalline and Conventional ZnO

Conventional and nanocrystalline ZnO were regenerated in an air stream at 650°C (ramp rate = 10°C/min) for 4 hours after each absorption cycle. Nanocrystalline ZnO removed 100% of the inlet H_2S for 2.8 hours, achieving 70% breakthrough conversion reproducibly at 500°C over 3 cycles (Figure 4.23). It experienced a minor grain growth from 44 nm to 50 nm with no change in surface area (15 m^2/g). Conventional ZnO

removed 100% of the inlet H_2S for 2.8 hours with 70% breakthrough conversion for the second and third cycles, following an initial breakthrough period of 2.1 hours with 50% conversion at 500°C (Figure 4.24). Although conventional ZnO is widely thought to be non-regenerable, previous literature has discussed the possibility of regeneration through increased surface area. However, the increased ZnO surface area from regeneration was attributed to oxygen-induced surface roughening and there was no mention of improved microstructure [10]. Our analysis showed that the conventional material actually underwent a significant reduction in grain size from 130 nm to 60 nm upon regeneration, with a two-fold increase in surface area to 14 m^2/g. Thus, its improved absorption characteristics in the second and third cycles could be attributed to its finer microstructure following regeneration.

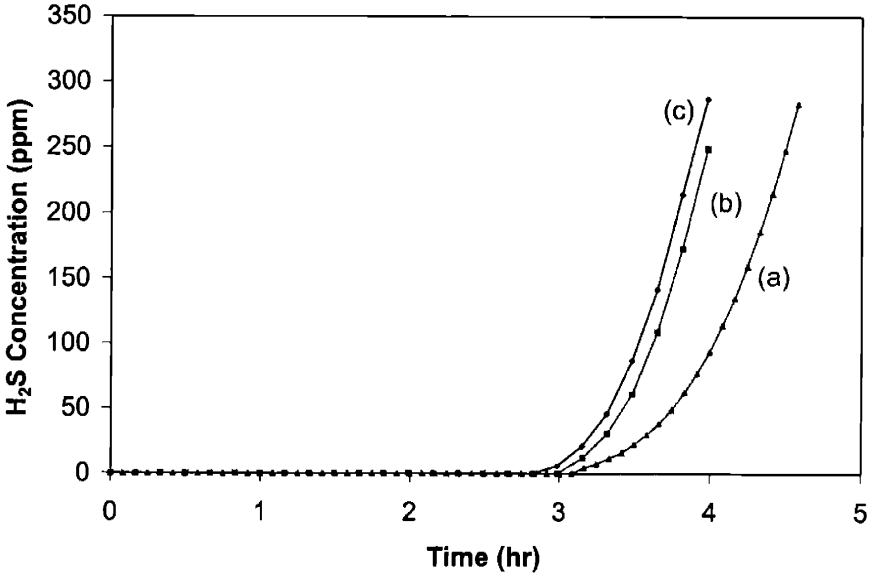

Figure 4.23 H_2S absorption analysis for 500°C-calcined nanocrystalline ZnO with 1000 ppm H_2S in He at 30,000 hr^{-1} and 500°C: (a) first cycle, (b) second cycle and (c) third cycle. The sample was regenerated in air at 650°C for 4 hours at 30,000 hr^{-1} after each absorption cycle.

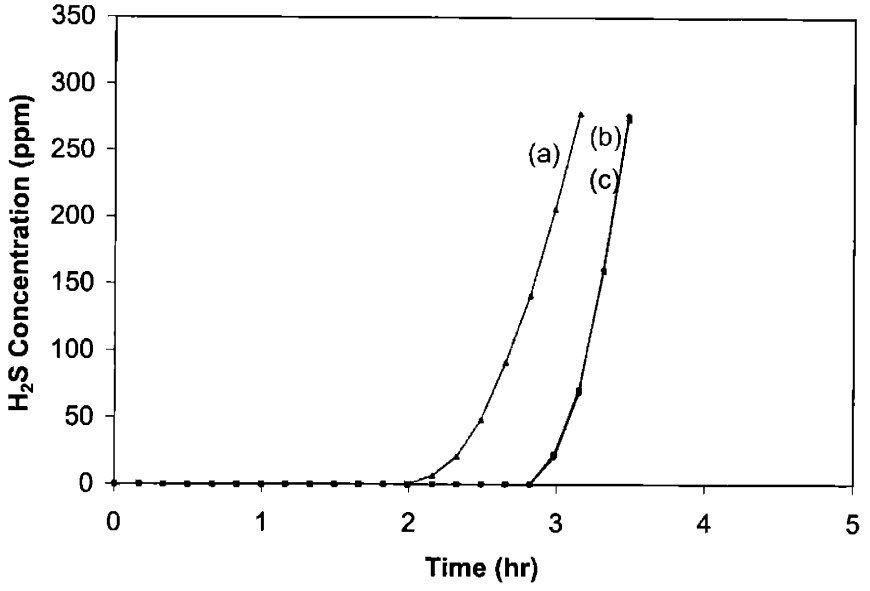

Figure 4.24 H_2S absorption analysis for conventional ZnO with 1000 ppm H_2S in He at 30,000 hr^{-1} and 500°C: (a) first cycle, (b) second cycle and (c) third cycle. The sample was regenerated in air at 650°C for 4 hours at 30,000 hr^{-1} after each absorption cycle.

TEM analysis was performed on the nanocrystalline and conventional ZnO before and after 3 absorption cycles (Figure 4.25). The initial microstructures of the two materials differed significantly. The 500°C-calcined nanocrystalline ZnO consisted of discrete particles of 10-100 nm, with a grain size of 43 nm. The conventional ZnO had a larger particle size distribution of 20 nm to 500 nm, with an average particle size of ~ 130 nm. Through the process of sulfation and oxide reprecipitation, the microstructures of both materials underwent significant changes. The particle size distribution for nanocrystalline ZnO became much broader after regeneration, while maintaining a similar average particle size. For conventional ZnO, the particle size distribution remained broad, however, the average particle size was significantly reduced after regeneration such that it matched that of the nanocrystalline ZnO.

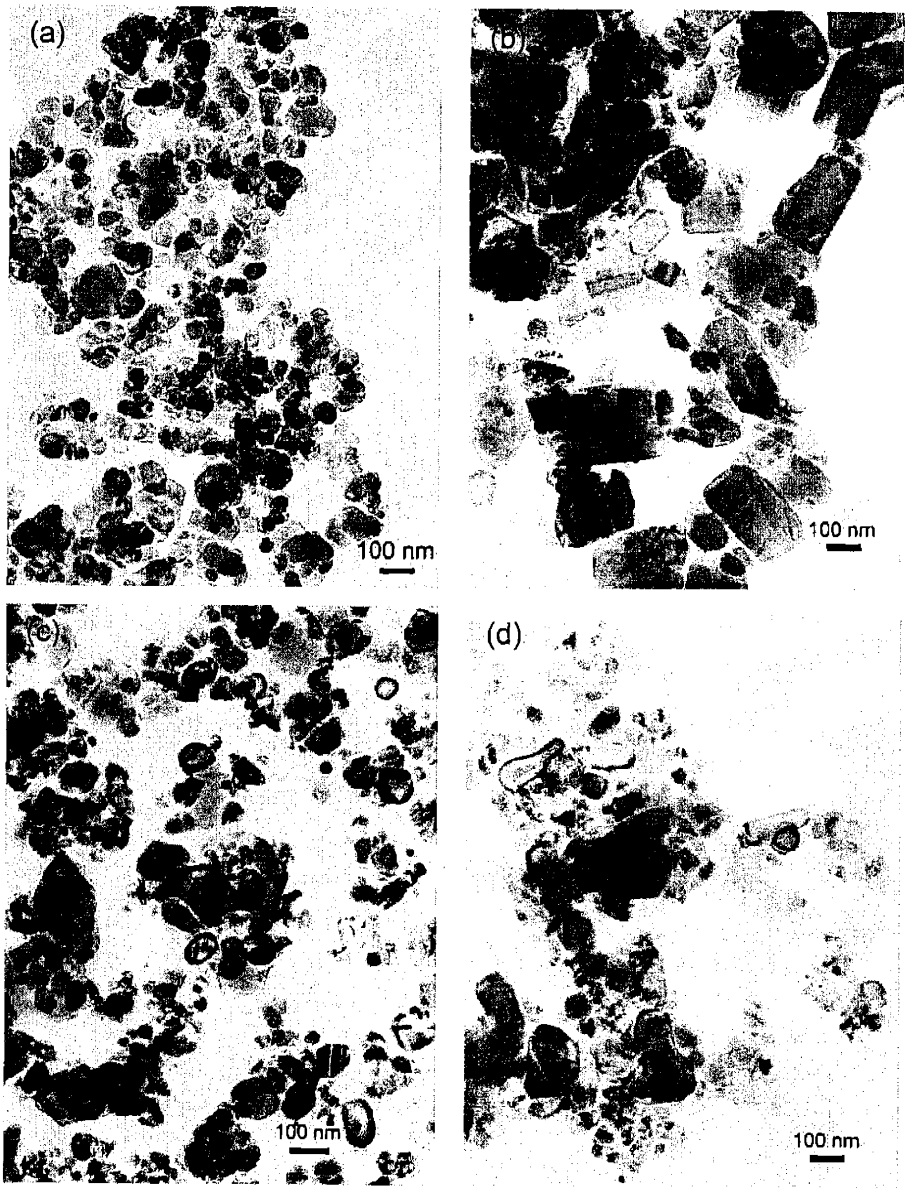

Figure 4.25 TEM micrographs of (a) 500°C-calcined nanocrystalline ZnO and (b) conventional ZnO, and (c) nanocrystalline and (d) conventional ZnO following the third regeneration in air at 650°C for 4 hours at 30,000 hr^{-1}.

The reduction in average particle size in conventional ZnO could have resulted from differences in the ZnO and ZnS structures. Although they both conform to a $P6_3mc$ symmetry, the crystal lattice experiences significant expansion and contraction through the absorption and regeneration cycles. The density ratio of ZnO to ZnS is 1.39, so there is $\leq$ 39% decrease in density during H_2S absorption. The *a* lattice parameter would expand from 3.25 Å to 3.82 Å in the ZnO-to-ZnS conversion. The *c* lattice parameter would increase even more significantly from 5.21 Å to 24.96 Å per super cell. This

drastic change in crystal structure has been shown to cause premature loss in activity for porous ZnO from pore blocking [6, 30]. It was likely that the lattice changes contributed to the microstructural changes in the nanocrystalline and conventional ZnO during the regeneration process.

4.3.4.3 Regeneration of TiO_2- and ZrO_2-coated ZnO Nanocrystals

700°C-calcined TiO_2- and ZrO_2-coated ZnO showed superior performance compared to the conventional and nanocrystalline ZnO after regeneration (Figures 4.26 and 4.27). TiO_2-coated ZnO achieved 99%, 96% and 86% conversions at breakthrough in the first, second and third absorption cycles at 500°C, with 100% H_2S removal over 4.0 hours, 3.9 hours and 3.5 hours, respectively. The significant decrease in conversion over the third cycle suggested some degradation in material properties. In contrast, ZrO_2-coated ZnO attained 91%, 90% and 88% conversions at breakthrough in the first three cycles at 500°C, with 100% H_2S removal over 3.8 hours, 3.8 hours and 3.7 hours, respectively.

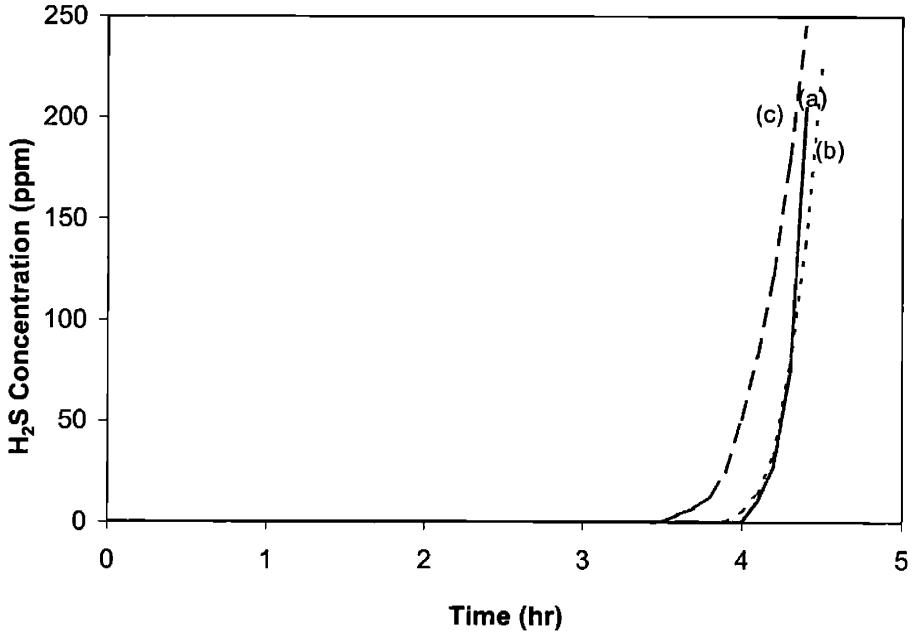

Figure 4.26 H_2S absorption analysis for 700°C-calcined TiO_2-coated ZnO with 1000 ppm H_2S in He at 30,000 hr^{-1} and 500°C: (a) first cycle (——), (b) second cycle (----) and (c) third cycle (– – –). The sample was regenerated in air at 650°C for 4 hours at 30,000 hr^{-1} after each absorption cycle.

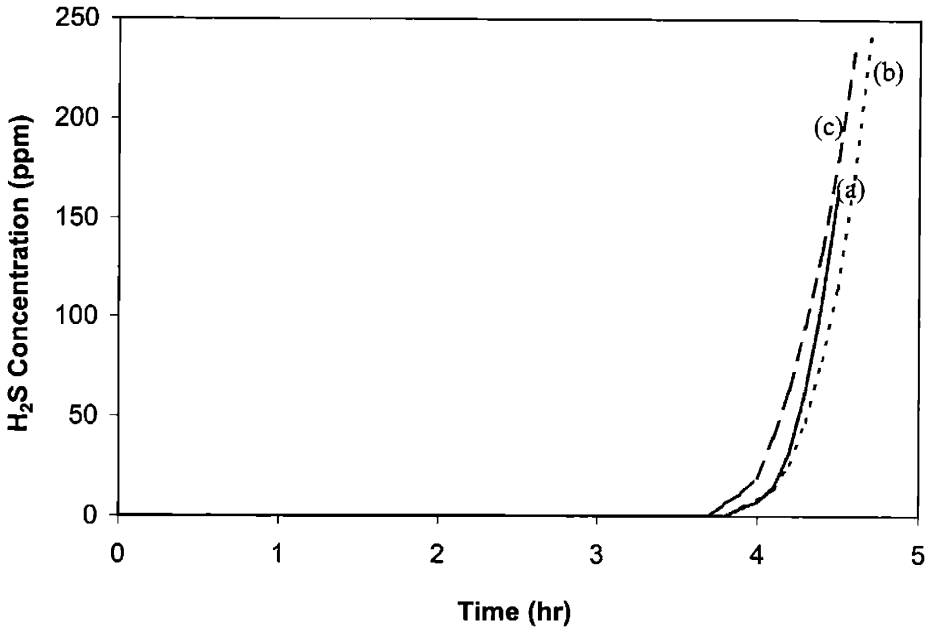

Figure 4.27 H_2S absorption analysis for 700°C-calcined ZrO_2-coated ZnO with 1000 ppm H_2S in He at 30,000 hr^{-1} and 500°C: (a) first cycle (——), (b) second cycle (----) and (c) third cycle (– – –). The sample was regenerated in air at 650°C for 4 hours at 30,000 hr^{-1} after each absorption cycle.

The 700°C-calcined TiO_2-coated ZnO experienced substantial grain growth from 15 nm to 33 nm upon regeneration, which was accompanied by a reduction in surface area from 61 m^2/g to 26 m^2/g. These microstructural changes could be attributed to the development of a secondary $ZnTiO_3$ phase, which grew at the expense of the highly dispersed TiO_2 surface coating on ZnO over three regeneration cycles (Figure 4.28). ZrO_2-coated ZnO showed a slight increase in grain size from 29 nm to 35 nm upon regeneration, but lost nearly half of its original surface area (31 m^2/g) to 17 m^2/g. The development of a separate ZrO_2 phase was also noted in XRD analysis.

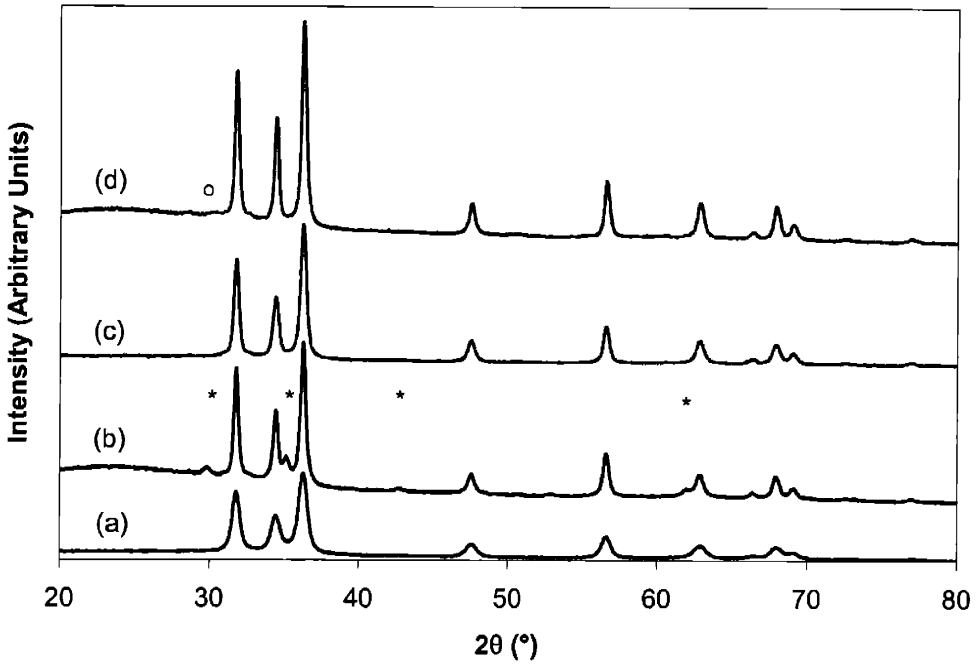

Figure 4.28 XRD patterns of (a) 700°C-calcined and (b) thrice-regenerated TiO_2-coated ZnO, and (a) 700°C-calcined and (b) thrice-regenerated ZrO_2-coated ZnO. Peaks associated with ZnO (unmarked), $ZnTiO_3$ (*) and ZrO_2 (o) were observed.

TEM analysis of TiO_2-coated ZnO illustrated that the 700°C-calcined material underwent a coarsening in particle size from < 20 nm to 10-50 nm (Figure 4.29). For the ZrO_2-coated ZnO, a particle size distribution of 10-50 nm was maintained through regeneration. Particle agglomeration was more noticeable for both TiO_2- and ZrO_2-coated ZnO following regeneration. The similarity in grain size and microstructure in Figures 4.29(c) and (d) explained the similar absorption capacity for the TiO_2- and ZrO_2-coated ZnO materials over the third cycle. These coated ZnO materials experienced only minor structural changes in regeneration. Thus, their superior absorption activity to the conventional and nanocrystalline ZnO was maintained due to their high thermal stability in multiple absorption-regeneration cycles.

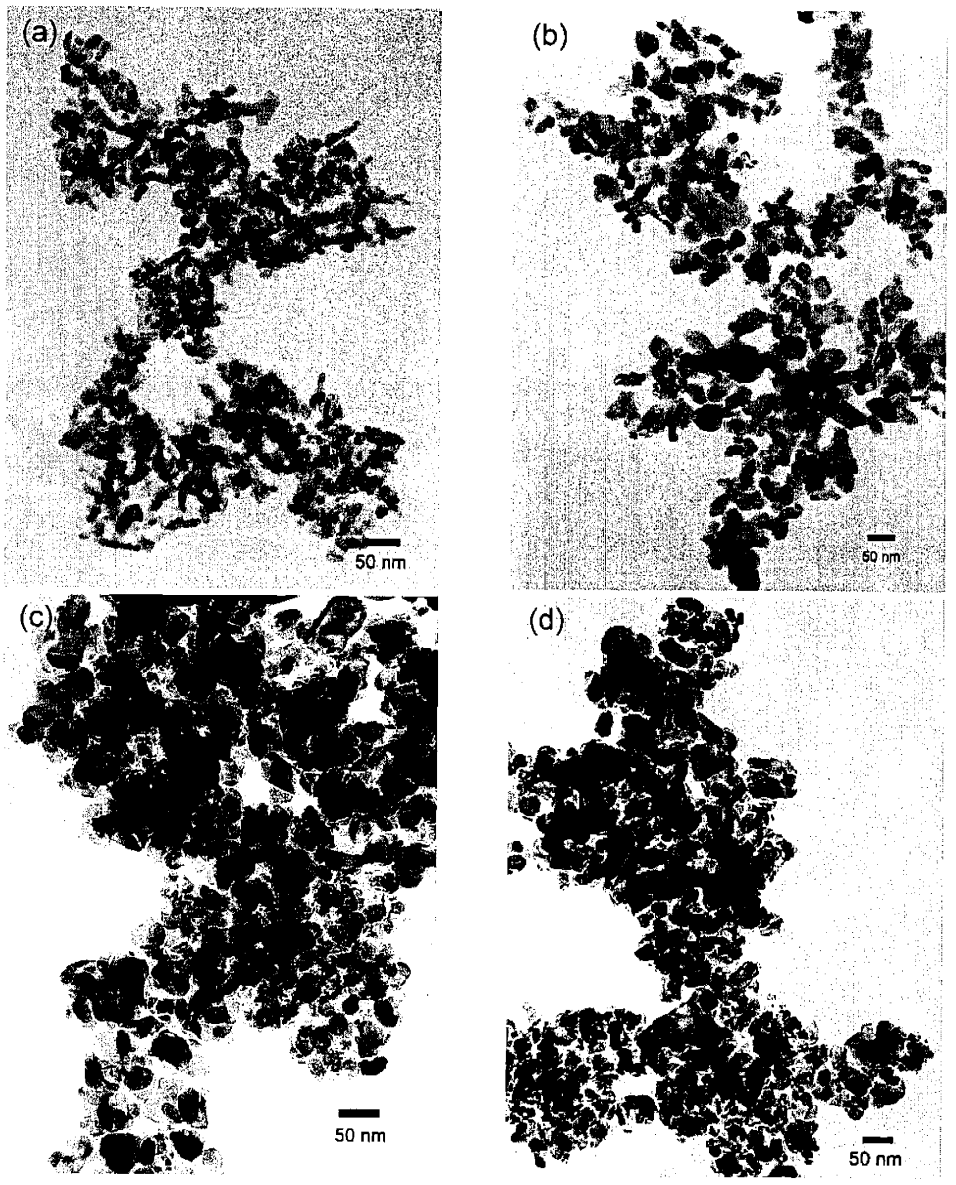

Figure 4.29 TEM micrographs of 700°C-calcined (a) TiO_2- and (b) ZrO_2-coated ZnO, and (c) TiO_2- and (d) ZrO_2-coated ZnO following the third regeneration cycle in air at 650°C for 4 hours at 30,000 hr^{-1}.

4.3.5 H_2S Absorption Kinetics

The H_2S absorption studies on pure and coated ZnO nanocrystals in Sections 4.3.3 and 4.3.4 provided information on the H_2S removal efficiency in a simulated industrial absorption process. However, to understand differences between the various ZnO materials, it would be useful to analyze ZnO conversion in a model environment. By monitoring the weight change of a given material over time while maintaining a constant

gas-phase H_2S concentration and temperature, the effects of grain size and coating composition as well as intrinsic surface kinetics could be examined. From preliminary studies, it was determined that a flow rate of > 300 sccm should be maintained to ensure consistent absorption results. Thus, all experiments were performed using a flow rate of 500 sccm. To achieve experimental reproducibility, a sample surface area of < 175 cm^2 was used.

4.3.5.1 Effect of Grain Size and Absorption Temperature on ZnO Conversion

An analysis of the weight change with time for conventional and nanocrystalline ZnO at 300°C showed the effect of grain size on the rate of conversion (Figure 4.30). Conventional ZnO (130 nm) achieved only 16% conversion in 60 min in a stream of 0.4% H_2S in He. In contrast, nanocrystalline ZnO calcined to 400°C (27 nm) and 500°C (43 nm) attained 65% and 50% conversion, respectively. The finer grain size of the 300°C-calcined nanocrystalline ZnO (16 nm) provided for a significant increase in conversion to 93%. The decreased absorption with increased grain size and the incomplete conversion at 300°C indicated that diffusion was a significant factor at this absorption temperature.

During the absorption cycle, the ZnO conversion was first dictated by surface kinetics, then by both diffusion and kinetics, and finally, by diffusion alone. Therefore, during the initial absorption stage, both conventional and nanocrystalline ZnO should exhibit similar absorption rates. The 300°C-calcined nanocrystalline ZnO maintained the high initial slope for a long period of time, achieving nearly 20% conversion. In contrast, the conventional material achieved only 2% conversion in the initial stage that was dominated by intrinsic surface kinetics. This was expected given the order of magnitude decrease in surface area and increase in grain size with the conventional ZnO compared to 300°C-calcined nanocrystalline ZnO. The 300°C-calcined material also remained in the intermediate region governed by diffusion and kinetics for a significant period of time, whereas the conventional material transitioned rapidly to a diffusion-controlled process as indicated by another change in slope.

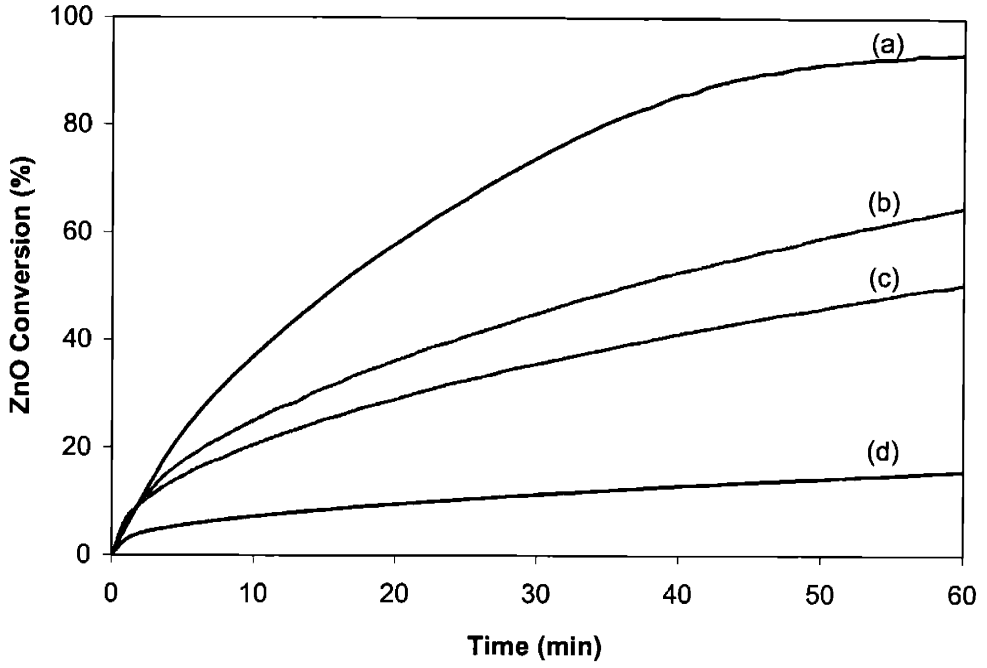

Figure 4.30 TGA analysis of H_2S absorption for nanocrystalline ZnO calcined to (a) 300°C, (b) 400°C and (c) 500°C, and (d) conventional ZnO, with 500 sccm of 0.4% H_2S in He at 300°C.

The effect of absorption temperature was examined for both nanocrystalline and conventional ZnO. Conventional ZnO showed an increase in conversion from 16% at 300°C to 57% at 500°C (Figure 4.31). Final conversion over the 60-min cycle fell short of 100% for 300-500°C. This result was similar to that found by Gibson *et al.*, who showed that the reaction between conventional ZnO and H_2S ceased prior to reaching full ZnO-to-ZnS conversion (maximum ZnO-to-ZnS conversion was < 65% for 300-500°C) [5]. In contrast, 500°C-calcined nanocrystalline ZnO showed ~ 50% conversion at 300°C, attaining > 90% conversion at 400°C and 500°C (Figure 4.32).

With increased temperature, both nanocrystalline and conventional ZnO experienced an expanded regime whereby the absorption process was kinetically limited. The curvature of both conventional and nanocrystalline ZnO increased significantly with increasing temperature as well. For the 500°C-calcined nanocrystalline ZnO (43 nm), the rate of conversion was greater at 500°C compared to 400°C for the first 30 min, but similarly high final conversions of > 90% were obtained after 60 min of absorption. By reducing the ZnO grain size further, the difference in the absorption profiles at 400°C and

500°C would theoretically disappear, since the ultrafine materials would not be diffusion-controlled at these temperatures.

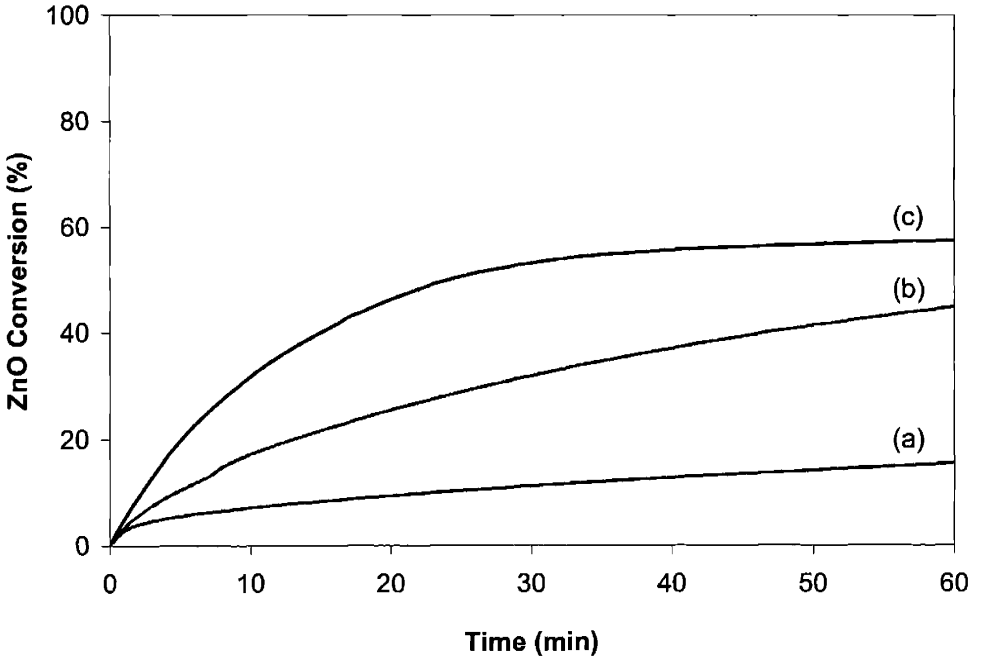

Figure 4.31 TGA analysis of H_2S absorption for conventional ZnO with 500 sccm of 0.4% H_2S in He at (a) 300°C, (b) 400°C and (c) 500°C.

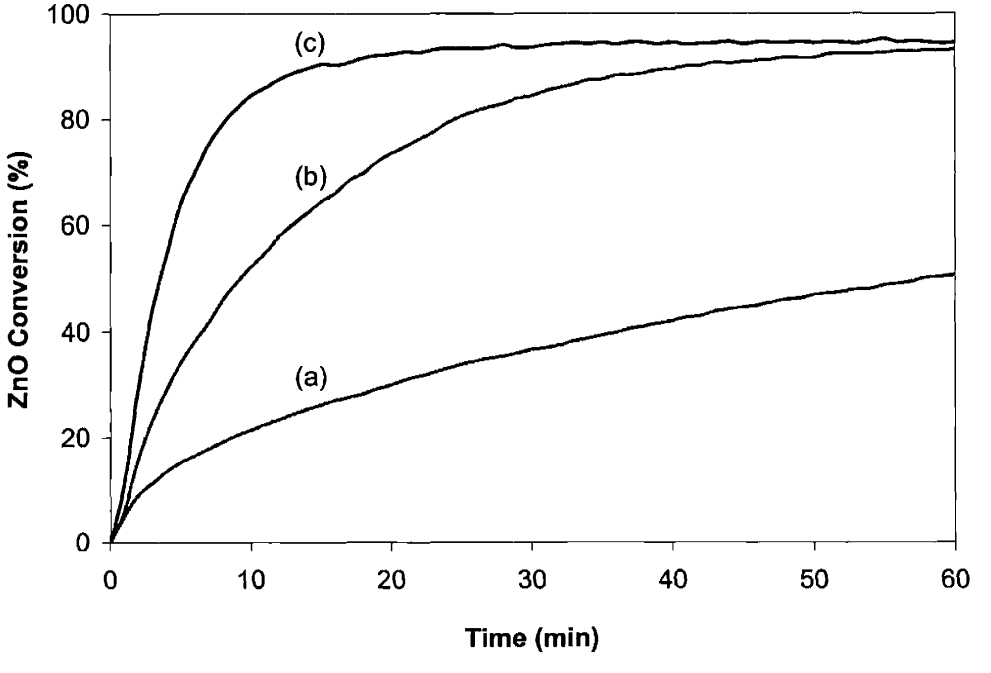

Figure 4.32 TGA analysis of H_2S absorption for 500°C-calcined nanocrystalline ZnO with 500 sccm of 0.4% H_2S in He at (a) 300°C, (b) 400°C and (c) 500°C.

4.3.5.2 Effect of Absorption Temperature on Coated ZnO Conversion

TiO_2-coated ZnO (15 nm) attained 100% conversion within 30 min at 300°C (Figure 4.33). In comparison, ZrO_2-coated ZnO (29 nm) and 300°C-calcined nanocrystalline ZnO (16 nm) achieved nearly 70% conversion and 500°C-calcined nanocrystalline ZnO (43 nm) reached only 35% conversion after 30 min at 300°C. TiO_2-coated ZnO also maintained a rapid initial absorption governed by surface kinetics for a relatively long time period of 5 min, achieving > 40% conversion prior to diffusion becoming a factor. In comparison, the ZrO_2-coated ZnO and 300°C-calcined nanocrystalline ZnO achieved < 25% conversion with kinetically-controlled absorption for < 4 min. The high H_2S absorption rates of TiO_2- and ZrO_2-coated ZnO could not be attributed to the ultrafine grain size alone, suggesting that the TiO_2 and ZrO_2 coatings greatly enhanced the surface absorption kinetics.

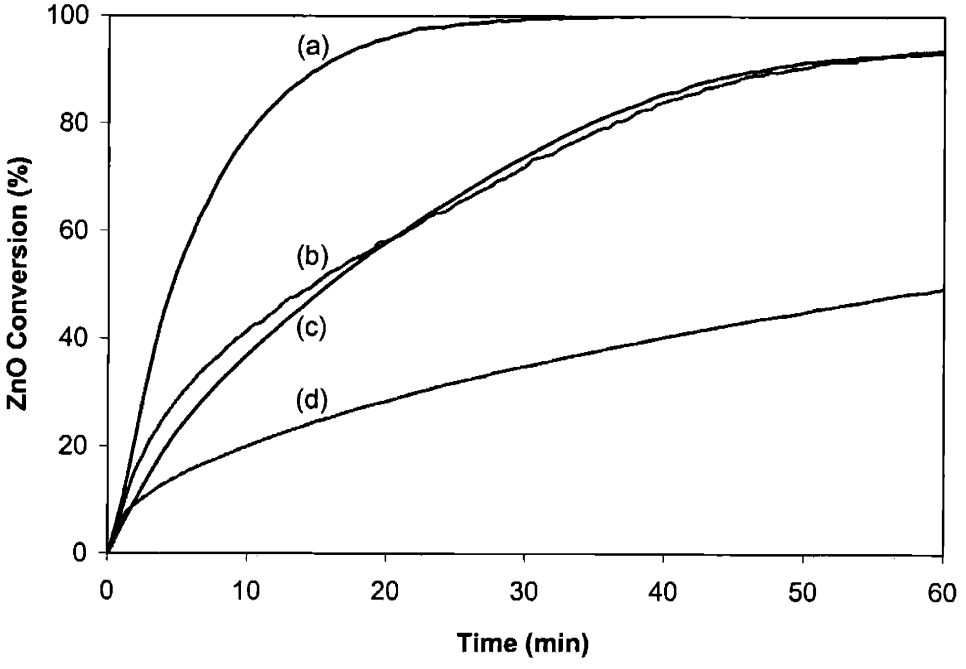

Figure 4.33 TGA analysis of H_2S absorption for (a) TiO_2- and (b) ZrO_2-coated ZnO, and (c) 300°C-calcined and (d) 500°C-calcined nanocrystalline ZnO, with 500 sccm of 0.4% H_2S in He at 300°C.

At 400°C, TiO_2-coated ZnO (15 nm) and ZrO_2-coated ZnO (29 nm) achieved their maximum conversions within 10 and 20 min, respectively. The curvatures of their

absorption profiles were sharper than those at 300°C, attaining 90% conversion in < 10 min. In contrast, the 500°C-calcined nanocrystalline ZnO (43 nm) experienced an initial high activity, followed by the gradual decrease in conversion rate as the rate-limiting step changed from surface reaction to bulk diffusion. This study suggested that diffusion was not a factor in H_2S absorption for ZnO systems with $\leq$ 29 nm at 400°C.

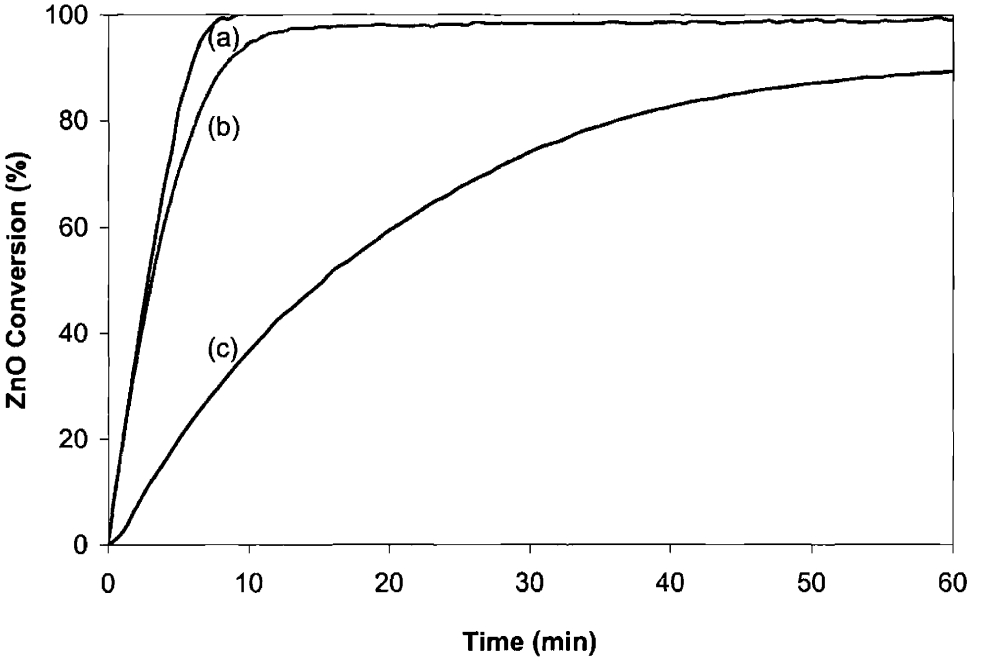

Figure 4.34 TGA analysis of H_2S absorption for (a) TiO_2- and (b) ZrO_2-coated ZnO, and (c) 500°C-calcined nanocrystalline ZnO, with 500 sccm of 0.4% H_2S in He at 400°C.

At 500°C, no significant diffusional effects were observed for TiO_2- or ZrO_2-coated ZnO, which attained similar absorption profiles. The absorption profile for the 500°C-calcined nanocrystalline ZnO maintained a high absorption rate consistent with surface kinetics over the first 4 min, and attained nearly 50% conversion. However, the diffusion effects limited conversion to 96% over 60 min. In contrast, essentially full conversion was achieved for the TiO_2- and ZrO_2-coated ZnO in 10 min and 25 min, respectively.

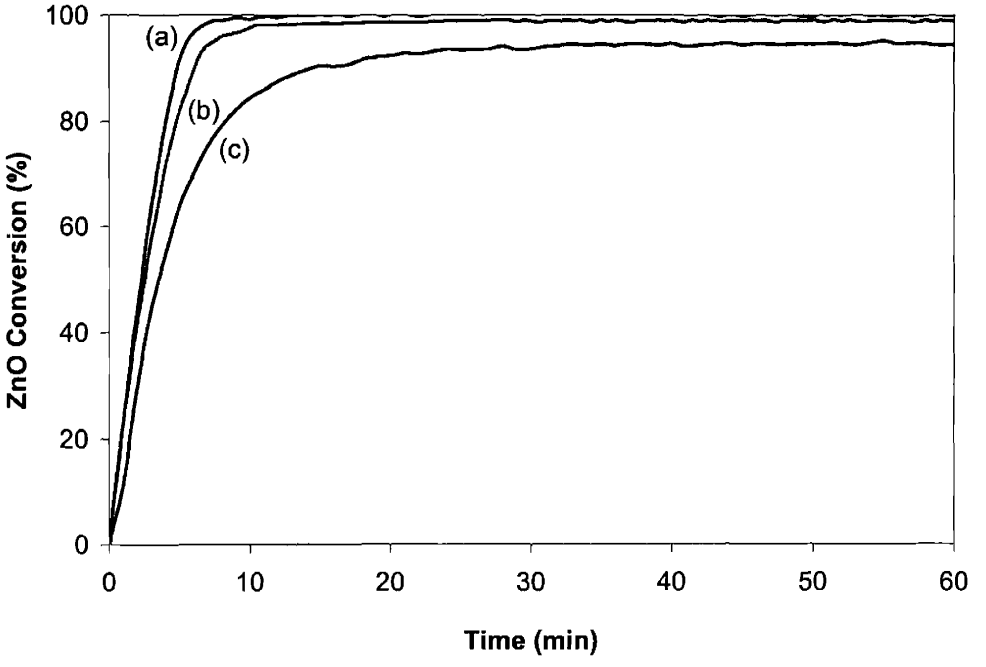

Figure 4.35 TGA analysis of H_2S absorption for (a) TiO_2- and (b) ZrO_2-coated ZnO, and (c) 500°C-calcined nanocrystalline ZnO, with 500 sccm of 0.4% H_2S in He at 500°C.

4.3.5.3 Surface Absorption Kinetics of Pure and Coated ZnO Nanocrystals

During the initial H_2S absorption by ZnO, the rate of conversion was dictated by the reaction kinetics between gas-phase H_2S and the ZnO surface according to Equation 4.3,

$$H_2S + ZnO = H_2O + ZnS \quad (4.3)$$

Previous literature has shown this reaction to be first order in H_2S concentration, and the reaction rate (r_i) could be described by Equations 4.4 and 4.5.

$$r_i = k\,[H_2S] \quad (4.4)$$

$$k = k_0\, e^{\left(-\frac{E_a}{R*T}\right)} \quad (4.5)$$

where k is the reaction rate constant, E_a is the activation energy and R is given by 1.987 kcal/mol/K.

Analysis of reaction rate as a function of H_2S concentration between 300°C and 500°C for 500°C-calcined nanocrystalline ZnO (43 nm) and conventional ZnO (130 nm) confirmed first order kinetics since k was a linear function of H_2S concentration ($R^2 >$ 0.98) (Figures 4.36 and 4.37). The reaction rate profiles for both materials were nearly

identical, so that there was little difference in their Arrhenius plots (Figure 4.38). Thus, the significant microstructural differences had no effect on the reaction rates or the activation energies for conventional ZnO (4.0 kcal/mol) and nanocrystalline ZnO (3.9 kcal/mol). These values were consistent with the literature values of 3.5-10.2 kcal/mol, the higher value of which was obtained with a co-feed of hydrogen that inhibited the reaction [1, 6, 9]. Since conventional and nanocrystalline ZnO exhibited similar surface kinetics, the differences in their absorption profiles were attributed to sulfur diffusion, which was greatly affected by ZnO grain size.

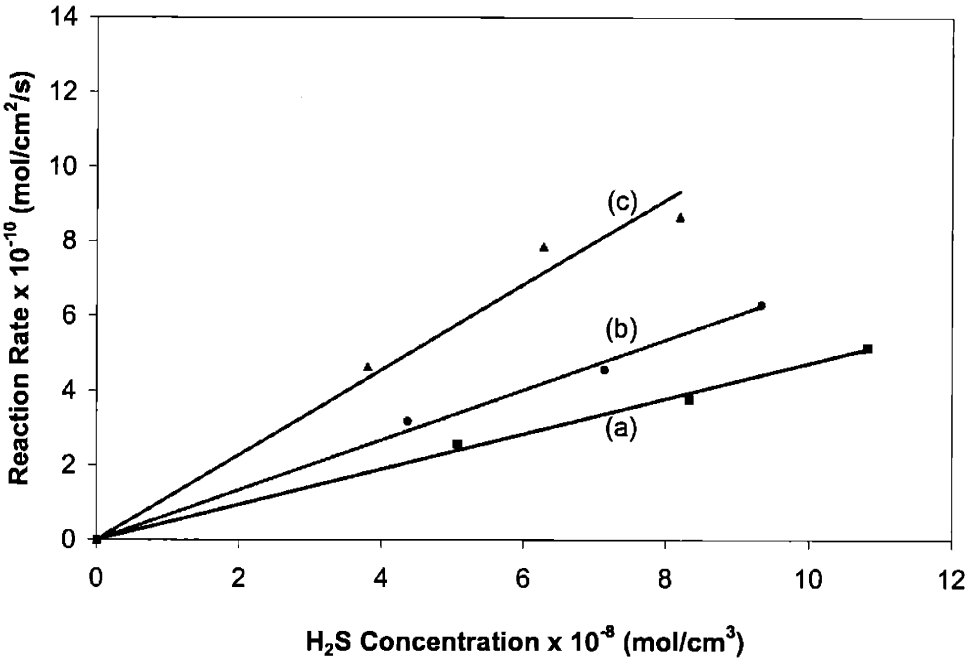

Figure 4.36 Effect of gas-phase H_2S concentration on the intrinsic reaction rate of 500°C-calcined nanocrystalline ZnO at (a) 300°C, (b) 400°C and (c) 500°C.

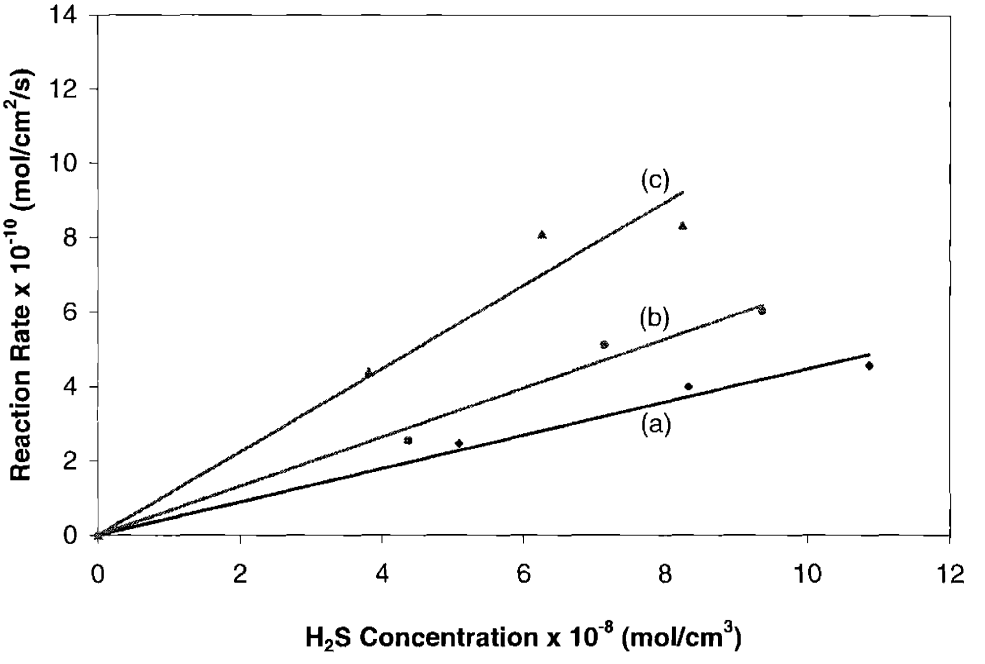

Figure 4.37 Effect of gas-phase H_2S concentration on the intrinsic reaction rate of conventional ZnO at (a) 300°C, (b) 400°C and (c) 500°C.

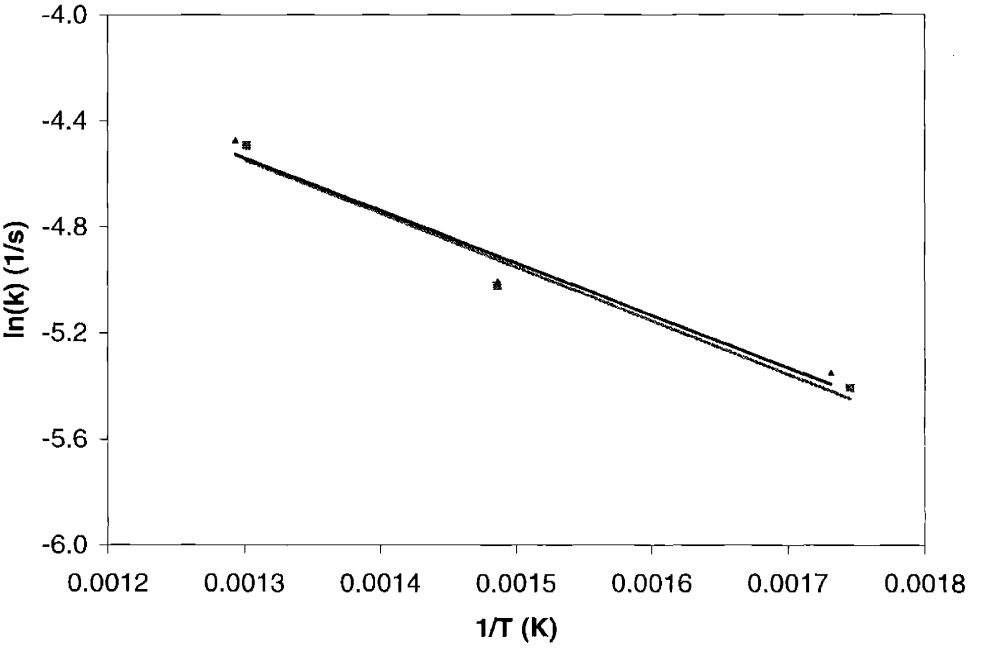

Figure 4.38 Arrhenius plot for (▲) conventional ZnO and (■) 500°C-calcined nanocrystalline ZnO.

TiO_2- and ZrO_2-coated ZnO also showed a linear relationship ($R^2 > 0.97$) between intrinsic reaction rate and H_2S concentration, confirming first-order kinetics as with pure ZnO (Figures 4.39 and 4.40). The reaction rate for TiO_2-coated ZnO was slightly lower than pure ZnO. However, this could have resulted from the assumption that the measured BET surface area of the TiO_2-coated ZnO was equivalent to the surface area of the ZnO core. The Arrhenius plot for TiO_2-coated ZnO was similar to that of pure ZnO, yielding an activation energy of 3.9 kcal/mol (Figure 4.41). Compared to pure and TiO_2-coated ZnO, ZrO_2-coated ZnO achieved an increase in absorption rate above 400°C, with a lower reaction rate at 300°C. This resulted in a significantly different Arrhenius plot, and thus, higher activation energy (7.1 kcal/mol). If we assume the actual surface area of the ZnO core was different from the measured BET surface area of the ZrO_2-coated ZnO and subtract the effects of the inert ZrO_2 coating, the resulting activation energy of ZrO_2-coated ZnO would still be 5.9 kcal/mol. The higher activation energy of the ZrO_2-coated nanocrystals relative to pure and TiO_2-coated ZnO nanocrystals suggested that H_2S absorption over ZrO_2-coated ZnO proceeded via a different mechanism.

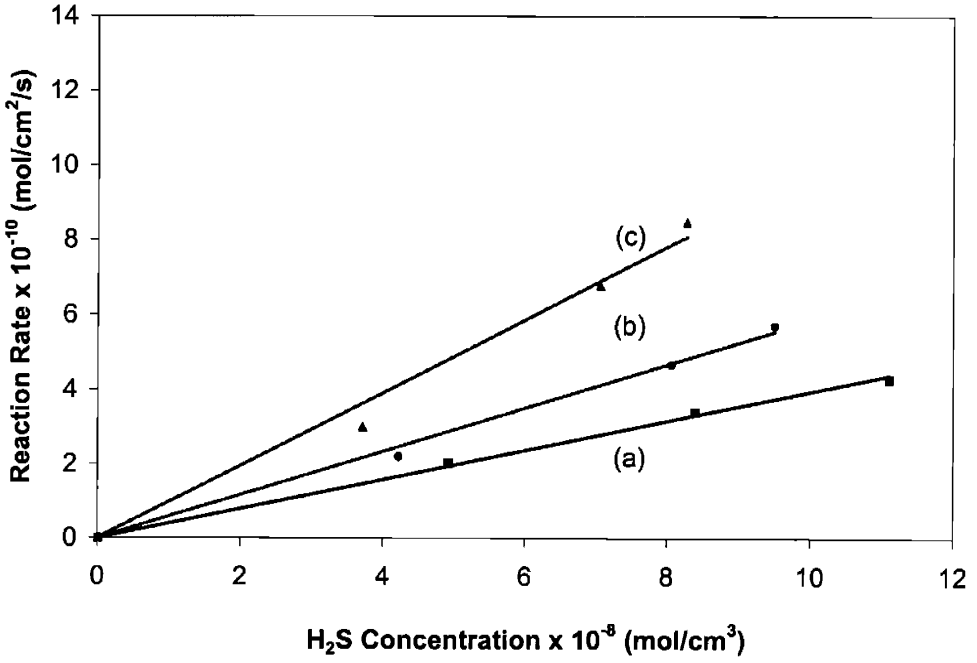

Figure 4.39 Effect of gas-phase H_2S concentration on the intrinsic reaction rate of 700°C-calcined TiO_2-coated ZnO at (a) 300°C, (b) 400°C and (c) 500°C.

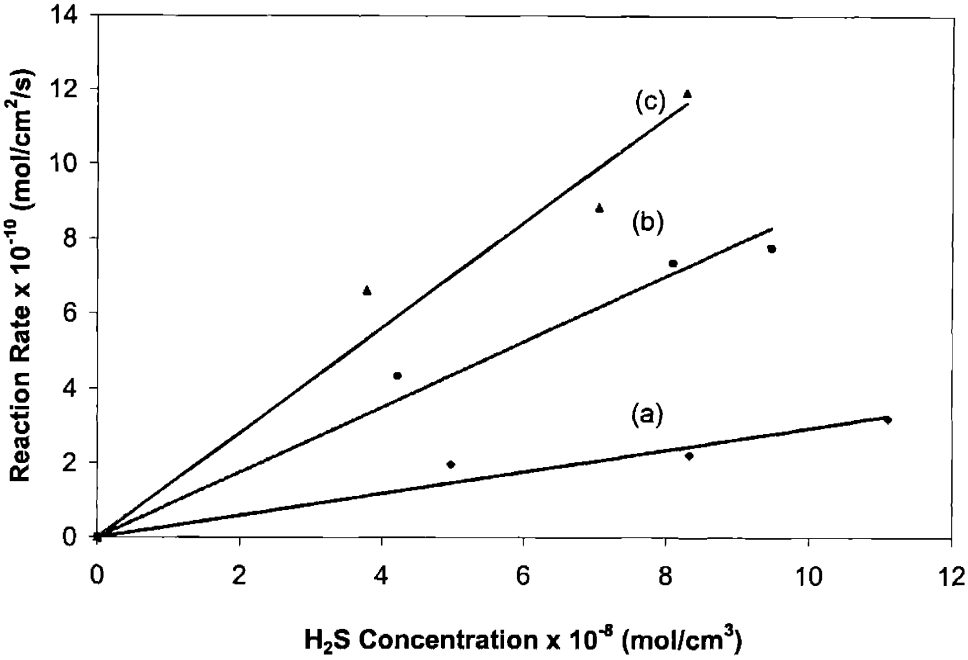

Figure 4.40 Effect of gas-phase H_2S concentration on the intrinsic reaction rate of 700°C-calcined ZrO_2-coated ZnO at (a) 300°C, (b) 400°C and (c) 500°C.

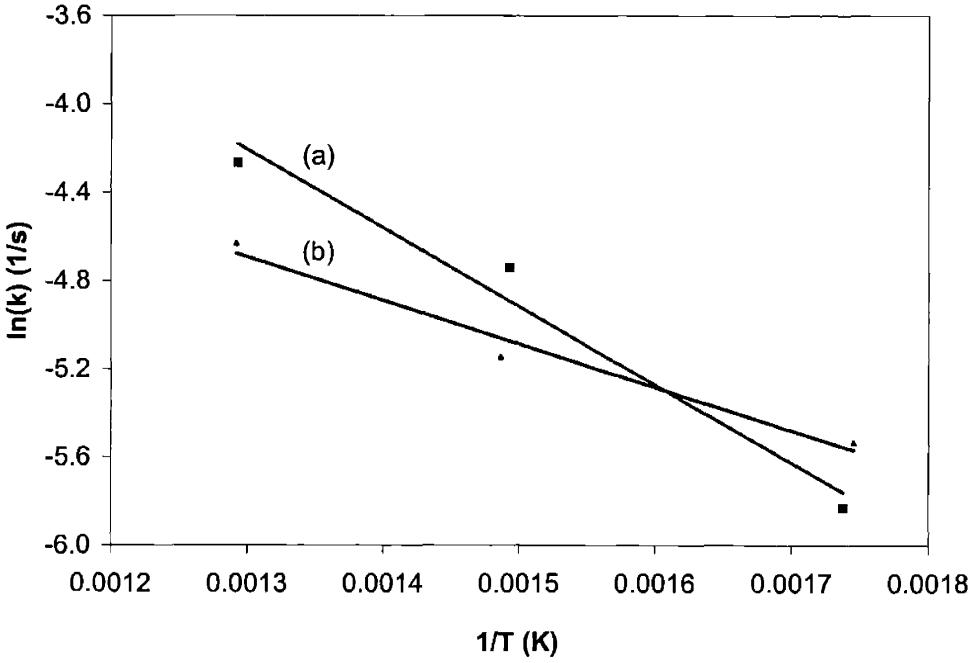

Figure 4.41 Arrhenius plot for 700°C-calcined (a) ZrO_2- and (b) TiO_2-coated ZnO.

Previous literature has suggested that increased surface area or surface activity plays a role in enhanced H_2S absorption over ZrO_2-ZnO mixtures [8]. Activation energy, however, is not affected by changes in surface area. Nevertheless, it was possible that the amorphous ZrO_2 deposits affected the H_2S adsorption on the ZnO nanocrystals surface. The increased temperature dependence evident from the high activation energy of ZrO_2-coated ZnO would then be related to the adsorption and diffusion through the amorphous ZrO_2.

4.4 Summary

Of the simple metal oxides for H_2S absorption, ZnO offers rapid oxygen-sulfur counter-diffusion, yielding the highest absorption efficiency. When operating in the diffusion-limited regime ($T \leq 500°C$), high ZnO conversions can be achieved by using ultrafine grain sizes and high surface areas. Through careful control of the zinc nitrate concentration, precipitation base and calcination process, nanocrystalline ZnO with a grain size < 10 nm and a surface area > 150 m^2/g was achieved. However, ZnO would begin to sinter above 350°C, and calcination to 500°C would yield a coarser grain size of 43 nm and a much smaller surface area of 15 m^2/g. Through the introduction of TiO_2, V_2O_5 and ZrO_2 coatings onto the 200°C-calcined ZnO, ZnO grain sizes of 9 nm, 11 nm and 13 nm were retained after calcination at 500°C, with surface areas of 88 m^2/g, 55 m^2/g and 56 m^2/g, respectively.

The effect of ZnO grain size on the H_2S absorption efficiency was studied at 300-500°C. Conversions of 6%, 20%, 30% and 67% were achieved at 300°C by conventional (130-nm), 43-nm, 28-nm and 13-nm ZnO, respectively. At 500°C, increased conversions were attained for both conventional (130-nm) and 43-nm ZnO (50% and 70%, respectively). The use of TiO_2 and ZrO_2 coatings gave rise to the finest ZnO grain sizes, such that ~ 100% conversions were obtained.

Upon regeneration in air at 650°C, ~ 70% conversion at breakthrough was achieved by 43-nm ZnO repeatibly at 500°C. In comparison, regenerated TiO_2- and ZrO_2-coated ZnO attained > 85% conversion at 500°C, with the latter showing negligible loss in capacity over three cycles.

Kinetics analysis with TGA was conducted to verify the effect of diffusion on H_2S absorption. 43-nm nanocrystalline ZnO showed a greater activity than conventional ZnO, with 50% instead of 16% conversion at 300°C. TiO_2-coated ZnO achieved superior absorption properties with full conversion in 30 min. At 500°C, TiO_2-coated ZnO became fully converted in < 10 min, while 43-nm nanocrystalline and conventional ZnO obtained 96% and 57%, respectively, after 60 min. The activation energy for conventional and nanocrystalline ZnO was determined to be 4.0 and 3.9 kcal/mol, respectively, indicating that difference in diffusion (rather than kinetics) was responsible for the improved absorption performance of the latter. TiO_2-coated ZnO had a similar activation energy as nanocrystalline ZnO, suggesting that the TiO_2 coating did not affect the absorption mechanism. The high activation energy of 7.1 kcal/mol for ZrO_2-coated ZnO indicated a more temperature-dependant rate-limiting step for this system. H_2S might have adsorbed onto the amorphous ZrO_2 coating, so that the adsorption and diffusion of H_2S onto the ZnO surface controlled the rate of absorption.

4.5 References

[1] Westmoreland, P. R., Gibson, J. B., Harrison, D. P., *Environ. Sci. Technol.* **1977**, *11*, 488.
[2] Westmoreland, P. R., Harrison, D. P., *Environ. Sci. Technol.* **1976**, *10*, 659.
[3] Twigg, V., *Catalyst Handbook*, 2nd ed., Wolfe Publishing Ltd., Frome, **1989**.
[4] Yumura, M., Furimsky, E., *Ind. Eng. Chem. Proc. Design Dev.* **1985**, *24*, 1165.
[5] Gibson, J. B., Harrison, D. P., *Ind. Eng. Chem. Proc. Design Dev.* **1980**, *19*, 231.
[6] Efthimiadis, E. A., Sotirchos, S. V., *Chem. Eng. Sci.* **1993**, *48*, 829.
[7] Ranade, P. V., Harrison, D. P., *Chem. Eng. Sci.* **1981**, *36*, 1079.
[8] Sasaoka, E., Sada, N., Manabe, A., Uddin, M. A., Sakata, Y., *Ind. Eng. Chem. Res.* **1999**, *38*, 958.
[9] Lew, S., Sarofim, A. F., Flytzani-Stephanopoulos, M., *Ind. Eng. Chem. Res.* **1992**, *31*, 1890.
[10] Lew, S., Jothimurugesan, K., Flytzani-Stephanopoulos, M., *Ind. Eng. Chem. Res.* **1989**, *28*, 535.
[11] Castellano, M., Matijevic, E., *Chem. Mater.* **1988**, *1*, 78.
[12] Chen, D. R., Jiao, X. L., Cheng, G., *Solid State Commun.* **1999**, *113*, 363.
[13] Chittofrati, A., Matijevic, E., *Coll. Surf.* **1990**, *48*, 65.
[14] Klissurski, D., Uzunov, I., Kumbilieva, K., *Thermochim. Acta* **1985**, *93*, 485.
[15] Koch, U., Fojtik, A., Weller, H., Henglein, A., *Chem. Phys. Lett.* **1985**, *122*, 507.
[16] Verges, M. A., Mifsud, A., Serna, C. J., *J. Chem. Soc. Faraday Trans.* **1990**, *86*, 959.
[17] Wang, L. N., Muhammed, M., *J. Mater. Chem.* **1999**, *9*, 2871.
[18] Lide, D. R., *CRC Handbook of Chemistry and Physics*, 72 ed., CRC Press, Boston, **1991**.
[19] Jing, L. Q., Xu, Z. L., Sun, X. J., Shang, J., Cai, W. M., *Appl. Surf. Sci.* **2001**, *180*, 308.
[20] Bahnemann, D. W., Kormann, C., Hoffmann, M. R., *J. Phys. Chem.* **1987**, *91*, 3789.
[21] Jolivet, J.-P., *Metal Oxide Chemistry and Synthesis: From Solution to Solid State*, John Wiley & Sons, Inc., New York, **2000**.
[22] Audebrand, N., Auffredic, J. P., Louer, D., *Chem. Mater.* **1998**, *10*, 2450.
[23] Ying, J., McMahon, G., *Mater. Res. Soc. Symp. Proc.* **1992**, 286, 73.
[24] Boccuzzi, F., Chiorino, A., *J. Phys. Chem.* **1996**, *100*, 3617.
[25] Clark, F. T., Springman, M. C., Willcox, D., Wachs, I. E., *J. Catal.* **1993**, *139*, 1.
[26] Gao, X. T., Fierro, J. L. G., Wachs, I. E., *Langmuir* **1999**, *15*, 3169.
[27] Gao, X. T., Bare, S. R., Weckhuysen, B. M., Wachs, I. E., *J. Phys. Chem. B* **1998**, *102*, 10842.
[28] Gao, X. T., Bare, S. R., Fierro, J. L. G., Banares, M. A., Wachs, I. E., *J. Phys. Chem. B* **1998**, *102*, 5653.
[29] Ocana, M., Hsu, W. P., Matijevic, E., *Langmuir* **1991**, *7*, 2911.
[30] Tamhankar, S. S., Bagajewicz, M., Gavalas, G. R., Sharma, P. K., Flytzani-Stephanopoulos, M., *Ind. Eng. Chem. Proc. Design Dev.* **1986**, *25*, 429.

5 – Recommendations for Future Work

Our CeO_2-based nanocomposites showed improved stability and low-temperature reducibility especially with Pr dopants. It would be of interest to develop PrO_2-based nanocomposites for oxygen storage applications. Various dopants could be introduced to PrO_2 so as to improve its microstructure and thermal stability, and to achieve a system with optimal low-temperature reducibility. Pulsing studies could be performed on the selected $Ce_{1-x}M_xO_{2-\delta}$ and $Pr_{1-x}M_xO_{2-\delta}$ nanocomposites to determine their oxygen storage capacities under dynamic oxidizing and reducing conditions.

$CuO/CuCr_{1.9}Co_{0.1}O_4$ and $CuO/CuCr_2O_4$ materials achieved superior SO_2 adsorption characteristics compared to the conventional CuO/Al_2O_3 adsorbent. Although an ultrafine grain size was attained for these novel compositions, further optimization in synthesis would be useful to improve their microstructure. A higher surface area material should possess better characteristics for this highly surface-dependent process. Specifically, it would be of interest to (1) optimize the synthesis route with the aim of limiting particle agglomeration, and (2) evaluate various support materials (e.g. Al_2O_3, SiO_2 and ZrO_2) for $CuO/CuCr_{1.9}Co_{0.1}O_4$, so as to maximize the active surface area while maintaining the favorable SO_2 desorption characteristics.

Recent research on SO_2 reduction to elemental S by CO and CH_4 involved CuO/CeO_2 nanocomposite catalysts. Our work on CeO_2-based nanocomposites indicated enhanced low-temperature redox activity, which would be useful for the SO_2 reduction reaction. On the other hand, our $CuCr_2O_4$ nanocomposites have shown low-temperature SO_2 sorption and CO oxidation activities, with the ability to reduce SO_2 to elemental S. By combining these two systems to produce CeO_2-$CuCr_2O_4$ nanocomposites, superb catalyst for SO_2 reduction activity might be attained.

The introduction of V_2O_5, ZrO_2 and TiO_2 coatings onto ZnO has imparted excellent thermal stability to ZnO nanocrystals. This stabilization technique may be extended to other simple and mixed metal oxide systems where thermal stability is an issue. Also, by modifying the surface chemistry of the ZnO nanocrystals, improved activity might be achieved for sensor and photocatalytic applications. A study of secondary oxide coating composition and loading on ZnO and other semiconducting oxides would provide interesting insights into the structure-property relationships of metal oxide interfaces and heterojunctions.

6 – Conclusions

The remediation of automotive emissions has become increasingly important as regulations push toward zero-emission vehicles. Through nanocrystalline synthesis and nanocomposite design, novel metal oxide systems have been developed for the removal of environmental and catalytic poisons. These materials address major challenges in the lean-burn engine and fuel cell technologies: (1) oxygen storage for the elimination of CO and hydrocarbons, (2) SO_2 adsorption to prevent poisoning of NO_x treatment materials, and (3) H_2S absorption to prevent poisoning of H_2 separation membranes and fuel cell systems.

In conventional three-way catalytic converters, CeO_2 is employed to provide oxygen during fuel-rich conditions to promote CO and hydrocarbon conversion to CO_2 and H_2O. With the introduction of dopants, the active temperature range for CeO_2-based nanocomposites was significantly broadened. It was found that for the $Ce_{0.8}M_{0.2}O_{2-\delta}$ series, Pr doping led to the highest surface area at 600°C; Zr doping resulted in improved microstructural stability to 1000°C. In temperature-programmed reduction and CO oxidation studies, $Ce_{0.8}Pr_{0.2}O_{2-\delta}$ attained a significant reducibility below 450°C, achieving the greatest weight loss of 1.8% by 800°C, and showed a low CO light-off temperature of 274°C. For the $Ce_xM_{1-x}O_{2-\delta}$ series, Pr and Zr doping provided for substantial improvements in low-temperature and overall reducibility for $x \leq 1.0$ and $x \leq 0.3$, respectively. $Ce_xPr_{1-x}O_{2-\delta}$ showed improved reducibility with increasing Pr content, reaching a maximum of 4.8% weight loss for $x = 1.0$. A significant portion of this weight loss (1.5%) was achieved at $\leq$ 350°C, due to a transition from PrO_2 to Pr_6O_{11}. In catalytic CO oxidation, reduced light-off temperatures were obtained for $Ce_xPr_{1-x}O_{2-\delta}$ and $Ce_xZr_{1-x}O_{2-\delta}$, with the lowest light-off temperatures of 264°C and 252°C achieved at $x = 0.4$ and 0.1, respectively.

SO_2 is adsorbed competitively and irreversibly on NO_x traps in lean-burn engine applications. Conventional SO_2 adsorbents do not possess the adsorption and regeneration characteristics needed for automotive applications. We have developed novel Cr_2O_3-CuO nanocomposites with excellent SO_2 adsorption capacity and low-temperature regenerability (< 350°C). By increasing the CuO content in these mixed oxides, both adsorption and desorption properties could be improved. These materials were further optimized through doping of the $CuCr_2O_4$ phase with Co at the Cr site. Improved SO_2 adsorption capacity was seen with increasing Co content, and significant SO_2 desorption was attained below 300°C. The addition of CuO to $CuCr_{1.9}Co_{0.1}O_4$ by various techniques resulted in excellent thermal stability and

adsorption/desorption characteristics. Dynamic pulse studies illustrated that $CuO/CuCr_{1.9}Co_{0.1}O_4$ and $CuO/CuCr_2O_4$ materials provided for faster and more efficient SO_2 regeneration than the conventional CuO/Al_2O_3 adsorbent. Moreover, 100% SO_2 removal was achieved with these novel mixed oxides during the SO_2 adsorption cycles, whereas CuO/Al_2O_3 showed significant decay in SO_2 adsorption activity over multiple cycles.

In the production of H_2 for fuel cells, the removal of H_2S is critical to prevent poisoning of both the H_2 separation membrane and the fuel cell materials. Traditionally, coarse-grained ZnO is used to removal gas-phase H_2S at moderate temperatures (300-500°C). However, oxygen-sulfur counter-diffusion limits the absorption efficiency of conventional ZnO. We have successfully synthesized ZnO with an ultrafine grain size of < 10 nm and a high surface area of > 150 m^2/g via nanocrystalline processing. The ZnO nanocrystals (43 nm) exhibited excellent absorption capacity with ZnO-to-ZnS conversion of ~ 70% at 500°C, which was superior to the 50% conversion achieved by the coarse-grained ZnO (130 nm). They were further stabilized from grain growth through the addition of secondary metal oxide coatings. The finer grain size of 9 nm for TiO_2-coated ZnO led to significant improvements in the H_2S absorption capacity, yielding > 90% conversion at breakthrough at 300-500°C. TiO_2- and ZrO_2-coated ZnO also showed excellent regenerability at 500°C, achieving > 85% conversion at breakthrough over multiple cycles. The absorption kinetics for conventional, nanocrystalline and TiO_2-coated ZnO revealed that these materials all reacted via a similar mechanism with an activation energy of ~ 3.9 kcal/mol. In contrast, ZrO_2-coated ZnO had a higher activation energy of 7.1 kcal/mol, possible due to H_2S adsorption on amorphous ZrO_2.